M 2023

U.PORTO
FEUP FACULDADE DE ENGENHARIA
UNIVERSIDADE DO PORTO

NETMIX CRYSTALLISER FOR NUTRIENTS RECOVERY FROM SIDE-STREAM DIGESTATE

LAURA JOANA RIBEIRO CULLEN
MASTER THESIS IN CHEMICAL ENGINEERING
PRESENTED TO THE FACULTY OF ENGINEERING
OF THE UNIVERSITY OF PORTO

Master in Chemical Engineering

NETmix crystalliser for nutrients recovery from side-stream digestate

Master dissertation

of

Laura Joana Ribeiro Cullen

Developed within the course of dissertation

held in

LSRE-LCM - Laboratory of Separation and Reaction Engineering – Laboratory of Catalysis and Materials

Supervisor at FEUP: **Vítor Jorge Pais Vilar, Principal Researcher at LSRE-LCM**

Joint supervisor at FEUP: **Ricardo Nogueira dos Santos, Auxiliary Researcher at LSRE-LCM**

U.PORTO
FEUP FACULDADE DE ENGENHARIA UNIVERSIDADE DO PORTO

DEPARTAMENTO DE ENGENHARIA QUÍMICA

July 2023

Agradecimentos

Primeiramente, gostaria de mostrar o meu agradecimento à minha equipa de orientação. Ao Professor Vítor Vilar, muito obrigada por ter proporcionado os recursos necessários à realização deste trabalho e pelas sugestões e conselhos dados ao longo do semestre. Ao Professor Ricardo Santos, muito obrigada pela sua constante dedicação e apoio, pela boa disposição, e por estar sempre disponível para esclarecimento de qualquer dúvida.

De seguida, um especial agradecimento à Isabel Fernandes que, apesar de não compor oficialmente a equipa de orientação, se mostrou sempre disponível para ajudar e cujos conselhos foram imprescindíveis para a concessão deste trabalho.

À Sofia Brandão, muito obrigada por me ter guiado no início deste percurso, pelo apoio dado no começo das atividades experimentais e pela preciosa ajuda na interpretação de resultados. À Yaidelin Manrique e à Margarida Brito, uma palavra de apreço pelo apoio dado durante a realização das atividades experimentais. Ao Paulo Marrocos, que se mostrou sempre disponível para ajudar com qualquer dúvida e pela partilha de conhecimento. À Carla Santos e à Kamila Amancio, pela ajuda prestada na caracterização das amostras das escorrências.

Gostaria ainda de agradecer à Margarida e à Teresa pelo espírito de amizade e de entreajuda, pelas boas conversas e momentos que partilhamos juntas durante este período. Aos restantes colegas de gabinete, Eduardo, Carolina, Sofia e Isabel, muito obrigada pela vossa boa disposição e por me terem acolhido de braços abertos.

Às amizades que a FEUP me proporcionou durante estes cinco anos, muito obrigada por todas as gargalhadas, abraços e convívios que tive o prazer de partilhar convosco. Tornaram o meu percurso nesta casa muito mais fácil e divertido. À minha afilhada, Sobral, muito obrigada por todas as boas conversas que temos, por todas as aventuras e por me dar sempre o seu apoio.

Às minhas amigas de longa data, Ana e Maria, foi um prazer caminhar e crescer ao vosso lado ao longo destes 17 anos. Não há palavras que descrevam o quanto a vossa amizade significa para mim. À Dias, por todas as aventuras, por todas as viagens, pelos conselhos, desabafos e por me conseguir por sempre um sorriso na cara. À Isabel e à Brandão, obrigada pela vossa preciosa amizade.

Por fim, gostaria de dar um especial agradecimento à minha família. Aos meus pais, que sempre me deram o seu apoio e amor incondicional e que são a razão de poder estar hoje a escrever estas palavras. Ao meu avô, por ser uma das pessoas que mais admiro, e por todos os ensinamentos que me proporcionou ao longo da minha vida.

Dr. Vítor Vilar and Dr. Ricardo Santos, supervisors of this dissertation, are members of LSRE-LCM - Laboratory of Separation and Reaction Engineering – Laboratory of Catalysis and Materials, financially supported by LA/P/0045/2020 (ALiCE), UIDB/50020/2020 and UIDP/50020/2020 (LSRE-LCM), funded by national funds through FCT/MCTES (PIDDAC).

REPÚBLICA PORTUGUESA FCT Fundação para a Ciência e a Tecnologia

Abstract

Phosphorus is a key element for plant growth, thus being one of the main constituents of fertilisers. However, the intensification of agricultural practices over the years led to an excessive release of this nutrient into water streams, causing severe harm to aquatic ecosystems. In addition, phosphorus is obtained from phosphate rocks, which are a non-renewable resource and their growing depletion has become an alarming concern. Therefore, it is imperative to find ways to recover this nutrient and make its life cycle more sustainable. Wastewater is known to be a great source of nutrients, especially nitrogen (N) and phosphorus (P). In recent years, the idea of recovering these nutrients from these effluents in solid form to produce a value-added product has emerged.

In this sense, the main objective of this dissertation was to explore the use of the NETmix technology for the recovery of P and N in the form of struvite crystals from the liquid fraction of a side-stream obtained after anaerobic digestion. This mineral has great fertilising properties due to its poor solubility in water and a slow-release rate of nutrients. To do so, Computational Fluid Dynamics (CFD) tools were employed to study the flow distribution, mass transfer and flow dynamics in the 2D ExtendedNUB (NETmix Unit Block) model, which only represents a subsection of the NETmix network, when dissimilar flow conditions are set at the inlets. Inlet conditions corresponded to a fully laminar steady regime in the right-hand side and a self-sustained fully chaotic regime in the left-hand side. Tracer experiments were simulated.

In all cases studied, a uniform flow distribution along the ExtendedNUB network was obtained, which attested to the great mixing capacities of this reactor. Moreover, it was verified that a higher Reynolds number at the left inlet enhanced the mass transfer phenomenon between the water and tracer phases due to a greater mixing degree promoted by vortex engulfment in downstream chambers. Finally, a flow dynamics analysis allowed to conclude that a fully developed dynamic flow was achieved in the downstream chamber of the ExtendedNUB in the cases with a higher Re value in the left inlet. For the other cases, a poor dynamic transfer between the two halves of that same chamber was observed, which resulted in a lower mixing degree and the occurrence of concentration gradients at the outlets.

Experimental validation of the CFD results in a NETmix reactor with the same dimensions as the ExtendedNUB showed that, in fact, this static mixer is able to efficiently mix two streams along its network when operated with dissimilar flow conditions. Nevertheless, it was verified that the mixing degree along the rows of its network was not uniform, meaning that further experimental validation should be done to assess whether it is possible to obtain outflows with similar compositions.

The CFD results obtained in this dissertation demonstrated that efficient mixing is achieved when the NETmix reactor is operated with dissimilar inlet flow conditions, which supports its use for the production of struvite crystals from anaerobic digestion liquid effluents.

Keywords: NETmix, CFD, crystallisation, nutrients recovery, struvite, hydrodynamic studies.

Resumo

O fósforo é essencial para o crescimento de plantas e é um dos principais constituintes dos fertilizantes. No entanto, a intensificação de práticas agrícolas tem resultado numa libertação excessiva deste nutriente em cursos de água, causando graves danos em ecossistemas aquáticos. Além disso, o fósforo é obtido a partir de rochas fosfatadas, um recurso não renovável e cujo esgotamento progressivo tem-se tornado alarmante, pelo que é imperativo arranjar formas de recuperar este nutriente e tornar o seu ciclo de vida mais sustentável. As águas residuais são uma grande fonte de nutrientes, especialmente de nitrogénio (N) e de fósforo (P). Recentemente, tem surgido a ideia de fazer a recuperação de nutrientes presentes nestes efluentes na forma sólida, por forma a se produzir um produto com valor acrescentado.

Neste sentido, o principal objetivo do presente trabalho foi validar a utilização da tecnologia NETmix para a recuperação de P e N sob a forma de cristais de estruvite a partir da fração líquida de uma corrente secundária obtida após o processo de digestão anaeróbica. Este mineral possui uma grande capacidade fertilizante devido a uma fraca solubilidade em água e a uma taxa de libertação de nutrientes baixa. Para tal, foram utilizadas ferramentas de Dinâmica de Fluidos Computacional (CFD) para estudar a distribuição de escoamento, a transferência de massa e a dinâmica de escoamento no modelo 2D *ExtendedNUB* (*NETmix Unit Block*), que apenas representa uma subsecção da rede NETmix, quando são impostas condições de escoamento diferentes nas entradas. Foi definido um regime totalmente laminar na entrada do lado direito e um regime totalmente caótico na entrada do lado esquerdo. Além disso, foram simuladas experiências com traçador.

Em todos os casos estudados foi obtida uma distribuição uniforme do escoamento ao longo da rede do modelo *ExtendedNUB*, o que comprovou a grande capacidade de mistura deste reator. Adicionalmente, verificou-se que um número de Reynolds, Re, mais elevado na entrada esquerda resultou numa maior transferência de massa entre a água e o traçador devido a um melhor grau de mistura, o qual era promovido pelo engolfamento de vórtices em câmaras a jusante. Por último, a análise da dinâmica de escoamento permitiu concluir que um escoamento dinâmico perfeitamente desenvolvido foi obtido na câmara mais a jusante do modelo *ExtendedNUB* nos casos com um Re mais elevado na entrada do lado esquerdo. Nos restantes casos, não foi obtido um escoamento com tais características, o que resultou num menor grau de mistura e na obtenção de gradientes de concentração nas correntes à saída.

Foram realizadas experiências de traçador num reator NETmix com as mesmas dimensões que o modelo *ExtendedNUB* por forma a se validar os resultados das simulações. Verificou-se que este misturador estático consegue, de facto, misturar eficazmente duas correntes ao longo da sua rede quando lhe são impostas condições de escoamento diferentes nas entradas. Todavia, o grau de mistura ao longo das linhas da rede do NETmix não foi uniforme. Tal indica que deverão ser realizadas mais experiências para se avaliar se é possível obter correntes de saída com composições semelhantes.

A realização do presente trabalho permitiu concluir que é possível obter um grau de mistura eficiente no reator NETmix quando este é operado com condições de escoamento diferentes nas suas entradas, validando o seu uso para a produção de cristais de estruvite a partir de efluentes da digestão anaeróbia.

Palavras-chave: NETmix, CFD, cristalização, recuperação de nutrientes, estruvite, estudos hidrodinâmicos.

Declaration

I hereby declare, under word of honour, that this work is original and that all non-original contributions is indicated and due reference is given to the author and source.

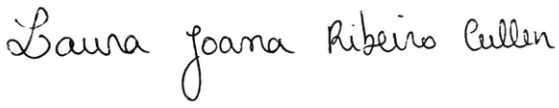

Laura Joana Ribeiro Cullen

July 2023

Index

List of Figures

List of Tables

Notation and Glossary

A	Cross-sectional area	m^2
A_{2D}	Area of the 2D ExtendedNUB geometry	m^2
Co	Courant number	
C_t	Constant for the determination of the turbulent viscosity	
$C_{1\varepsilon}$	Standard *k-ε* turbulence model constant	
$C_{2\varepsilon}$	Standard *k-ε* turbulence model constant	
$C_{3\varepsilon}$	Standard *k-ε* turbulence model constant	
d	NETmix channel width or characteristic diameters of the Y-flow distributor	m
D	NETmix chamber diameter	m
$D_{i,m}$	Mass diffusion coefficient	$m^2 \cdot s^{-1}$
$D_{T,i}$	Soret diffusion coefficient	$m^2 \cdot s^{-1}$
E	Enstrophy	$m^2 \cdot s^{-2}$
$E_{r,\Delta p_{distributor}}$	Relative error for the pressure differences between the Y-flow distributor outlets	%
$E_{r,\tau}$	Relative error for the shear stresses	%
f	Frequency	s^{-1}
$\vec{F}$	Term of the momentum Navier-Stokes equation that accounts for external body forces	$kg \cdot m^{-2} \cdot s^{-2}$
$\vec{g}$	Acceleration of gravity vector	$m \cdot s^{-2}$
G_b	Term related to the generation of turbulent kinetic energy due to buoyancy	$kg \cdot m^{-1} \cdot s^{-3}$
G_k	Term related to the generation of turbulent kinetic energy due to velocity gradients	$kg \cdot m^{-1} \cdot s^{-3}$
h_1	Length of the Y-flow distributor inlet channel	m
h_2	Length of outlet channels of the Y-flow distributor	m
I	Unit tensor	
I_s	Intensity of segregation	
I_t	Intensity of turbulence	
$\vec{J}_i$	Diffusion flux of a species *i*	$kg \cdot m^{-2} \cdot s^{-1}$
k	Turbulent kinetic energy	$m^2 \cdot s^{-2}$
K_{sp}	Solubility product constant	
l	NETmix channel length	m
L	Characteristic length scale	m
$\dot{m}$	Mass flowrate	$kg \cdot s^{-1}$
N	Number of time steps	
p	Total pressure	Pa
P	Wet perimeter	m
pH	Hydrogen potential	
p_s	Static pressure	Pa
q	Volumetric flowrate	$m^3 \cdot s^{-1}$
r	Distance to the axis of a NETmix channel	m
Re	Reynolds number	
R_i	Rate of formation of a species *i* by chemical reaction	$kg \cdot m^{-3} \cdot s^{-1}$
S_i	Source term of the convection-diffusion equation	$kg \cdot m^{-3} \cdot s^{-1}$
S_k	Source term of the transport equation for turbulent kinetic energy	$kg \cdot m^{-1} \cdot s^{-3}$
S_m	Source term of the general continuity equation	$kg \cdot m^{-3} \cdot s^{-1}$
S_ε	Source term of the transport equation for turbulent dissipation rate	$kg \cdot m^{-1} \cdot s^{-4}$
t	Time	s
T	Temperature	K
u	Velocity magnitude	$m \cdot s^{-1}$
w	NETmix width	m
x	Mass fraction of a certain species or axial coordinate	
$x(t)$	Function of time	
$X(f)$	Function of frequency	
y	Axial coordinate	
Y_i	Local mass fraction of a certain species *i*	
Y_M	Term related to fluctuating dilation	$kg \cdot m^{-3} \cdot s^{-1}$

Greek Letters

α	Forward enstrophy flux	$m^3 \cdot s^{-4}$
δ_{ij}	Kronecker delta	
$\Delta p_{distributor}$	Pressure drop inside the Y-flow distributor	Pa
Δp_{outlet}	Pressure difference between both Y-flow distributor outlets	Pa
Δt	Time step	s
Δx	Mesh element size	m
ε	Turbulent dissipation rate or kinetic energy cascade rate	$m^2 \cdot s^{-3}/s^3 \cdot m^{-1/2}$
θ	Angle between the two Y-flow distributor outlet channels	rad
λ	Wavenumber	m^{-1}
μ	Dynamic viscosity	Pa.s
μ_t	Turbulent viscosity	Pa.s
π	Pi number	
ρ	Density of a fluid	$kg \cdot m^{-3}$
σ_a	Standard deviation of the mass fraction of a species A	
σ_b	Standard deviation of the mass fraction of a species B	
σ_ε	Prandtl number for the turbulent dissipation rate	
σ_k	Prandtl number for the turbulent kinetic energy	
τ	Passage time or shear stresses	s/Pa
$\bar{\bar{\tau}}$	Stress tensor	$N \cdot m^{-2}$
Υ	Amplitude of the Fast Fourier Transform of the velocity fluctuation	$m \cdot s^{-1}$
φ	Generic solution variable	

Indexes

*	Dimensionless variable
$\bar{}$	Average variable
$\vec{}$	Vector variable
’	Fluctuating component
2D	Refers to the 2D ExtendedNUB geometry
3D	Refers to real NETmix reactor
a	Indicates a certain species A
b	Indicates a certain species B
bifurcation	Relative to the bifurcation of the Y-flow distributor
c	Critical
h	Hydraulic
channel	Channel of the NEB geometry
i	Indicates the x-coordinate, a ExtendedNUB channel number or a generic species *i*
in	One of the inlets of the ExtendedNUB
inlet	Inlet of the Y-flow distributor
j	Indicates the y-coordinate
l	Indicates the ExtendedNUB left side or the z-coordinate
lateral chamber	Lateral chambers of the NEB geometry
m	Left side of the ExtendedNUB
max	Maximum
outlet	Both outlets of the Extended NUB or both outlets of the Y-flow distributor
outlet1/out,1	Left outlet of the Y-flow distributor
outlet2/out,2	Right outlet of the Y-flow distributor
r	Right side of the ExtendedNUB
radial inlet	Radial inlet of the NEB geometry
RI	Inlet chamber of the NEB geometry
s	Static or segregation
t	Tracer or turbulent
T	Transposed matrix
tracer	Refers to the tracer phase
water	Refers to the water phase
x	Coordinate axis

List of Acronyms

ATP	Adenosine Triphosphate
CFD	Computational Fluid Dynamics
CFL	Courant-Friedrichs-Lewy
COD	Chemical Oxygen Demand
DFT	Discrete Fourier Transform
DIC	Dissolved Inorganic Carbon
DOC	Dissolved Organic Carbon
EU	European Union
ICP	Inductively coupled plasma
LCM	Laboratory of Catalysis and Materials
LSRE	Laboratory of Separation and Reaction Engineering
MUSCL	Monotone Upstream-Centered Schemes for Conservation Laws
NDIR	Non-Dispersive Infrared
NEB	NETmix Entire Block
NUB	NETmix Unit Block
OES	Optical Emission Spectrometry
PRESTO!	Pressure Staggering Option
RANS	Reynolds-averaged Navier Stokes
SIMPLEC	Semi-Implicit Method for Pressure linked Equations-consistent
TDC	Total Dissolved Carbon
TN	Total Nitrogen
TP	Total Phosphorus
TS	Total Solids
TSS	Total Suspended Solids
UV/VIS	Ultraviolet-visible
UWWTD	Urban Waste Water Treatment Directive
VSS	Volatile Suspended Solids
WWTP	Wastewater Treatment Plant

1 Introduction

1.1 Framing and presentation of the work

Phosphorus (P) is a key element for plant growth, a constituent of plant cells and a main component of tissue molecules, such as nucleic acids and adenosine triphosphate (ATP). This means that, for plants to develop properly, they need to have access to this nutrient in their early stages of development. P is abundantly present in soils in the form of insoluble inorganic phosphate compounds and organic compounds, with concentrations varying from 0.022 to 0.090 kg P·m^{2}. However, plants only have access to a small percentage of this nutrient (approximately 20 %) in the form of inorganic phosphorus dissolved in water or dissolved directly in the soil, so the use of natural (manure) or synthetic fertilisers as a source of nutrients becomes necessary to ensure proper crop growth [1, 2].

Synthetic fertilisers are usually made from phosphate rocks, which are extracted from geological phosphorus reserves and are a limited resource. In recent years, there has been a growing concern regarding the non-renewability of these resources and their evident depletion worldwide, as a result of intensification of agricultural practices and a poor management of organic P resources. Predictions on how much longer these resources will last are not concordant, with lifespans varying from 50 to 400 years. Moreover, studies show that the depletion rate of phosphate rocks can vary between 4 to 19 kg·ha^{-1}·yr^{-1} [2]. In addition to this problem, there is the issue of P removal from soils primarily due to erosion by water. Although it is a natural phenomenon, the excessive use of this resource increases the amount of phosphorus that is lost. This element is released into water streams, which causes the eutrophication of lakes, rivers or backwaters and consequent damage to aquatic ecosystems, and also the discharge of this element into the ocean [2]. In 2013, the quantity of P discharged into the ocean was estimated to be 37.9 Tg, which corresponds to more than 50 % of the P consumed that year [3]. Thus, the life cycle of phosphorus is a one-way flow, meaning that, aligned with its increasing scarcity, it is mandatory to find ways to recycle and recover this element so that its use becomes more sustainable.

Wastewater is known to be a great source of nutrients, such as nitrogen, potassium, phosphorus, among others. Regarding P, industrial wastewater influents may contain, on a daily average, a Total Phosphorus (TP) concentration of 3.5 mg·L^{-1} [4] and municipal wastewaters may contain between 6 and 12 mg·L^{-1} [3]. The main sources of phosphate pollution in water streams are fertilisers, detergents and human waste. These waters, before being discharged into the environment, are subject to several treatment processes in Wastewater Treatment Plants (WWTPs), including sedimentation, filtration and biological treatment, so as to enhance their quality and reduce their toxicity in accordance with the European Union (EU) Urban Wastewater Treatment Directives [5]. In recent years, efforts have been made to develop and implement efficient phosphorus recovery technologies in WWTPs. This nutrient is usually removed from a side-stream generated during anaerobic digestion, which is called digestate and is composed of two phases, namely the solid and liquid phases. This study will focus on the recovery of P from the liquid fraction of this stream, the centrate, obtained through a dewatering process of the digestate [3]. The most conventional method to recover P from these streams is through crystallisation processes, in which it precipitates in the form of magnesium ammonium phosphate, also known as struvite, through the

addition of magnesium (Mg) salts. This mineral is considered a promising alternative to phosphate rock-based fertilisers, due to being a slow-release fertiliser and a great source of phosphorus as well as nitrogen (N), and the fact that it is obtained in an environmentally friendly way [6].

Apart from crystallisation techniques, other P recovery technologies have been studied, such as adsorption and electrochemical precipitation. However, these are still premature from a scientific point of view [3] and crystallisation presents significant advantages, such as a very high recovery rate and no need of supplementary materials like adsorbents, catalysts or membranes [7]. Nonetheless, when crystallisation is used to treat the above-mentioned side-stream, there are still a few drawbacks, which are the fact that it is necessary to use an external source of Mg to promote the formation of struvite, thus resulting in additional costs to the process [6], and also because crystallisation-based technologies that already exist to recover P are still not economically feasible in the long term [8].

In this sense, the main objective of this work is to propose the use of the NETmix technology as an answer to the issues stated above. The NETmix is a patented static mixer developed at the Associate Laboratory LSRE-LCM in 2005. It is known for its great mixing capacities above a critical Reynolds number due to its characteristic geometry, which is crucial to attain high conversion rates in chemical reactions. Additionally, it allows an efficient control of the inlet flow conditions, and it is easy to scale up or number up in accordance with its intended use. This technology has already an industrial application, which is the production of a nanocrystal called hydroxyapatite performed by the company Fluidinova [9].

In this work, Computational Fluid Dynamics (CFD) tools will be used to assess the performance of the NETmix in the production of struvite crystals from side-stream digestate. Several asymmetric inlet flow conditions will be studied in order to predict the performance of this reactor when mixing a dilute stream with the nutrients to be precipitated (the digestate liquid fraction) and a stream with a high concentration of Mg. The following aspects will be analysed: flow distribution, mass transfer and flow dynamics. Finally, experimental validation of the CFD results will be performed.

1.2 Contribution of the author to the work

All CFD simulations done with the 2D ExtendedNUB geometry were performed by the author. The mesh used in these simulations was generated for previous works by Fernandes et al. [10]. The experimental setup used for the tracer experiments was also developed for previous works done by Fernandes et al. [10]. The experiments were conducted with the aid of Doctoral Researchers Margarida Brito and Yaidelin Manrique and Project Researcher Sofia Brandão. Furthermore, the analysed digestate liquid fraction was provided by Ave WWTP, situated in Tougues, Portugal. The characterisation analysis of this effluent was done with the aid of Mobility PhD student Kamila Amancio and PhD Student Carla Santos. The Inductively Coupled Plasma (ICP) analysis of the effluent was done by Engineer Liliana Pereira. At last, the design, mesh validation and CFD simulations done with the Y-flow distributor geometry were done by the author. The design of the NETmix Entire Block geometry was done with the aid of PhD student Paulo Marrocos. The mesh validation and CFD simulations were performed by the author.

1.3 Organisation of the dissertation

This dissertation is divided into the following chapters:

Chapter 1 introduces the present dissertation by explaining the importance of recovering and recycling phosphorus from wastewaters and highlights its main objectives.

Chapter 2 gives context to this work and is divided into four sections: section 2.1 emphasises the importance of WWTPs and briefly describes how the liquid fraction of digestates is obtained; section 2.2 compares the composition of several digestates with different origins and discusses the potential environmental implications associated with the direct application of digestate liquid fractions on soils; section 2.3 describes the working principles of different methods to recover nutrients from these streams in solid form and their advantages and disadvantages. It also concludes that crystallisation is the most suitable method to recover P and N. This section has a subsection, numbered 2.3.1, in which the precipitation of struvite crystals through a crystallisation process is described and several factors affecting the extension of the reaction are discussed. Finally, section 2.4 introduces the NETmix technology as a possible alternative to existing crystallisation technologies for struvite production.

Chapter 3 is dedicated to the NETmix CFD simulations. In section 3.1, the geometry of the 2D ExtendedNUB model is described, as well as the characteristics of the mesh. The employed governing equations, the boundary and initial conditions and the models and solution methods chosen for the simulations are described in sections 3.2, 3.3 and 3.4, respectively. The presentation and discussion of the results is done in section 3.5, which is divided into three subsections, namely flow distribution analysis, mass transfer analysis and flow dynamics analysis.

Chapter 4 describes the experimental work carried out for this dissertation. The experimental setup used for tracer experiments, the materials and experimental conditions used and the discussion of the results obtained is done in section 4.1. In section 4.2, the characteristics of a digestate liquid fraction are discussed.

Chapter 5 is about the CFD simulations of a Y-flow distributor and is divided into the following sections: section 5.1 – geometry and mesh description; section 5.2 – governing equations used; section 5.3 – boundary and initial conditions, section 5.4 – models and solution methods; and section 5.5 – discussion of the results obtained for the mesh independence test performed to the designed geometry and for the analysis of the influence of pressure in the flow inside the distributor.

Chapter 6 introduces a new NETmix geometrical model for CFD simulations, the NETmix Entire Block model. Section 6.1 describes the geometry and mesh used for the simulations, sections 6.2 and 6.3 describe the governing equations and boundary and initial conditions, and the models and solution methods, respectively, and section 6.4 presents the results obtained for the influence of asymmetric inlet flow conditions on the pressure at the first channels of this NETmix model.

Finally, chapter 7 summarises the main conclusions drawn for this dissertation and chapter 8 presents an assessment of the work done and future work proposals.

2 Context and State of the Art

2.1 Wastewater treatment plants

The main objective of wastewater treatment plants is to guarantee that the quality of effluents meets safety standards established by regulatory authorities, so as to prevent the degradation of ecosystems and the deterioration of public health [11]. In the EU, WWTPs must follow the regulations stated in the Urban Waste Water Treatment Directive (UWWTD), in which requirements concerning the collection, the treatment, and the discharge of urban and certain industrial wastewaters are stated, as well as quality objectives and emission limit values [12]. Urban wastewaters are the ones that originate from domestic activities and include greywater (from washing machines, showers and baths), blackwater (derived from toilet waste) and sewage. Industrial wastewaters, for instance, derive from industrial activities and their compositions and quantities vary depending on the type of industry and the size of the business [13].

Wastewaters may contain several types of pollutants, such as suspended solids like sand and soil, dangerous bacteria, viruses and other microorganisms, heavy metals and other chemicals derived from industrial activities, large quantities of nutrients, primarily nitrogen and phosphorus, and undesirable pH values. Due to the diversity of these pollutants, WWTPs have several treatment stages that specifically target each one of them and are divided into two main sections, the liquid phase treatment section and the solid phase treatment section [11]. Figure 1 shows a generic process diagram of a WWTP with its various process units. A synthetic description of the several treatment stages is present in Appendix A.

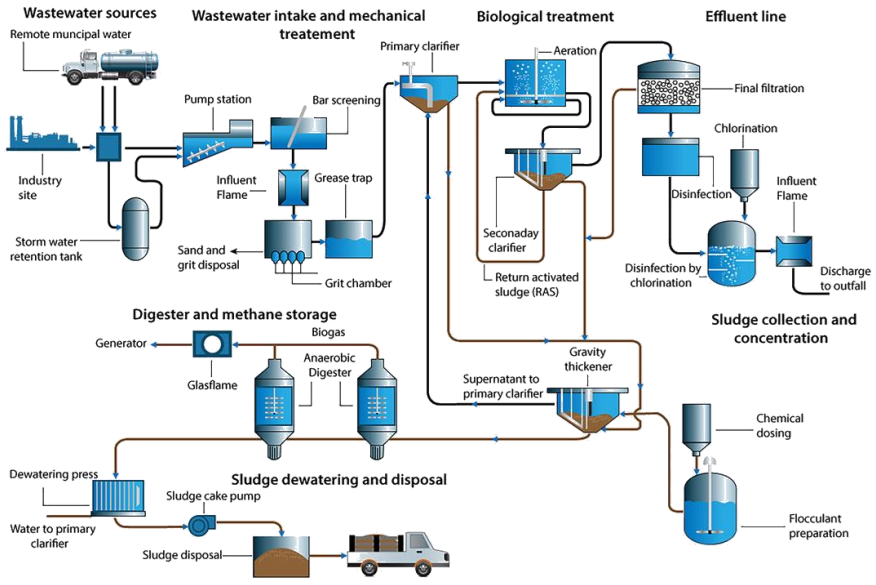

Figure 1. Generic process diagram of a wastewater treatment plant [14].

As mentioned in section 1.1, the main focus of this work is the liquid stream generated during one of the solid phase treatment steps, the digested sludge dewatering process. This sludge is known as digestate and is a by-product of the anaerobic digestion step. Dewatered sludge is normally used as a fertiliser in agricultural practices since it is composed of various elements, in particular nutrients like phosphorus, nitrogen and potassium [3]. During the dewatering process, the majority of N present in the digestate

generally goes to the liquid fraction (between 65 and 75 %). P, however, is more evenly distributed, with 55 to 65 % going to the solid digestate fraction [15].

2.2 Digestate composition

The composition of a digestate varies considerably depending on the origin of the wastewater. Some studies have investigated the composition of several digestates regarding nutrient concentrations. Maurer et al. reported concentration values of N and P for untreated digestate originated from energy crops, and for its solid and liquid fractions obtained after the dewatering process [16]. Drosg et al. also reported averaged values for five samples of digested wastewater derived from manure [15]. Moreover, Zuliani et al. described the composition of a digestate obtained from an Italian municipal wastewater [17]. These values are summarised in Table 10 of Appendix B, in which NH_4-N stands for ammoniacal nitrogen, TP means Total Phosphorus, TN is the Total Nitrogen and K is the chemical formula for potassium. Ge at al. reported TP, TN and NH_4-N values for a centrate sample originated from a Canadian wastewater treatment plant, which are summarised in Table 11 of Appendix B. As expected, different sources of wastewater originate digestates with different compositions. Energy crop digestates seem to have significantly higher concentrations of N and P than manure or municipal wastewater digestates. The municipal wastewater digestates presented the lower concentrations of N and P. Furthermore, it can be confirmed that digestate liquid fractions uptake higher quantities of N when compared to the solid fraction, and that P distribution is not as coherent when comparing liquid and solid fractions for each type of digestate. This could be due to the fact that the degree of solid/liquid separation varies according to the type of equipment used to perform the dewatering process [18].

After the dewatering process, the centrate stream is usually returned to the primary decantation stage, so as to make necessary adjustments to the dry matter concentration of the influent [11]. Recently, however, the idea of using this liquid fraction as a direct fertiliser has emerged. Nevertheless, this application has not been implemented yet due to the possible occurrence of nitrogen leaching, that is, the formation of gaseous nitrous oxide due to microbial activity, which is a greenhouse gas 300 times more potent than carbon dioxide. Moreover, this element contributes in a significant way to the pollution of aquatic ecosystems because it promotes the development of toxic algae that reduce oxygen content in waters [19]. Another problem associated to the direct application of the liquid fraction of digestates in soils is the possible presence of certain contaminants in concentrations above the legal limits for liquid fertilisers stated in the EU Regulation 2019/1009, such as heavy metals and pathogens, that could have serious environmental implications if they were to be in direct contact with soils [18].

2.3 Nutrients recovery from the liquid fraction of digestates

As seen in the previous section, applying digestate liquid fractions directly to soils is still not feasible owing to potential harmful consequences for aquatic ecosystems. An alternative way to take advantage of the nutrients present in these effluents is through the incorporation of processes in WWTPs that allow their recovery in solid form and thus close their life cycle [3].

Phosphate ions can be removed from liquid effluents through an adsorption process, in which P anions replace hydroxyl groups present in the adsorbent due to electrostatic forces and adsorption reactions. At the same time, these adsorbents leach out positively charged ions, such as calcium (Ca^{2+}) or magnesium (Mg^{2+}), into the solution. The partial dissolution of Mg^{2+} or Ca^{2+} in the adsorbate increases the pH medium and triggers the precipitation of phosphate ions in the form of calcium phosphates or struvite crystals. In this process, the adsorbents can be regenerated several times, resulting in low operational costs [20]. Nevertheless, the use of adsorption to precipitate phosphate-based compounds is recent and has only been tested at a laboratory scale [3]. Also, it leads to the generation of concentrated streams, which could be of difficult disposal [21].

Electrochemical precipitation can also be used to produce phosphate-based compounds. In this process, water is electrolysed at a cathode, resulting in the formation of hydroxide ions (OH^-) and hydrogen and consequent increase of the pH medium. At the same time, a sacrificial anode composed of Ca or Mg, for example, is oxidised by electrons under current, which results in the formation of cations (Ca^{2+} or Mg^{2+}) [22]. Again, the precipitation of the phosphate ions occurs due to the alkalinity of the medium. Depending on the nature of the cations, two insoluble minerals may precipitate, namely hydroxyapatite if the cations are Ca^{2+} [3], or struvite if the anode is made of Mg [22]. The advantages of this process are the fact that it does not require the addition of chemicals for pH control and the precipitated mineral can be removed from the cathode without the need of a separation step. Nonetheless, the P removal efficiencies obtained so far for this process are still low (below 50 %) and more research has to be done to make it economically feasible [3]. Moreover, the electrodes must be renewed quite frequently [23].

The most widely used technique to precipitate phosphate-based compounds is crystallisation [3]. In a crystallisation process, solid structures with highly organised microscopic structures are formed under specific conditions. Two main steps occur: firstly, there is a nucleation step, in which solute molecules gather to form clusters that must reach a certain size to become stable, named nuclei; then, a process known as crystal growth takes place. The ions present in the solution deposit on these nuclei until they reach the size of settling particles [6, 24]. Crystallisation has several advantages, namely a very high recovery rate, no need for supplementary materials like adsorbents, catalysts or membranes, the possibility of obtaining simultaneously value-added salts and water with high levels of purity, process stability, energy saving, and ease of scale-up to industrial levels [7].

Several minerals with phosphorus in their constitution can be precipitated from digestate liquid fractions through crystallisation, such as struvite ($Mg(NH_4)PO_4{\cdot}6H_2O$) [23], hydroxyapatite ($Ca_{10}(PO_4)_6(OH)_2$) [25] or even vivianite ($Fe_3(PO_4)_2{\cdot}8H_2O$) [26]. Nevertheless, since one of the objectives of this work is to recover P in a sustainable way for subsequent use as fertiliser, hydroxyapatite production was not considered. This mineral is normally used for biomedical applications, like bone repair and regeneration, coating of orthopedic and dental implants, or as a drug carrier [27]. Furthermore, although vivianite precipitation is linked to high P recovery rates comparatively to $Ca_{10}(PO_4)_6(OH)_2$ and $Mg(NH_4)PO_4{\cdot}6H_2O$, its applications are still very premature from a scientific point of view and so its production was also discarded [26]. Research has been recently conducted to study its use as a fertiliser in iron-deficient soils and its incorporation in lithium iron phosphate batteries [28]. In this sense, struvite was considered to be the mineral that best met the objectives of this dissertation. It is known to have great fertilising capacities

owing to its low solubility in water and to the fact that it has a slow-release rate, which minimises nutrient loss by run-off. Additionally, struvite precipitation allows the simultaneous recovery of two nutrients, namely phosphorus and nitrogen, both essential for plant growth [29]. Finally, struvite does not incorporate significant amounts of pathogens and heavy metals during its formation [6].

2.3.1 Struvite crystallisation for phosphorus and nitrogen recovery

Struvite is an orthorhombic white crystal formed by one phosphate molecule (PO_4^{3-}, HPO^{2-} or H_2PO^-), one ammonium molecule (NH_4^+), one magnesium molecule (Mg^{2+}) and six water molecules (H_2O). It has a relative density of 1.67-1.7, a molar mass of 245.53 g·mol^{-1} and a solubility product constant, K_{sp}, of $10^{-13.36}$ at 25 °C. Struvite precipitation occurs when the product of the concentrations of $H_nPO_4^{3-}$, NH_4^+ and Mg^{2+} in solution exceeds the K_{sp}, that is, when the solution is supersaturated [23]. The formation of struvite occurs in accordance with Equation 2.1, in which n can be equal to 0, 1 or 2 [21].

$$Mg^{2+} + NH_4^+ + H_nPO_4^{3-n} + 6H_2O \rightarrow MgNH_4PO_4 \cdot 6H_2O + nH^+ \quad (2.1)$$

There are several factors that affect the extent of the reaction and the purity of the final product. Firstly, since the formation of struvite is accompanied by the release of hydrogen ions, H^+, a more alkaline pH medium will favour the forward reaction direction. Several studies have reported optimum pH values for struvite precipitation. Song et al. reported that the pH of the reaction medium should be between 9.5 and 10.5 [30]. Tünay et al. suggested an optimum pH value range of 8.5-9.3 [31]. Hao et al., for instance, proposed a pH range of 9-9.5 [32]. The various ranges reported could be related to different wastewater compositions that result in different ionic strengths and activities and, consequently, affect the ideal pH range for struvite precipitation [21]. Nevertheless, it is known that pH values greater than 11 do not favour the struvite precipitation reaction as they enable the occurrence of side reactions that reduce the availability of Mg^{2+} and NH_4^+ [33].

Another factor that influences struvite formation is the molar ratios between Mg^{2+}, NH_4^+ and $H_nPO_4^{3-}$. Theoretically, this mineral is precipitated when these three ions are present in solution in equimolar concentration. However, in reality, digestate liquid fractions normally have higher concentrations of NH_4^+ and $H_nPO_4^{3-}$ comparatively to Mg^{2+}, meaning that an external magnesium source is needed to ensure the reaction takes place [25]. This, however, presents itself as a disadvantage for the production of struvite through crystallisation, because it adds to the costs of the process. The costs associated with chemical Mg sources, such as magnesium chloride ($MgCl_2$), magnesium sulphate ($MgSO_4$) or magnesium hydroxide ($Mg(OH)_2$), could be up to 75 % of the total process expenses. Still, this problem can be overcome by the use of low-cost magnesium sources, for instance, bittern, wood ash, pre-treated sea water or concentrated sea water from nanofiltration or reverse osmosis processes [6]. Studies in literature state that Mg:P molar ratios higher than 1:1 should be used to promote efficient phosphorus removal from centrate streams [21]. Quintana et al. found that increasing the Mg:P ratio enhanced the formation of struvite crystals and that the optimum Mg:P value was of 1.5:1 [34]. Nelson et al. reported an ideal Mg:P ratio of 1.6:1 [35] and Jaffer et al. stated that a magnesium source should be added in a molar ratio of 1.3 [36]. Once again, the diversity of values reported in literature could be linked to different wastewater compositions.

Regarding the influence of temperature, it is known that increasing the temperature of the reaction medium increases the K_{sp} of the reaction, leading to the formation of struvite crystals with less purity or even to their dissolution. In this sense, many studies state that the crystallisation process of this mineral should be performed in a temperature range of 25-35 °C [21].

The presence of competitive ions, especially Ca^{2+}, in the wastewater effluent should also be taken into account. Calcium ions react with orthophosphates (PO_4^{3-}) to form calcium phosphates and hydroxyapatite, which significantly reduces the amount of struvite that is formed and its purity. Tao et al. showed that Ca:Mg molar ratios inferior to 0.2 did not jeopardise the quality of struvite, but values higher than 0.2 resulted in a decrease in the purity of the crystals formed and slowed down the nucleation process [37]. Furthermore, Ca:Mg ratios higher than 1 inhibit the nucleation process altogether [38].

Crystallisation processes for P and N recovery through struvite precipitation already have some scientific maturity and full-scale technologies have already been implemented in WWTPs. Some examples of these technologies are Crystalactor®, Ostara Pearl®, NuReSys®, Phosnix and PHOSPAQ™ [39, 40]. A brief description of these technologies is present in Appendix C. Although these technologies are known to have satisfactory P recovery efficiencies, the selling price of the produced struvite becomes quite expensive owing to high process costs associated with the need for chemicals like acids, precipitation agents, caustics, resins or seed materials if the technologies use fluidised bed reactors [8]. In addition, some of them consist of stirred tanks that require a constant energy supply for the operation of the stirring blade, which results in high energy costs.

In this sense, this work proposes the use of the NETmix technology as a more economically viable alternative to the technologies presented above, since it would not require the use of resins or seed materials, and it is a static mixer, so no external force is required to promote mixing. The characteristics of this novel reactor will be presented next.

2.4 NETmix reactor

The NETmix reactor is a patented static mixer developed at the Associate Laboratory LSRE-LCM in 2005 [41]. Its network consists of repeating unit cells, each one composed of one chamber, two inlet half-channels and two outlet half-channels, oriented at a 45º angle from the main flow direction. There are two possible configurations for these unit cells, namely a 2D configuration, in which the chamber is cylindrical and the channels have a prismatic form, and a 3D configuration, in which the chamber is spherical and the channels are cylindrical [9]. Examples of 2D and 3D NETmix networks can be seen in Figure 2, as well as characteristic NETmix reactor dimensions.

Mixing inside the NETmix network is achieved without the need for an external force due to its distinct geometry, which enhances the hydrodynamic interaction between opposing jets when they meet at the centre of the chambers. However, mixing can only be achieved when the Reynolds number, Re, of the flow is above a certain value, known as the critical Reynolds number, $\mathrm{Re}_c = 200$. For Re < Re_c, a fully developed laminar flow can be observed, in which no mixing between the two halves of the chambers occurs. For Re > Re_c, the flow evolves into a self-sustained fully chaotic and dynamic oscillatory flow

and a high mixing degree is achieved. Vortices are formed inside the NETmix chambers that engulf the streams that emerge from the two unit cell inlets, promoting the occurrence of micromixing [42].

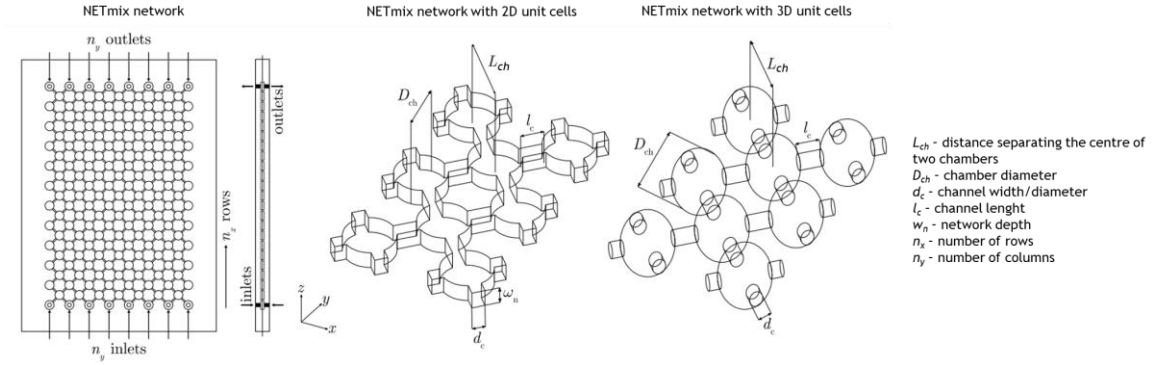

Figure 2. Schematic representations of the NETmix network (adapted from [9]).

The NETmix reactor has several competitive advantages, namely the possibility of efficiently controlling macro and micromixing, the fact that it allows a careful distribution of reactants in accordance with the reaction stoichiometry and control of the flowrate at the inlets [9], a large heat transfer area, making it suitable for endothermic or exothermic reactions [43], its network can be easily scaled-up or numbered-up in accordance to the intended purpose [9] and it operates at relatively low pressure drops [44].

This static mixer has been studied for several applications, such as for homogenous photo-Fenton degradation of antibiotics in water streams [45], as a photocatalytic reactor for the degradation of volatile organic compounds from air streams [46], bromate reduction [47], oxytetracycline oxidation [48], and arsenic oxidation [49], for the continuous production of carbon dioxide hydrates [9], for the production of Pickering emulsions [50] and for the continuous production of melamine-formaldehyde microcapsules [51]. In addition, the NETmix already has an industrial application, which is the production of synthetic nanocrystals of hydroxyapatite for the manufacture of medical devices with purity levels close of 100 %. It is sold under the commercial name of nanoXIM by the Portuguese company Fluidinova S.A [52]. This attests to the capacity of the NETmix technology to produce crystalline compounds with a very narrow size distribution, evidencing its great performance as a reactor and a mixer. This allows to infer a possible success of this technology in the production of struvite crystals.

So far, the majority of the single-phase studies conducted in the NETmix reactor have been for symmetric inlet flow conditions, that is, the same Reynolds number is set in each inlet. Hence, this work intends to evaluate the performance of the NETmix reactor when operated with two different Reynolds numbers at the inlets, that correspond to two different flow regimes in the reactor, and validate its use for the production of struvite through a crystallisation process. Note that this static mixer must be able to efficiently mix a highly diluted digestate liquid fraction stream (Re > Re_c) and a stream with a high concentration of Mg (Re < Re_c), in order to promote the formation of the struvite crystals.

3 NETmix CFD simulation

Computational Fluid Dynamics is a powerful tool that allows the prediction of the way fluids flow in a given geometry. These predictions are made based on the resolution of three conservation equations regarding mass, momentum and energy, and also on the definition of boundary and initial conditions and fluid properties [53].

In this work, CFD simulations were performed using the commercial package ANSYS/Fluent 2022 R2 to study the behaviour of a liquid flow inside the NETmix reactor when imposing asymmetric inlet boundary conditions. The objective of these studies was to assess the mixing performance of the NETmix reactor when the velocities at the two inlets are different. In this way, dynamic two-dimensional (2D) tracer experiments were simulated and certain parameters were calculated and evaluated, namely the intensity of segregation and the averaged flowrate in the channels, the frequency spectra and the power spectra obtained for the NETmix downstream chamber and the intensity of turbulence in all chambers for different inlet conditions.

3.1 Geometry and mesh

The CFD simulations were performed applying the NETmix Unit Block (NUB) concept developed by Fonte et al., in which only a small section of the NETmix network is simulated [44]. As previously mentioned, this static mixer is formed by the repetition of unit cells, each one composed of a chamber with four adjacent half-channels, two inlets and two outlets. The NUB model used in this work, called the 2D ExtendedNUB, only represents 9 rows and 3 columns of the NETmix. It is normally used as an alternative to simulating the whole reactor in order to reduce simulation time. Additionally, it has been previously verified that the flow inside the NETmix presents a repetitive nature due to its peculiar geometry, which allows the simulation of only a segment of its network without compromising the reliability of the predictions [54].

The 2D ExtendedNUB model is represented in Figure 3. In Figure 3a one can see the inlets and outlets of the ExtendedNUB geometry. In addition, periodic boundary conditions were defined on the half-chambers of the first and third columns, which will be further explained in section 3.3. Lines were drawn at the half-length of all channels to obtain the velocity magnitude of the fluid and the mass fraction of tracer along the NETmix so as to determine the segregation intensity along the reactor. Finally, points were defined at the centre of the chambers to determine the velocity magnitude in the x and y-directions. This was done to obtain the power and frequency spectra for chamber C8 and calculate the intensity of turbulence along the chambers and evaluate the mixing performance of the NETmix while operating with asymmetric inlet velocities.

Figure 3b shows the characteristic dimensions of the NETmix, namely the chamber diameter, D, and the length and width of each channel, represented by l and d, respectively. The width of the NETmix was not defined since the simulations were done in two dimensions. The values defined for each dimension were the following: $D = 6.75$ mm, $d = 1$ mm and $l = 2$ mm. These values were chosen in accordance with a relationship established by Matos et al. that states that the ratio between D and d should be between

6.65 and 6.85 so that perfect mixing in the NETmix is achieved [54]. It is also important to mention that the length of the inlet and outlet channels is half the length of the other channels. Moreover, Figure 3b shows the identification of the chambers of the central column and of the channels. The ones on the left side of the NETmix are identified with the letter '*l*' and the ones on the right side with the letter '*r*'.

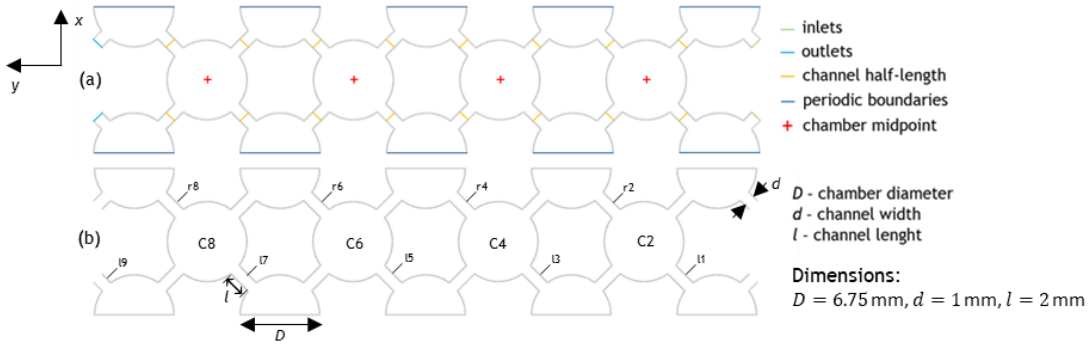

Figure 3. (a) Identification of the surfaces in the 2D ExtendedNUB and (b) characteristic dimensions and channels and chambers identification.

In this work, the mesh independence test was not performed since this mesh was already validated in previous works for single-phase [55] and two-phase flows [10]. The mesh element size, Δx, is of 62.5 µm, has 97818 mixed cells and an area of 358.5 mm^2.

3.2 Governing equations

As mentioned before, CFD simulations are calculated based on conservation laws. Regarding mass conservation, the general continuity equation that represents it is present in Equation 3.1 [56].

$$\frac{\partial \rho}{\partial t} + \nabla \cdot (\rho \vec{u}) = S_m \tag{3.1}$$

In Equation 3.1, ρ represents the density of the fluid under study, t is the time, $\vec{u}$ is the velocity vector and S_m is a source that could represent the mass transferred from the discrete phase to the continuous phase and also other sources [56]. In the present case, the simulations were conducted assuming that the fluid was incompressible and only a single liquid phase was considered, which means that $\frac{\partial \rho}{\partial t} = 0$ and $S_m = 0$, so the continuity equation becomes $\nabla \vec{u} = 0$.

Concerning momentum conservation, the respective Navier-Stokes equation is present in Equation 3.2, in which p_s is the static pressure, $\bar{\bar{\tau}}$ is a stress tensor, calculated by Equation 3.3, $\rho \vec{g}$ is the gravitational body force and $\vec{F}$ is a term that accounts for external body forces that may result from interaction between phases. In this work, these two last terms were not accounted for since the effect of gravity was not considered as both fluids had the same physical properties and the simulations were single-phased [56].

$$\frac{\partial}{\partial t}(\rho \vec{u}) + \nabla \cdot (\rho \vec{u} \vec{u}) = -\nabla p_s + \nabla \cdot (\bar{\bar{\tau}}) + \rho \vec{g} + \vec{F} \tag{3.2}$$

$$\bar{\bar{\tau}} = \mu \left[(\nabla \vec{u} + \nabla \vec{u}^T) - \frac{2}{3} \nabla \cdot \vec{u} I \right] \tag{3.3}$$

In Equation 3.3, the variable I represents the unit tensor, μ is the dynamic viscosity of the fluid, and the second term on the right side of this equation is related to the effect of volume dilation. Since the flow was considered incompressible, this term becomes equal to zero [56].

With the assumptions stated above, the momentum conservation equation could be rewritten as it is shown in Equation 3.4 [56].

$$\rho\left(\frac{\partial\vec{u}}{\partial t}+\vec{u}\cdot\nabla\vec{u}\right)=-\nabla p+\nabla\cdot\left(\mu(\nabla\vec{u}+\nabla\vec{u}^{T})\right) \tag{3.4}$$

Moreover, it was considered that the flow was isothermal, so the energy conservation equation was not solved [56].

Finally, as tracer experiments were simulated, it was necessary to take into account a species transport equation that predicts locally the mass fraction of a certain species, Y_i. The generic form of this convection-diffusion equation is present in Equation 3.5 [56].

$$\rho\left(\frac{\partial Y_i}{\partial t}+\nabla\cdot(\vec{u}Y_i)\right)=-\nabla\cdot\vec{J_\iota}+R_i+S_i \tag{3.5}$$

$\vec{J_\iota}$ is the diffusion flux of a certain species i, R_i is the rate of formation of that species by chemical reaction and S_i represents the amount of i that is added to the continuous phase from the dispersed phase and other sources. These last two terms were not considered since no chemical reaction was simulated and, as mentioned before, only a single liquid phase was simulated. The diffusion flux was calculated from Fick's Law present in Equation 3.6 [56].

$$\vec{J_\iota}=-\rho D_{i,m}\nabla Y_i-\rho D_{T,i}\frac{\nabla T}{T} \tag{3.6}$$

The first term on the right side of Equation 3.6 is related to the influence of concentration gradients in the mass diffusion process and $D_{i,m}$ is the mass diffusion coefficient that assumed a value of 10^{-9} $m^2 \cdot s^{-1}$. The second term, in which $D_{T,i}$ is the Soret diffusion coefficient, represents the influence of temperature gradients in the mass diffusion process and was not considered in this work [56]. Finally, T refers to temperature.

With the assumptions made for the species transport phenomenon, it was possible to rewrite Equation 3.5 in the following form:

$$\frac{\partial Y_i}{\partial t}+\nabla\cdot(\vec{u}Y_i)=D_{m,i}\nabla^2 Y_i \tag{3.7}$$

3.3 Boundary and initial conditions

The governing equations shown in the previous section are all partial differential equations since they relate a physical quantity with its rate of change in a certain domain. In order to solve this type of equations, it is necessary to define initial and boundary conditions to restrict the evolution of the solution so that it does not diverge [57].

Boundary conditions restrain the spatial domain in which the differential equations are to be integrated. In this work, the average velocity magnitude, $\bar{u}_{in}$, in both inlet channels was calculated with the aid of Equation 3.8.

$$\mathrm{Re} = \frac{\rho \bar{u}_{in} d_h}{\mu} \tag{3.8}$$

Re is the Reynolds number, defined as the ratio between inertial and viscous forces and used to describe the single phase flow regime of a Newtonian fluid [58]. d_h is the hydraulic diameter, which is given by Equation 3.9.

$$d_h = \frac{4A}{P} = \frac{2wd}{w+d} \tag{3.9}$$

In Equation 3.9, A is the cross-sectional area of the channel, P is the wet perimeter and w is the depth of the NETmix geometry. Since the simulations were performed in 2D, w is considered to be infinite, which means that $w \gg d$ and so the hydraulic diameter becomes equal to $2d$.

Additionally, water was defined as the working fluid, so ρ assumed a value of 998.2 kg·m^{-3} and μ a value of 1.003 mPa·s. Moreover, it is important to mention that a fully developed parabolic velocity profile was defined at both inlets according to Equation 3.10, which is normally used to describe 2D flows of Newtonian fluids between large parallel plates [59].

$$u(r) = u_{max}\left[1 - \frac{4r^2}{d^2}\right] \tag{3.10}$$

In this equation, u_{max} corresponds to the maximum fluid velocity that occurs in the middle of the plates and can be calculated in the following way: $u_{max} = \frac{3}{2}\bar{u}_{in}$. The r variable represents the distance to the axis of the channel [59]. It is important to highlight that the left-hand side inlet is inclined +45º in relation to the y-axis and the right-hand side inlet has an inclination of -45º relatively to the same axis.

Regarding the boundary conditions imposed on the outlets and the walls of the ExtendedNUB geometry, it was defined that the gauge pressure, that is the pressure relative to atmospheric pressure, in each outlet would be equal to zero and that the backflow mass fraction of tracer would be of 0.5. A no-slip condition was defined at the walls. This condition means that the velocity of the fluid in direct contact with the wall is the same as the velocity of that same wall [58]. In this case, $\vec{u} = 0$.

Moreover, in order to take advantage of the periodically repeating nature of the flow inside the NETmix reactor, translational periodic boundary conditions were imposed on the right-hand side and left-hand side half-chambers, as it can be seen in Figure 3, so as to connect the flow in each pair of opposite half-chambers. This means that the flow conditions that were verified in the cells adjacent to one periodic wall were used to calculate the flow on the opposite wall.

Finally, as mentioned before, it was also necessary to define the initial conditions of the simulations. The initial state of the simulations corresponded to the steady state solution obtained when all the time-dependent terms of the governing equations were set equal to zero [42]. In addition, all the initial guesses for the space domain variables were likewise set to zero.

Since tracer experiments were simulated, it was necessary to define at the inlets the mass fraction of both simulated species, namely water and a fluid with the same physical properties as water, the tracer. In this sense, a mass fraction of tracer of 1 was defined in the right-hand side inlet and of 0 in the other inlet.

Table 1 summarises the simulated cases. Three different ratios between the Reynolds numbers of both inlets, Re_l for the left and Re_r for the right inlet, were studied, namely ratios of 10, 100 and 1000. The values chosen for Re_l were always above the critical Reynolds number of 200, which corresponds to a self-sustained chaotic flow in the NETmix when this Re is considered in both inlets. The Re_r values always corresponded to a fully developed laminar regime, which means that $\mathrm{Re}_r < \mathrm{Re}_c$.

Table 1. Cases studied for asymmetric inlet flow conditions in the ExtendedNUB geometry.

Cases	1	2	3	4	5	6
$\mathrm{Re}_l/\mathrm{Re}_r$	1000	100	10	1000	100	10
Re_l	600	600	600	1200	1200	1200
Re_r	0.6	6	60	1.2	12	120

3.4 Models and solution methods

The simulations performed for the cases described in Table 1 were solved by a pressure-based solver, the flow scales were fully resolved, and so no turbulence sub-grid scale models were defined. The species transport equation was solved together with the flow equations. Additionally, it was necessary to define the solution methods used in these simulations. These methods control the way that the time and space domains are discretised during the simulations. For the pressure-velocity coupling the SIMPLEC method was used. Regarding spatial discretisation, the Least Squares Cell Based method was used for gradient discretisation, the PRESTO! scheme for pressure discretisation, the Third-Order MUSCL scheme for momentum discretisation and the Second Order Upwind scheme for the interpolation of the tracer flow. Since the simulations were performed in transient state, the First Order Implicit transient formulation was adopted. Moreover, it was necessary to determine the appropriate time step, Δt, the smallest unit of time that is resolved in a simulation, for each case by implementing the Courant-Friedrichs-Lewy (CFL) condition. This condition states that the Courant number, Co, given by Equation 3.11, should be inferior to 1 for an iterative process to converge in a stable way to the correct solution of the partial differential equations. In other words, so that the solution of the difference equation can converge to the solution of the respective differential equation [60].

$$\mathrm{Co} = u_{max}\Delta t/\Delta x \tag{3.11}$$

In Equation 3.11, u_{max} was calculated in the following way: $u_{max} = \max(1.5\bar{u}_{in})$, since both inlets had different average inlet velocities and a higher u_{max} leads to a smaller Δt and so the discretisation process is more accurate. The maximum number of iterations per time step was set as 40 and the convergence criteria was that all conditions should be met in each time step (constant residuals of 1×10^{-5}).

Finally, the duration of the simulations was also defined through the calculation of the passage time in the 2D ExtendedNUB geometry, τ_{2D}, calculated by Equation 3.12.

$$\tau_{2D} = A_{2D}/\left((\bar{u}_{in,l} + \bar{u}_{in,r})\, d\right) \quad (3.12)$$

In Equation 3.12, A_{2D} represents the area of the ExtendedNUB geometry (358.5 mm^2). Then, it was defined that the simulations would last 5 passage times, which allowed the determination of the number of time steps, N, necessary per simulation, as it is shown in Equation 3.13.

$$N = 5\, \tau_{2D}/\Delta t \quad (3.13)$$

Table 2 shows the values of Δt, τ_{2D} and N obtained for each case. A Courant number of 0.5 was assumed to obtain the time steps for each case.

Table 2. Values of Δt, τ_{2D} and N obtained for each case.

Cases	Δt/s	τ_{2D}/s	N
1	6.94×10^{-5}	1.19	85597
2		1.18	84835
3		1.08	77894
4	3.47×10^{-5}	0.59	85597
5		0.59	84835
6		0.54	77894

3.5 Results and discussion

3.5.1 Flow distribution analysis

Firstly, it was necessary to analyse the flow distribution throughout the NETmix network, so as to assess its ability to obtain similar outlet flowrates when asymmetric inlet conditions are imposed. Note that one must ensure that the outlet streams present similar conditions in terms of composition and flow when performing a chemical reaction in this reactor. As it is shown in Figure 3, lines were drawn at the middle of all channels present in the ExtendedNUB geometry and the average velocity magnitude in each line was computed for each time step during the simulations of all six cases. Then, the average volumetric flowrate was determined knowing that it is calculated by multiplying the respective average velocity magnitude by the cross-sectional area of each channel, $A = wd$. Since the simulations were performed in 2D, the ANSYS Fluent program assumed a default value of 1 m for the width to calculate this variable.

Figure 4 shows the variation of the time-averaged normalised flowrate, $q^*_{m,i}$, with the NETmix channel number for cases 1 to 6, calculated with Equation 3.14. The $q_{m,i}$ variable is the time-averaged flowrate in each channel, with the index m being equal to l (left side) or r (right side) and i assuming integer values between 0 and 9, that correspond to the numeration of the channels shown in Figure 3, and $\bar{q}_{outlet}$ is the average outlet flowrate in the ExtendedNUB geometry, calculated as $\bar{q}_{outlet} = (q_{l,9} + q_{r,9})/2$.

$$q^*_{m,i} = q_{m,i}/\bar{q}_{outlet} \quad (3.14)$$

It should be mentioned that the inlet channels are represented by the number 0 in the x-axis. The bars present in all graphs of Figure 4 represent the standard deviation of q^* throughout the duration of the simulations for each channel. In all cases studied, one can see that the normalised flowrate values in opposite channels along the ExtendedNUB become closer until they reach values close to 1 at the outlets. Also, the behaviour of both plots of each case are symmetric.

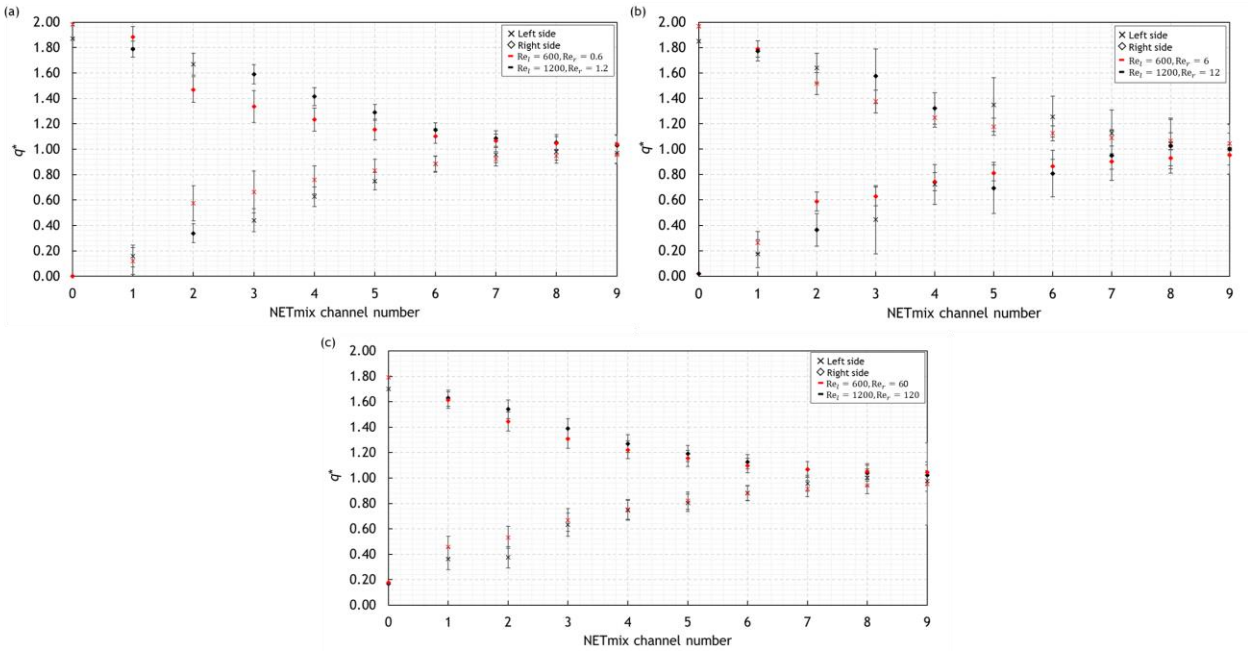

Figure 4. Variation of q^* along the NETmix channels for (a) case 1 ($Re_l = 600$ and $Re_r = 0.6$) and case 4 ($Re_l = 1200$ and $Re_r = 1.2$), (b) case 2 ($Re_l = 600$ and $Re_r = 6$) and case 5 ($Re_l = 1200$ and $Re_r = 12$), and (c) case 3 ($Re_l = 600$ and $Re_r = 60$) and case 6 ($Re_l = 1200$ and $Re_r = 120$).

These results show that this static mixer is able to generate a uniform flow distribution inside its network and attain the desirable condition of similar outlet flowrates for various inlet conditions. Nevertheless, for the cases with $\mathrm{Re}_l = 1200$, the difference between both outlet flowrates is usually smaller than the ones obtained for the cases with $\mathrm{Re}_l = 600$. Higher Re_l values increase the dynamics of the flow, leading to a higher mixing degree of both fluids in the chambers and a more homogenous flow distribution.

Furthermore, for all cases except case 2, the $q^*_{r,i}$ values are normally higher than the $q^*_{l,i}$ values, apart from the ones obtained at the inlets. Also, most cases present similar flow distribution patterns with minor differences in q^* values of upstream channels. Velocity magnitude contour maps were obtained for each case and for five normalised simulation times, in order to better understand this phenomenon. These are present in Figures 5 and 6. The scales shown in these figures are in logarithmic form.

One can see that, in cases 1 and 3 (Figures 5a and 5c), there is the formation of an eddy on the left halve of chamber C2, that forces the current coming from the right channel up the same side. Nonetheless, the elements of fluid that go up the *l2*-channel already have a considerable velocity due to the recirculation effect caused by that same eddy. From this point onwards, the $q^*_{r,i}$ are always higher than the $q^*_{l,i}$, but their values approximate along the ExtendedNUB network due to the formation of eddies in the remaining chambers. Regarding case 2, the formation of the eddy appears to happen on the right halve of chamber C2, resulting in the redirection of the flow coming from the *r1*-channel to the *l2*-channel, thus explaining the opposite behaviour seen in Figure 4b in relation to the other cases. This can be justified by the fact that the jet coming from the *l1*-channel does not have sufficient kinetic energy to counteract the flow direction of the opposite jet that has a higher velocity. For case 3, the formation of the eddy on the left side is related to the fact that the jet coming from the *l1*-channel already has a sufficiently high kinetic energy to force the jet coming from the *r1*-channel to go up the

same side. For case 1, however, it would be expected that the vortex would be formed on the same side as in case 2. This unexpected opposite behaviour could be related to the very asymmetric inlet conditions used in this case, which are $\mathrm{Re}_l = 600$ and $\mathrm{Re}_r = 0.6$. As it can be seen in the contour maps of Figure 5a, the velocity magnitude along channel *l1* is very close to zero, which could lead to the occurrence of backflow in this channel and consequently the formation of the eddy on the left side of chamber C2. Concerning case 3, a slightly more chaotic behaviour can already be seen in chamber C8, since the shape of the flow is not preserved in this chamber. This can be explained by the increase of Re_r, that results in a higher dynamic transfer between the two halves of the ExtendedNUB chamber comparatively to cases 1 and 2. As last, the flow along the channels in all three cases preserves its shape and the flow distribution is a gradual process.

The velocity magnitude contour maps obtained for cases 4 to 6 (Figure 6) clearly show a more predominant chaotic behaviour of the flow inside the ExtendedNUB, related to the increment of Re_l, and the formation of more eddies with smaller dimensions in upper chambers. Although in these cases the flowrate values in opposite channels only start to get closer for higher channel numbers comparatively to the cases with $\mathrm{Re}_l = 600$, the greater turbulence causes the flow to partially lose its shape and this contributes to the homogenisation of the flowrates in the outlet channels of higher chambers. In addition, it is possible to conclude that, in these cases, the influence of Re_r is not clearly visualised in downstream chambers when one compares their respective velocity magnitude contour maps, since the flow already acquires a predominant self-sustained chaotic behaviour from around $t/\tau = 1.00$ in chamber C4. In addition, for cases 4 and 5, there is the formation of an eddy on the right halve of chamber C2, due to the reasons mentioned above. In case 6, the formation of the eddy in chamber C2 occurs on the left side, as it happens in case 3.

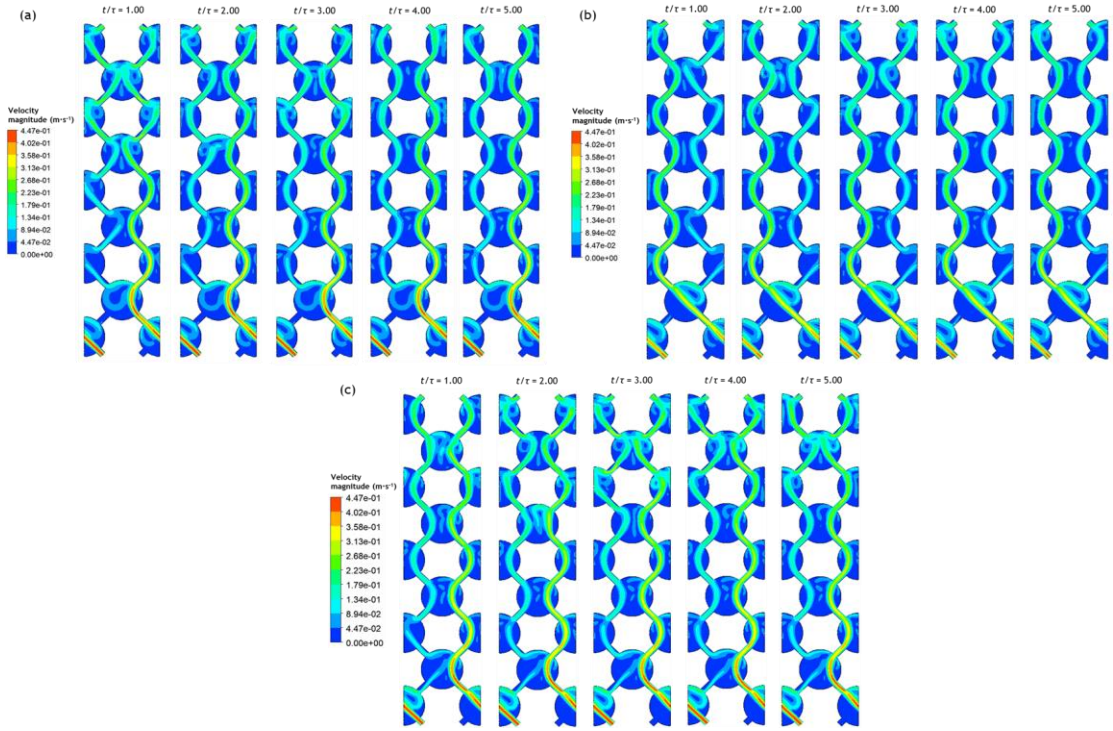

Figure 5. Velocity magnitude contour maps for cases (a) 1 ($Re_l = 600$ and $Re_r = 0.6$), (b) 2 ($Re_l = 600$ and $Re_r = 6$) and (c) 3 ($Re_l = 600$ and $Re_r = 60$).

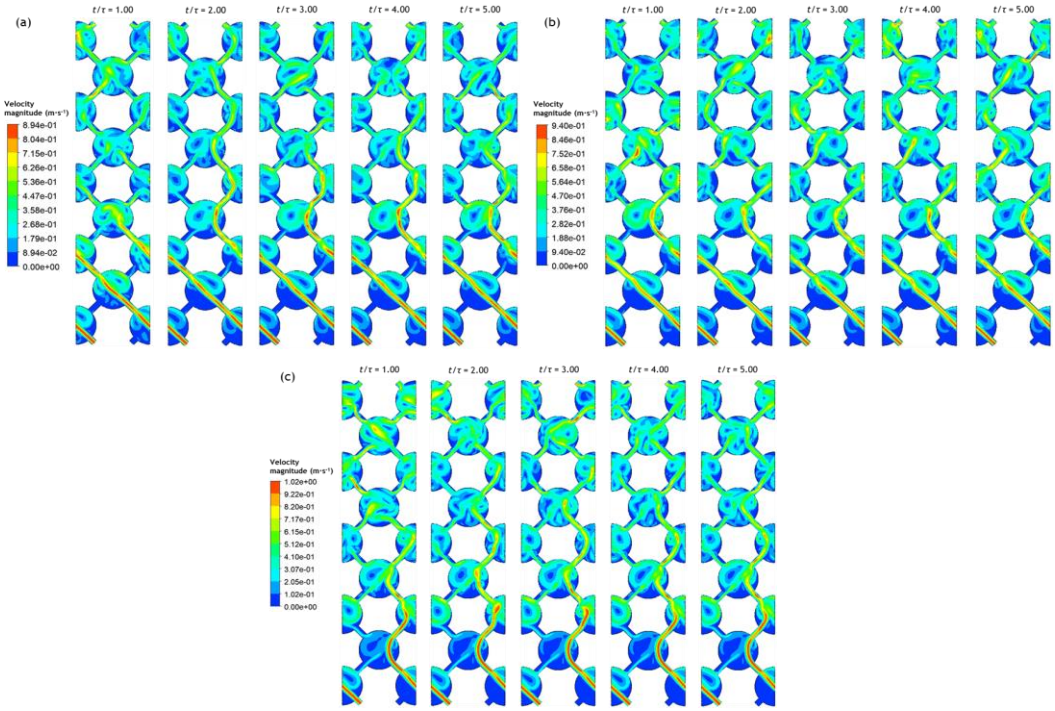

Figure 6. Velocity magnitude contour maps for cases (a) 4 ($Re_l = 1200$ and $Re_r = 1.2$), (b) 5 ($Re_l = 1200$ and $Re_r = 12$) and (c) 6 ($Re_l = 1200$ and $Re_r = 120$).

3.5.2 Mass transfer analysis

After evaluating the flow distribution inside the ExtendedNUB geometry and concluding that in all cases it was possible to obtain similar flowrates at both outlets, it was necessary to study the mass transfer phenomenon between the tracer and water fluids. To do so, the segregation concept was taken into account.

In a mixing process of two miscible liquids, two phenomena occur. Firstly, both fluids start to break up into smaller sections due to the existence of an external mechanical force or of mixing elements that redirect the flow direction. Simultaneously, molecular interdiffusion occurs between the two fluids, which ultimately leads to an uniformisation of the concentration in the domain [61]. Two opposite segregation states can be defined: a completely segregated state, in which no diffusion occurs between fluids, and a perfectly mixed state, in which instantaneous contact between both fluids occurs at a molecular level [62]. The segregation state can be characterised by the intensity of segregation, I_s, defined by Danckwerts as the measure of the deviation of the concentration of a portion of fluid from homogeneity. This statistical measure was determined with the aid of Equation 3.15 [61].

$$I_s = \frac{\sigma_a^2}{\bar{x}_a \cdot \bar{x}_b} = \frac{\sigma_b^2}{\bar{x}_a \cdot \bar{x}_b} = \frac{\sigma_a^2}{\bar{x}_a(1-\bar{x}_a)} = \frac{\sum_{n=1}^{N}(x_a - \bar{x}_a)^2}{\bar{x}_a(1-\bar{x}_a)N} \tag{3.15}$$

In Equation 3.15, σ_a^2 represents the variation of the mass fraction of a species A, x_a, σ_b^2 the variation of the mass fraction of a species B, x_b, $\bar{x}_a$ is the average mass fraction of A in a mixture of A and B and $\bar{x}_b$ is the average mass fraction of B. Also, N represents the number of experimental measurements. For the two opposite segregation states mentioned above, I_s assumes a value of 1 for a completely segregated

state and a value of 0 for a perfectly mixed state. It is expected that its value decreases as both liquids are progressively mixed.

In this work, as the inlet flowrates were different, the ideal mass fraction of tracer that would be obtained in the NETmix if perfect mixing was achieved was calculated by Equation 3.16. $x_{t,m}$ represents the mass fraction of tracer at the right and left inlets whether m is equal to r or l, respectively, and $\bar{x}_t$ is the mass fraction of tracer that would be obtained in a perfectly mixed state.

$$\bar{x}_t = \frac{x_{t,l} q_{l,0} + x_{t,r} q_{r,0}}{q_{l,0} + q_{r,0}} \tag{3.16}$$

For $\mathrm{Re}_l/\mathrm{Re}_r = 10$, $\bar{x}_t = 0.1$, for $\mathrm{Re}_l/\mathrm{Re}_r = 100$, $\bar{x}_t = 0.01$, and for $\mathrm{Re}_l/\mathrm{Re}_r = 1000$, $\bar{x}_t = 0.001$.

Hence, the variation of the intensity of segregation for each channel was determined over time and then a time-averaged I_s was calculated for each channel and each case studied. Figure 7 shows the variation of the normalised I_s, represented by I_s^*, calculated by Equation 3.17, with the NETmix channel number for all six cases. The y-axis in this figure is in logarithmic form.

$$I_s^* = \frac{I_s^{m,i}}{(I_s^{l,2} + I_s^{r,2})/2} \tag{3.17}$$

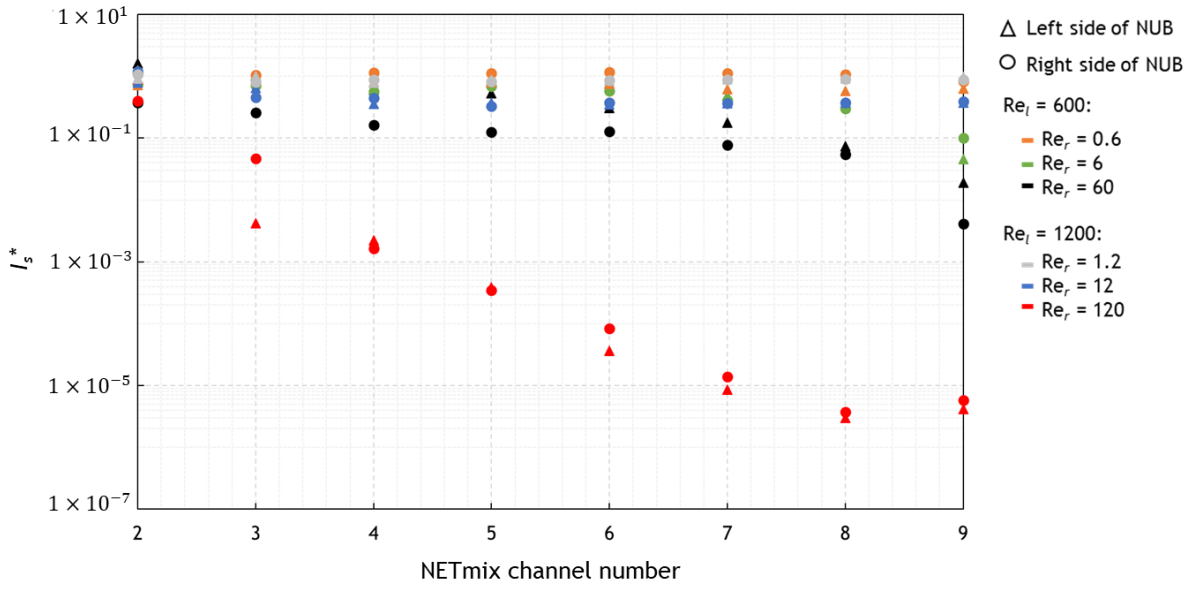

Figure 7. Variation of I_s with the NETmix channel number.*

Firstly, it should be mentioned that the I_s values for channels 1 were not considered since little contact between both fluids occurs at this point. Moreover, normalised I_s values were determined in order to better evaluate the mixing tendency along the reactor. By analysing Figure 7, one can see that the left and right-hand side I_s^* values are generally similar for all cases studied. This attests to the NETmix's ability to equally distribute the flow along its network. Only cases 3 and 6 show a higher divergence of opposite I_s^* values in upstream channels ($\mathrm{Re}_l = 600$ and $\mathrm{Re}_r = 60$ and $\mathrm{Re}_l = 1200$ and $\mathrm{Re}_r = 120$).

In addition, by comparing the plots with $\mathrm{Re}_l = 600$, it is notorious that the increase of Re_r results in a decrease of the I_s^* values for the same channel number. The same can be said for the plots with

$\mathrm{Re}_l = 1200$. Higher Re values mean that the fluid has a higher kinetic energy and so the flow dynamics increases. This results in the formation of more eddies and an enhancement of the mixing degree in the reactor with a consequent decrease of I_s^*.

Furthermore, the comparison of plots with the same $\mathrm{Re}_l/\mathrm{Re}_r$ shows that, as expected, higher Reynolds on both inlets of the ExtendedNUB enhance the dynamic behaviour of the flow and, consequently, higher mixing degrees and lower intensities of segregation are achieved. The greatest difference between I_s^* values is observed for the cases with a Reynolds ratio of 10 (black and red plots in Figure 7).

Finally, it should be referred that the decrease of I_s^* along the NETmix channels is more pronounced for case 6 ($\mathrm{Re}_l = 1200$ and $\mathrm{Re}_r = 120$), from values close to 1 to values < 1×10^{-5}. This could mean that the mixing in this case was the most efficient. Although not so obvious, other curves also present a decreasing tendency. Table 11 in Appendix D shows the I_s^* obtained for the 2nd and 9th channels and proves that gradual mixing of both fluids occurs in all cases, still it does not appear to be significant for the cases with a Reynolds ratio of 1000.

A disadvantage of the concept of intensity of segregation is that it does not take into account how concentration gradients are distributed throughout the reactor, i.e., it does not quantify flow homogeneity (only species homogeneity). In this sense, mass fraction of tracer contour maps were taken for each case (Figures 8 and 9), with the intent of validating the observations stated above. The scales shown in these figures are in logarithmic form. By comparing the contours of cases 1, 2 and 3 with the ones of cases 4, 5 and 6, it is notorious that the downstream chambers and channels in the last cases have a uniform colour distribution (which corresponds to values close to the respective $\bar{x}_t$) and that does not happen for the first set of cases, in which gradient of colours can be observed. Hence, a more uniform concentration of tracer in downstream NETmix chambers for the cases with $\mathrm{Re}_l = 1200$ is obtained and, consequently, a more effective mixing. The cases with $\mathrm{Re}_l = 600$ present higher concentration gradients along the reactor, which could be due to a less dynamic flow behaviour.

Additionally, as previously mentioned, Figure 7 seems to show that mass transfer between the tracer and water phases is low for the cases with a $\mathrm{Re}_l/\mathrm{Re}_r$ of 1000 as the I_s^* values do not decrease significantly. However, when observing the contour maps of x_t in Figures 8a and 9a, one notices that certain portions of fluid have an ideal concentration of tracer for case 1 (from $t/\tau = 3.00$) and, for case 4, from chamber C4 onwards an almost homogenised state is evident also at $t/\tau = 5.00$. This allows to better understand the behaviour of the orange and grey curves of Figure 7. As in both cases the velocity at the tracer input is 1000 times lower than the velocity at the water input, portions of fluid with high tracer concentrations (represented by the dark red colour) are not dragged along the NETmix and significant mass transfer between the two fluids already occurs at the second row of the ExtendedNUB. Correspondingly, a relatively high mixing degree is already noticeable in channels *r*2 and *l*2 of the ExtendedNUB geometry, denoted by the presence of portions of fluid with an orange colour. Therefore, this results in a small variation of x_t and, consequently, of I_s^* along the remaining channels.

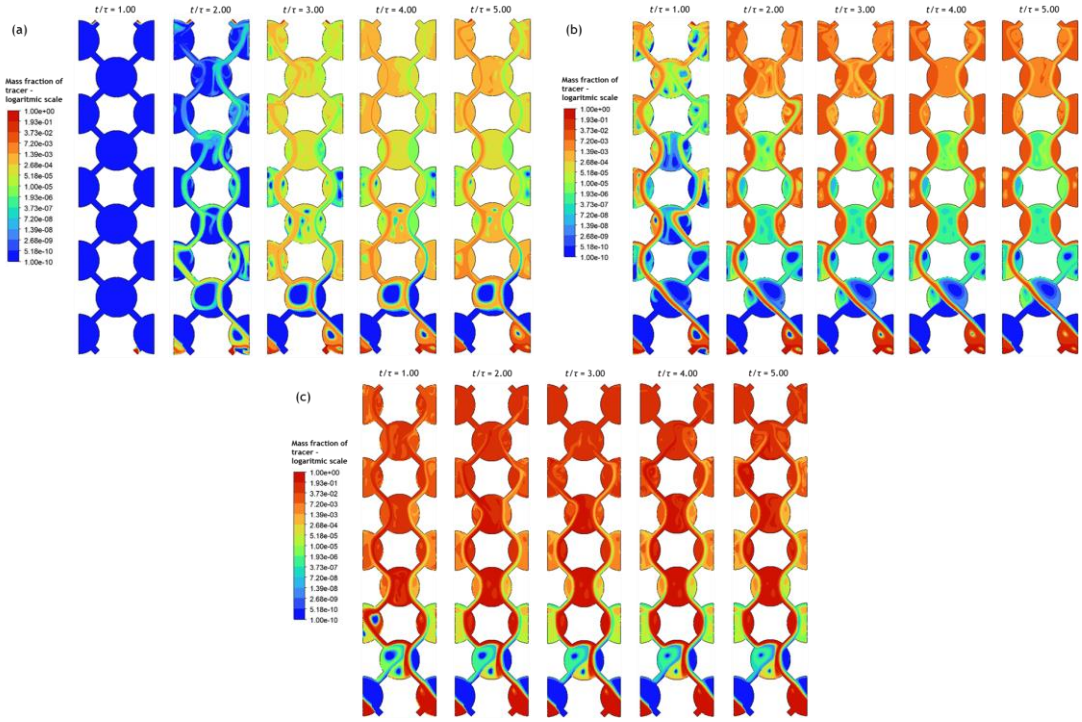

Figure 8. Tracer mass fraction contour maps for cases (a) 1 ($Re_l = 600$ and $Re_r = 0.6$), (b) 2 ($Re_l = 600$ and $Re_r = 6$) and (c) 3 ($Re_l = 600$ and $Re_r = 60$).

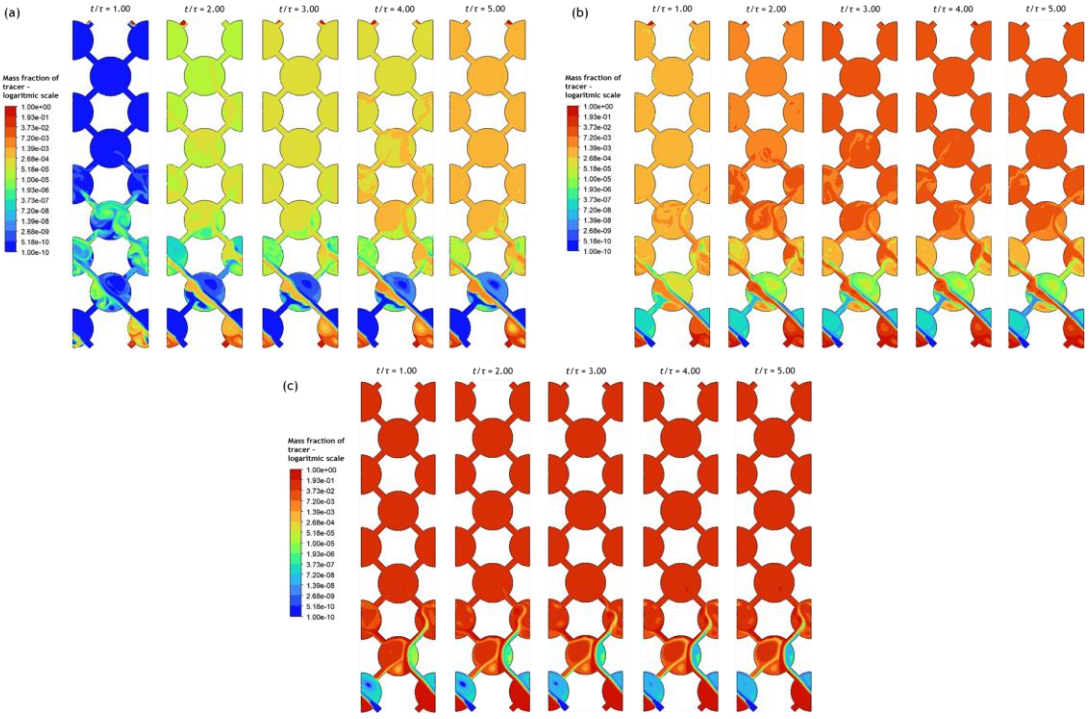

Figure 9. Tracer mass fraction contour maps for cases (a) 4 ($Re_l = 1200$ and $Re_r = 1.2$), (b) 5 ($Re_l = 1200$ and $Re_r = 12$) and (c) 6 ($Re_l = 1200$ and $Re_r = 120$).

3.5.3 Flow dynamics analysis

In order to better comprehend and describe the nature of the flow inside the NETmix reactor, power and frequency spectra were drawn and analysed for each case. Power spectra represent the variation of enstrophy, E, with a wavenumber, λ, calculated as $\lambda = f/\bar{u}_{in}$. The f variable represents the frequency

and $\bar{u}_{in}$ is the average fluid velocity at the inlets. Enstrophy is defined as the mean square vorticity and is normally used to characterise the intensity of vortices. The vorticity concept refers to the local rotation of fluid particles at a given point in the domain. Figure 10 shows a generic form of the power spectra normally obtained for small scale mixers with prismatic shapes, like the NETmix [63].

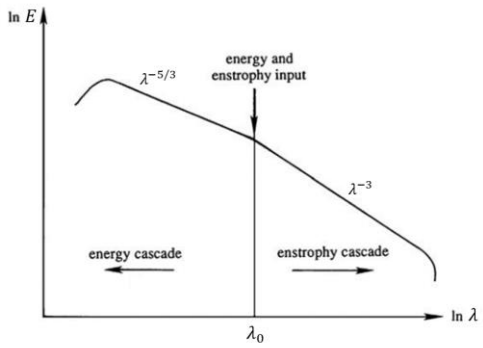

Figure 10. Typical power spectrum obtained for small scale mixers (adapted from [64]).

The flow inside these mixers is usually described by the 2D turbulence theory, which states that the energy contained in smaller scales is fed onto larger eddies until an inviscid state is achieved due to the conservation of enstrophy. In contrast, in 3D turbulence vortex stretching occurs, and so energy is transferred from larger eddies to smaller eddies until it is dissipated by viscosity. In cases with 3D turbulence, enstrophy is related to eddy scales, λ, by Kolmogorov's -5/3 power law, present in Equation 3.18 (ε is the kinetic energy cascade rate), and only a direct energy cascade is observable in the power spectrum [64].

$$E(\lambda) = const.\,\varepsilon^{2/3}\lambda^{-5/3} \tag{3.18}$$

In 2D turbulence, however, a dual cascade effect occurs, as it is shown in Figure 10. There are two cascades, namely the inverse energy cascade, in which $E \propto \varepsilon^{2/3}\lambda^{-5/3}$ and the transfer of energy goes to smaller wavenumbers (larger eddies), and the direct enstrophy cascade, in which $E \propto \alpha^{2/3}\lambda^{-3}$ and enstrophy is transferred to smaller scales until it is dissipated by viscous effects. α is the forward enstrophy flux. The point where the curve changes its slope indicates the energy injection scale [64].

Concerning frequency spectra, these represent the variation of the amplitude of the Discrete Fourier Transform (DFT) of the velocity fluctuations (Y_x and Y_y for $u_x = \bar{u}_x + u_x'$ and $u_y = \bar{u}_y + u_y'$, respectively, where u_x' and u_y' represent instantaneous velocity values) with the frequency. A Fourier Transform (Equation 3.19) converts a function of time, $x(t)$, into a function of frequency, $X(f)$, by decomposing a signal that is the combination of several signals with different frequencies in the time domain into functions that depend on the temporal frequency [65].

$$X(f) = \int_{-\infty}^{+\infty} x(t)e^{-2\pi i f t}dt \tag{3.19}$$

Figure 11 shows the power spectra obtained for all six cases from the velocity data at the centre of chamber C8. The x and y-axis are in logarithmic form. The vertical dashed lines indicate the inverse value of characteristic dimensions of the NETmix. L is called the laminar core and is calculated as: $L = D/2 - d$. Firstly, it is can be observed that, as expected, all power spectra present the dual cascade

tendency mentioned above for 2D turbulence. Regarding the energy injection scale, for Figures 11a, 11b and 11c, the change of slope from $E \propto \lambda^{-5/3}$ to $E \propto \lambda^{-3}$ occurs close to D^{-1}. In Figures 11d, 11e and 11f, this change occurs close to d^{-1}. The same energy injection scale identified for cases 4 to 6 was observed for 2D CFD simulations using the ExtendedNUB for equal Re at the two inlets between 300 and 2000 [66]. This means that a fully developed dynamic flow can be observed in the ExtendedNUB's eighth row in cases 4 to 6, where jets issuing from channels promote mixing by vortex engulfment in the chambers. The cases with $\mathrm{Re}_l = 600$, however, do not verify this behaviour. This could be due to the fact that the flowrates in the *r7* and *l7*-channels in these cases are not as uniform as the ones obtained in the cases with $\mathrm{Re}_l = 1200$. Hence, a fully developed dynamic flow is not achieved, resulting in an energy injection scale deviation from the standard NETmix behaviour. This suggests that higher Re at the water inlet should be preferred.

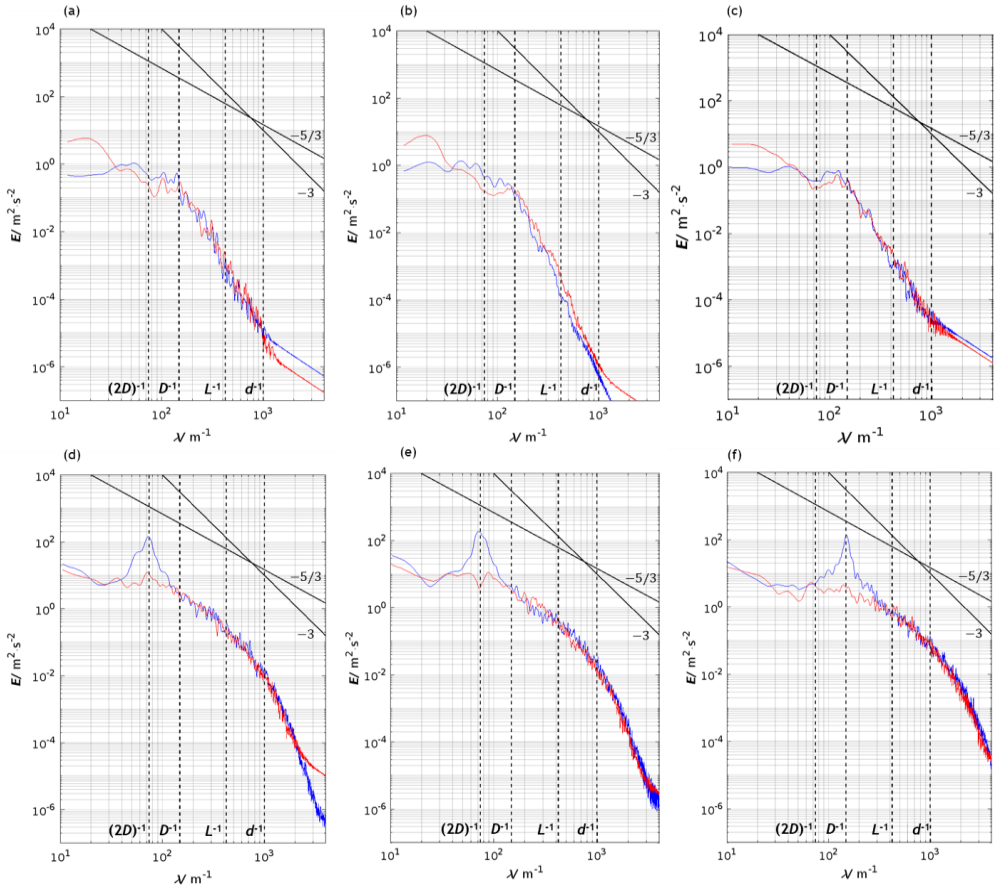

Figure 11. Power spectra for the x-velocity (blue) and y-velocity (red) components for cases (a) 1 ($Re_l = 600$ and $Re_r = 0.6$), (b) 2 ($Re_l = 600$ and $Re_r = 6$), (c) 3 ($Re_l = 600$ and $Re_r = 60$), (d) 4 ($Re_l = 1200$ and $Re_r = 1.2$), (e) 5 ($Re_l = 1200$ and $Re_r = 12$) and (f) 6 ($Re_l = 1200$ and $Re_r = 120$).

Furthermore, the blue curves shown in Figures 11d to 11f present clear energy peaks. These could indicate the presence of vortices in chamber C8 with a characteristic dimension equal to the inverse of the corresponding wavenumber. For cases 4 and 5, these vortices appear to have a dimension of $2D$. This means that two eddies are formed in chamber C8 that have the same behaviour due to the predominance of viscous forces, resulting in a spatial correlation of $2D$. For case 6, these vortices have a dimension of D, which is smaller than the other cases. This is a consequence of the increase of Re_r from 1.2 to 120,

that results in an increase of the flow dynamics and the formation of eddies with smaller dimensions. Finally, in all cases the energy curves obtained for the x and y-velocity components do not overlap, which means that the turbulence is anisotropic.

Figure 12 shows the frequency spectra obtained for the x-velocity fluctuations in all cases. It is notorious that the spectra obtained for the cases with higher Re_l are much more intense than the ones obtained for the cases with lower Re_l. The frequency spectra for the y-velocity fluctuations were also computed but were not taken into account since they were obtained for the direction parallel to the flow. They can be viewed in Appendix E.

Well defined isolated energy peaks can be observed in the frequency spectra obtained for cases 4 to 6 (Figure 12d to 12f). These energy peaks are a consequence of the presence of vortices with the characteristic dimensions mentioned above in chamber C8. Moreover, they indicate that fluid elements at the centre of this chamber oscillate in the x-direction more predominantly at a certain frequency over time. In addition, it is notorious that the frequency of these peaks increases as Re_r also increases. Higher Re values mean that the elements of fluid have higher kinetic energies and the flow dynamics is enhanced. Thus, vortex engulfment between the two halves of the NETmix chamber is also enhanced. In contrast, the frequency spectra for the cases with $\mathrm{Re}_l = 600$ (Figure 12a to 12c) do not have maximum energy peaks but rather a spread of energy around typical frequency values. This means that the vortices that are formed in chamber C8 do not have characteristic dimensions and are less energetic than the ones formed in cases 4 to 6. Therefore, the vortices oscillate less in the x-direction as a result of the lower inlet Reynolds numbers.

Vorticity contour maps were obtained for different normalised simulation times and for all cases. An analysis of these maps, presented in Appendix F, confirmed the conclusions drawn above.

Lastly, the intensity of turbulence in the x-direction, $I_{t,x}$, was determined at the centre of all the ExtendedNUB chambers for all cases (Figure 13). This parameter evaluates the deviation of the velocity that an element of fluid acquires at a specific time, $u_{x,i}$, from the time-averaged velocity, $\bar{u}_x$, and is calculated as it is shown in Equation 3.20 [67].

$$I_{t,x} = \frac{\sqrt{\sum_{i=1}^{N}\left(u_{x,i} - \bar{u}_x\right)^2 / N}}{\bar{u}_{in}} \tag{3.20}$$

By analysing Figure 13, it is clear that the intensities of turbulence obtained for the cases with $\mathrm{Re}_l = 600$ are considerably smaller than the ones obtained for the cases with $\mathrm{Re}_l = 1200$ from chamber C4 onwards. Moreover, in cases 2, 4 and 5, the $I_{t,x}$ values for chamber C2 are greater than the $I_{t,x}$ values for chamber C4. This is due to the flow direction that the jet coming from the *r1*-channel acquires when it reaches chamber C2. In these particular cases, the jet goes from channel *r1* to channel *l2* and so the x-velocity component computed at the centre of chamber C2 is considerably higher comparatively to the velocities obtained at this point in the cases where the jet goes from *r1* to *l1*. This then results in a higher turbulence and consequent higher $I_{t,x}$ values. Additionally, Figure 13a shows that the $I_{t,x}$ values along the ExtendedNUB chambers do not vary considerably and are only slightly higher for the case with $\mathrm{Re}_l = 600$ and $\mathrm{Re}_r = 60$ in chambers C6 and C8. This could be related to the less dynamic behaviour of the flow in

these cases and the more gradual flow uniformisation along the ExtendedNUB network. Although it appears that a stabilisation of the turbulence is in progress, simulations with a NUB model with more rows would be needed to confirm this assumption. In contrast, Figure 13b shows a sharp increase of $I_{t,x}$ along the chambers for all three cases due to the more predominant chaotic behaviour of the flow. Also, this indicates that the turbulence of the flow may not have stabilised yet at chamber C8. Once again, simulations in a NUB model with a higher number of rows would have to be performed to verify at which row begins the stabilisation of the turbulence when the water input has a Re of 1200.

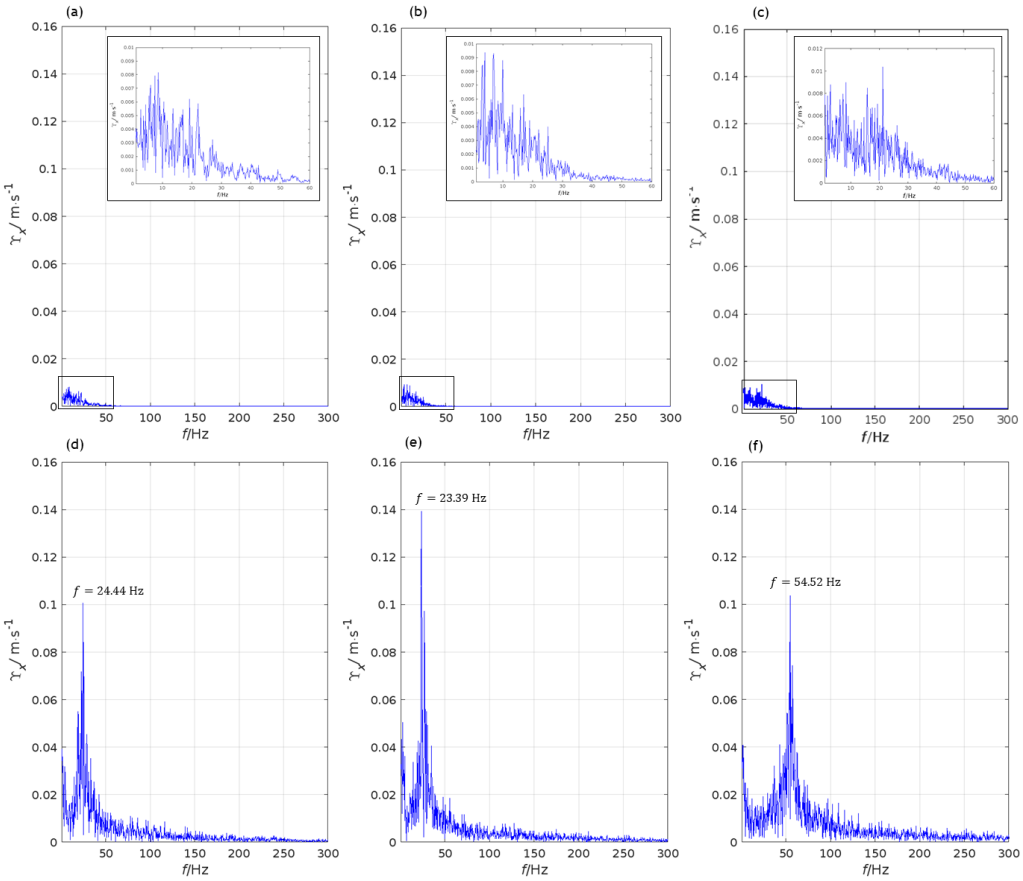

Figure 12. Frequency spectra for the x-velocity component for cases (a) 1 ($Re_l = 600$ and $Re_r = 0.6$), (b) 2 ($Re_l = 600$ and $Re_r = 6$), (c) 3 ($Re_l = 600$ and $Re_r = 60$), (d) 4 ($Re_l = 1200$ and $Re_r = 1.2$), (e) 5 ($Re_l = 1200$ and $Re_r = 12$) and (f) 6 ($Re_l = 1200$ and $Re_r = 120$).

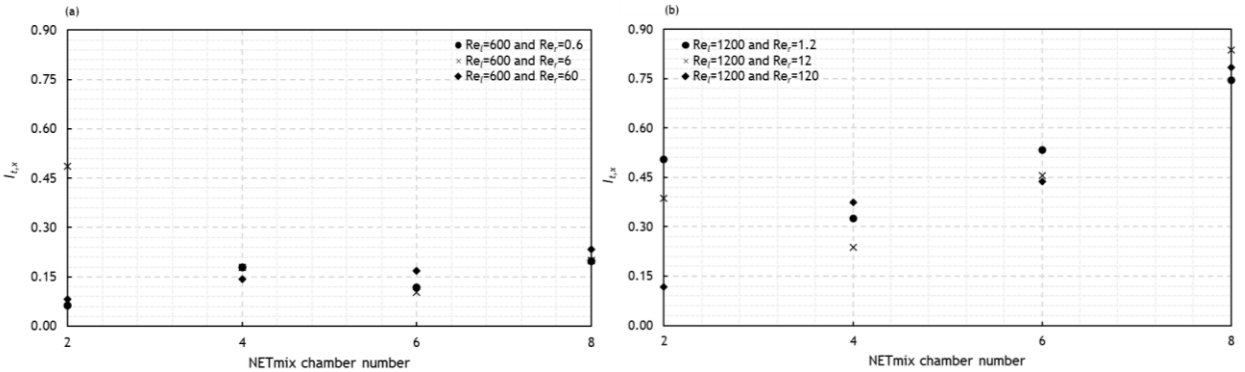

Figure 13. Variation of the intensity of turbulence in the x-direction with the chamber number for (a) cases with $Re_l = 600$ and (b) cases with $Re_l = 1200$.

4 Experimental work

4.1 Tracer experiments

After analysing the results obtained with the CFD simulations of the ExtendedNUB geometry for different asymmetric inlet flow conditions, it was necessary to experimentally validate them. It was only possible to study the mass transfer phenomenon for two Reynolds ratios, namely 10 and 100, due to mass flowmeter limitations. In this sense, tracer experiments were conducted.

4.1.1 Experimental setup

Figure 14 depicts a scheme of the experimental setup used in the laboratory. A photograph of the experimental setup can be seen in Appendix G.

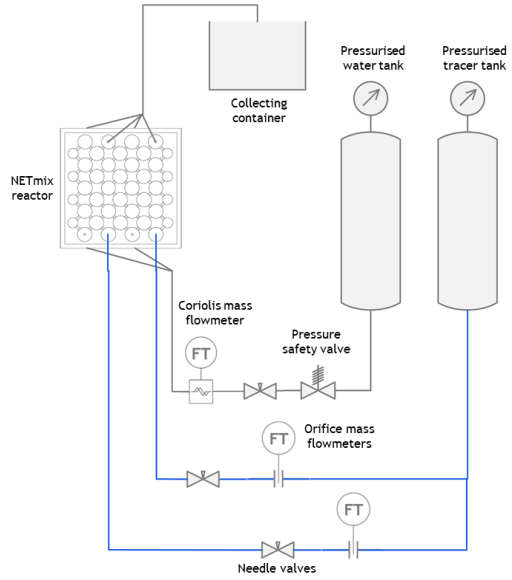

Figure 14. Experimental setup for the tracer experiments.

Both working fluids (water and tracer) were contained in pressurised tanks at a pressure of 3 barg. The tracer and water flowrates were controlled by needle valves placed downstream and upstream of the respective mass flowmeters. For the tracer flowrate measurement, two Alicat Scientific LC-200CCM-D Liquid Flow Meters were used. The flowrate reading was taken from these flowmeter's own display. For the water flowrate measurement, a Bronkhorst® Coriolis flowmeter, model mini CORI-FLOW™ M15, was used. The flowrate reading was done by connecting this flowmeter to a computer through a USB cable and using Bronkhorst's softwares FlowPlot and FlowDDE. Regarding the NETmix reactor, its dimensions were the same as the ones defined for the ExtendedNUB model, apart from the depth, which was 2 mm. Also, the inlet scheme was different in the sense that the fluid entered the NETmix reactor by radial inlets with a diameter of 1 mm placed at the centre of the first-row chambers. Pictures of the flow were captured with a Nikon D3400 + AF-P DX 18-55mm f/3.5-5.6G VR.

4.1.2 Materials and experimental conditions

Water was used as one of the working fluids. For the preparation of the tracer solution, indigo carmine, a blue pigment, was mixed with water. For both fluids, the working temperature was the ambient temperature (19.3 °C). Concerning the experimental conditions, these are summarised in Table 3. The Re_{3D} values were calculated as: $\mathrm{Re}_{3D} = \frac{\rho \bar{u}_{in} 2wd}{\mu(w+d)}$, and refer to the first channels of the NETmix reactor. It is important to mention that the water flowrate, q_{water}, values are four times the flowrate value in each channel connected to the two water chamber inlets. Each tracer flowrate, q_{tracer}, value are two times the flowrate in each channel connected to the tracer inlet chambers.

Table 3. Experimental conditions.

Simulated case	q_{water} / mL·min^{-1}	q_{tracer} / mL·min^{-1}		Required $\mathrm{Re}_{3D,water}$	Required $\mathrm{Re}_{3D,tracer}$	Real $\mathrm{Re}_{3D,water}$	Real $\mathrm{Re}_{3D,tracer}$	
2	221	0.9	1.2	600	6	610	5	7
3	214	10.7	12.7	600	60	592	59	70
5	429	2.0	2.4	1200	12	1185	11	13
6	431	21.9	22.9	1200	120	1192	121	127

4.1.3 Results and discussion

The results obtained for the experimental conditions shown in Table 3 are present in Figures 15a to 15d. The pictures taken of the NETmix reactor when operated with the different inlet conditions were compared to tracer mass fraction contour maps obtained during the simulations of cases 2, 3, 5 and 6 for a simulation time of $t/\tau = 5.00$. The colour scheme of the contour maps was changed to allow for an easier comparison and the respective scales are in logarithmic form. The dark blue frames present in all figures indicate the part of the NETmix reactor that corresponds to the ExtendedNUB geometry.

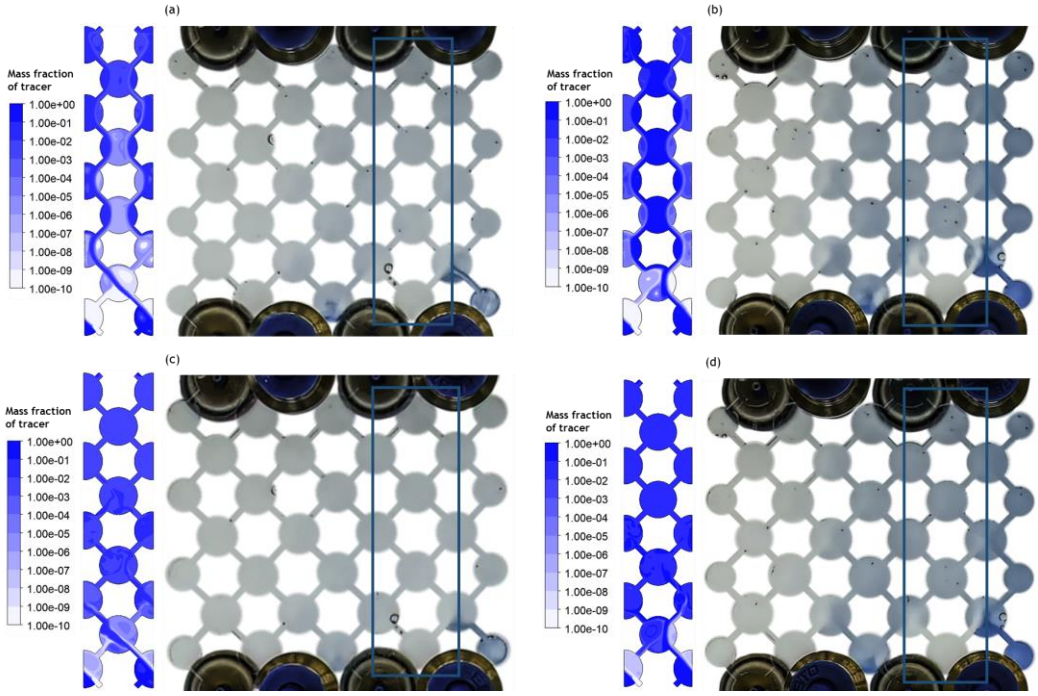

Figure 15. NETmix pictures and x_t contour maps for (a) case 2, (b) case 3, (c) case 5, and (d) case 6.

Firstly, by comparing Figures 15a and 15c with Figures 15b and 15d, it is notorious the dilution effect caused by $\mathrm{Re}_{3\mathrm{D},tracer}$ being 100 and 10 times smaller than $\mathrm{Re}_{3\mathrm{D},water}$, respectively. Hence, in the experiments reproducing cases 2 and 5, the tracer solution is diluted 100 times and, in the experiments reproducing cases 3 and 6, the dilution is of 10.

In addition, due to the low quality of the pictures present in Figure 15 as a consequence of poor lighting, it was not possible to compare the simulated flow patterns with the experiments. Nonetheless, it can be seen that the tracer concentration decreases along the framed areas, which indicates that mass transfer between water and tracer occurs in all cases. This is also seen in all x_t contour maps. Additionally, in Figures 15b and 15d, a similar flow pattern to the one observed in the right-hand side half-chambers of the respective contour maps can be seen on the left halves of the chambers of the 2nd column from the right-hand side of the NETmix reactor. It is also perceptible in all pictures that the intensity of the blue colour gradually decreases from the second to the fourth framed chamber, suggesting that the concentration of tracer becomes more homogeneous in the NETmix's downstream chambers and that efficient mixing of both phases occurs. This is desirable since it supports the use of the NETmix technology for the production of struvite from the liquid fraction of digestates.

However, the comparison of the CFD simulation results with the experimental data is limited. Firstly, the tracer (T) and water (W) injection scheme in the ExtendedNUB is different from the injection scheme of the NETmix reactor used for the tracer experiments. In the ExtendedNUB, the injection scheme is W-T-W-T, and, in the reactor at the channels, is W-W-T-T. Additionally, the inlet geometries are different. In the ExtendedNUB, both fluids enter the network through half-channels that lead to half-chambers. In contrast, in the NETmix reactor both fluids enter perpendicularly to the mixer through constrictions and then spread radially inside the respective inlet chambers. In addition, the 2D simulation results show planar tracer maps, which depict a sharper image of the flow structures. On the other hand, the images obtained from the tracer experiments show the flow inside a 3D structure, more precisely, the cloud of tracer that fills the NETmix chambers, and do not demonstrate the flow patterns so accurately.

At last, it can be seen in all pictures present in Figure 15 that the tracer concentration gradually decreases from the right-hand side column to the left-hand side column, the contours of which are almost not perceptible as it seems only water flows through it. This means that, although vertical mixing is achieved in all tracer experiments, the tracer concentration along the NETmix rows is not uniform and so outflows with different x_t are obtained. This suggests that the flow distribution at the inlets was not uniform due to the higher kinetic energy of the water streams that hindered the passage of the tracer streams.

Finally, tracer experiments in NETmix reactors with higher number of rows and columns should be done to assess if outlet flows with similar tracer concentrations can be obtained when operating the NETmix reactor with asymmetric inlet flow conditions.

4.2 Characterisation of a digestate liquid fraction

Since it was possible to prove that the NETmix reactor is capable of efficiently mixing two streams with different flow regimes, and thus validate its use for the production of struvite crystals, a characterisation of a liquid fraction of a digestate stream provided by Ave WWTP was done to study the influence of the composition of this stream on the struvite crystallisation process. The following physico-chemical parameters were analysed: pH, total suspended solids (TSS), volatile suspended solids (VSS), total solids (TS), chemical oxygen demand (COD), dissolved organic carbon (DOC), inorganic anions, ammoniacal nitrogen (NH_4-N), total phosphorus (TP) and total nitrogen (TN). Also, an Inductive Coupled Plasma (ICP) analysis was done to determine the metal content of this stream.

Results show the following molar concentrations for the species involved in the struvite precipitation reaction: $[\mathrm{NH_4^+}] = 0.17$ mol·L^{-1}, $[\mathrm{PO_4^{3-}}] = 1.86 \times 10^{-3}$ mol·L^{-1} and $[\mathrm{Mg^{2+}}] = 3.18 \times 10^{-4}$ mol·L^{-1}. The molar concentration of calcium was of 2.79×10^{-3} mol·L^{-1}. The molar ratios mentioned in section 2.3.1 were taken into account to determine whether it would be necessary to add a magnesium concentrated solution to the centrate stream to promote the formation of struvite crystals. It was found that the Mg:P ratio in the effluent was of 0.17 and the Ca:Mg ratio was of 8.77. Considering an ideal Mg:P of 1.6:1 [35] and an ideal Ca:Mg of 0.2:1 [37], it can be concluded that, in fact, it would be necessary to add magnesium to the digestate liquid fraction stream. This was expected since, as mentioned before, these effluents are known to have higher concentrations of N and P comparatively to Mg [25]. In this sense, the Mg concentration that the reaction medium should have to comply with each molar ratio was determined considering the concentrations of Ca^{2+} and PO_4^{3-} obtained during the characterisation of the effluent. For a Ca:Mg of 0.2:1, the reaction medium should have a Mg concentration of 0.014 mol·L^{-1}. This would imply, however, that the Mg:P ratio would be of 7.5, which is much higher than the optimum value. An excessive concentration of magnesium would increase the pH value above the desired level, leading to an increase of the saturation level of other kinds of magnesium phosphates and their precipitation, inhibiting the formation of struvite [23]. Regarding the optimum Mg:P ratio of 1.6, the reaction medium should have a Mg concentration of 2.98×10^{-3} mol·L^{-1} to obey this value. Nonetheless, this would result in a Ca:Mg of 0.9, which would significantly reduce the purity of struvite crystals and could even hinder their formation [38]. With this study, it was possible to conclude that a compromise should be done between the inhibition of the formation of calcium phosphates and of the precipitation of undesired magnesium phosphates, in order to be possible to obtain struvite crystals with a satisfactory purity level when performing their precipitation in the NETmix reactor.

Finally, the pH of the effluent was found to be of 7.70 at a temperature of 20.9 °C, which is below the optimum pH values for struvite precipitation mentioned in section 2.3.1. These ranged from 8.5 to 10.5. This confirms that the addition of an alkaline solution to regulate the pH of the reaction medium would be necessary while conducting a struvite precipitation reaction in the NETmix reactor, for instance, magnesium hydroxide.

5 Flow distributor CFD simulation

While doing the initial experimental studies to validate the CFD simulations of the tracer experiments, it was necessary to use Festo two-way Y-flow distributors (Figure 16) to divide the flows of tracer and water by the several inlets of the NETmix reactor. Upon starting the injection of both fluids, it was verified that the two flowrates exiting each outlet of the distributors were not identical, one being notoriously larger than the other. What is more, in the distributors used for the flows with the smallest Reynolds numbers the occurrence of backflow from the NETmix in one of the channels was verified. This could have been due to different pressure drops in each channel.

Figure 16. Festo two-way Y flow distributor.

Thus, in order to assess the influence of pressure on the flow inside this device, a Y-flow distributor was drawn in the ANSYS CAD tool Design Modeller and, after generating and validating the corresponding mesh, 2D simulations were conducted in the CFD package ANSYS/Fluent 2022 R2, in which different gauge pressures were imposed on each outlet and also different Reynolds numbers on the inlet. The following parameters were studied: the pressure at the inlet and the flowrates at each outlet.

5.1 Geometry and mesh

The geometry of the simulated Y-flow distributor is represented in Figure 17, with the respective dimensions. As it can be seen, the distributor has one inlet, with a diameter, d_{inlet}, of 2 mm, and two outlets with diameters $d_{outlet1}$ and $d_{outlet2}$ of 1 mm. In addition, the inlet channel has a length, h_1, of 6 mm and both outlet channels also have that same length, which is represented by h_2. The angle between both outlet channels, θ, is of 45º.

In relation to the mesh, it was necessary to perform a grid independence test in order to guarantee that the obtained solution did not vary with the decrease of the mesh element size. By decreasing this parameter, the number of mesh elements increases and so does the quality of the mesh to ensure the convergence of the results [68].

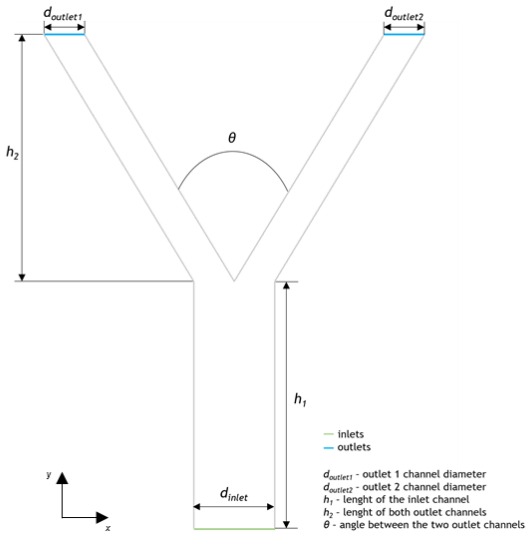

Figure 17. Identification of the surfaces and characteristic dimensions of the Y-flow distributor.

The selected mesh to perform the simulations had a mesh element size of 1×10^{-4} m, 2424 mixed cells and an average flow area of 2.4×10^{-5} m^2. Some simulations were conducted in turbulent regime, so, in those cases, inflation at the walls was imposed at a growth rate of 1.2 and with a maximum number of layers of 10. This was done to ensure that rapid changes of certain flow variables near the walls, such as pressure and velocity, would be accurately discretised [69]. Figure 18 exemplifies the effect of inflation in the mesh of the distributor.

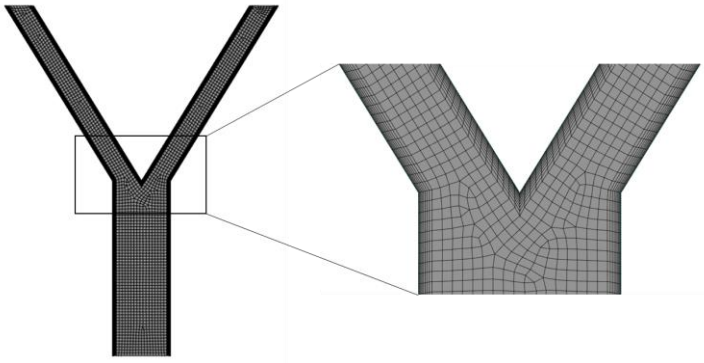

Figure 18. Mesh details of the inflation at the walls.

5.2 Governing equations

Regarding governing equations, the Navier-Stokes and continuity equations for momentum and mass conservation discussed in section 3.2 were solved for the simulations done in laminar regime. Once again, the energy conservation equations were not solved since an incompressible and isothermal flow was assumed.

In addition, depending on the Re number set at the inlet, simulations in turbulent regime were also performed. The standard k-ε model was chosen to simulate the turbulent flow due to its widespread validation for engineering applications, that has demonstrated reasonable accuracy and robustness of predictions. This model is a Reynolds-averaged Navier Stokes (RANS) turbulence model, which means

that the solution variables are decomposed into their time-averaged or ensemble-averaged mean and their fluctuating components, as it is shown in Equation 5.1 [56].

$$\varphi = \bar{\varphi} + \varphi' \tag{5.1}$$

In this Equation, φ is a generic representation of the solution variables, $\bar{\varphi}$ represents the mean and φ' represents the fluctuating components. In the case of fluid velocity, it can be decomposed in the following way: $u_i = \bar{u}_i + u_i'$. Thus, it is possible to adapt the continuity and momentum equations to the RANS turbulence models as it is shown in Equations 5.2 and 5.3, respectively [56].

$$\frac{\partial \rho}{\partial t} + \frac{\partial}{\partial x_i}(\rho u_i) = 0 \tag{5.2}$$

$$\frac{\partial}{\partial t}(\rho u_i) + \frac{\partial}{\partial x_j}(\rho u_i u_j) = -\frac{\partial p}{\partial x_i} + \frac{\partial}{\partial x_j}\left[\mu\left(\frac{\partial u_i}{\partial x_j} + \frac{\partial u_j}{\partial x_i} - \frac{2}{3}\delta_{ij}\frac{\partial u_l}{\partial x_l}\right)\right] + \frac{\partial}{\partial x_j}\left(-\rho\overline{u_i' u_j'}\right) \tag{5.3}$$

In these equations, the indexes i, j and l represent the three Cartesian coordinates and δ_{ij} is known as the Kronecker delta, that assumes the value of 1 if $i = j$ and of 0 if $i \neq j$. In addition, the second term on the right side of Equation 5.3 is called the Reynolds stresses. These are employed to represent the effects of turbulence and are modelled with the Boussinesq hypothesis, which is described in Equation 5.4. This hypothesis is based on the observation that the Reynolds stresses must be proportional to the mean rates of deformation [70].

$$-\rho\overline{u_i' u_j'} = \mu_t\left(\frac{\partial u_i}{\partial x_j} + \frac{\partial u_j}{\partial x_i}\right) - \frac{2}{3}\rho k \delta_{ij} \tag{5.4}$$

In Equation 5.4, μ_t is the turbulent viscosity and k is the turbulent kinetic energy per unit mass [70].

The k-ε model, in which ε is the dissipation rate, solves two additional transport equations for k and ε, present in Equations 5.5 and 5.6, respectively. It is important to mention that this model assumes that the flow is fully turbulent and the turbulence is homogeneous [56].

$$\frac{\partial}{\partial t}(\rho k) + \frac{\partial}{\partial x_i}(\rho k u_i) = \frac{\partial}{\partial x_j}\left[\left(\mu + \frac{\mu_t}{\sigma_k}\right) + \frac{\partial k}{\partial x_j}\right] + G_k + G_b - \rho\varepsilon - Y_M + S_k \tag{5.5}$$

$$\frac{\partial}{\partial t}(\rho \varepsilon) + \frac{\partial}{\partial x_i}(\rho \varepsilon u_i) = \frac{\partial}{\partial x_j}\left[\left(\mu + \frac{\mu_t}{\sigma_\varepsilon}\right) + \frac{\partial \varepsilon}{\partial x_j}\right] + C_{1\varepsilon}\frac{\varepsilon}{k}(G_k + C_{3\varepsilon}G_b) - C_{2\varepsilon}\rho\frac{\varepsilon^2}{k} + S_\varepsilon \tag{5.6}$$

In both equations, the term G_k is related to the generation of turbulent kinetic energy as a result of mean velocity gradients, G_b represents the generation of k due to buoyancy, that is, the generation of k due to the existence of a nonzero gravity field and a temperature gradient. In this case, $G_b = 0$. Furthermore, Y_M is related to the occurrence of fluctuating dilatation due to compressible turbulence. This parameter was set to zero since an incompressible flow was defined. $C_{1\varepsilon}$, $C_{2\varepsilon}$ and $C_{3\varepsilon}$ are model constants, σ_k and σ_ε are the turbulent Prandtl numbers for k and ε, and S_k and S_ε are user-defined source terms [56].

The turbulent viscosity present in these two equations can be calculated by Equation 5.7, in which the constant C_t is equal to 0.9 [56].

$$\mu_t = \rho C_t \frac{k^2}{\varepsilon} \tag{5.7}$$

5.3 Boundary and initial conditions

Boundary conditions were defined at the inlet, at both outlets and on the walls of the Y-flow distributor. Firstly, a parabolic inlet velocity profile was defined in each simulation in accordance to Equation 3.10. The average inlet velocity was calculated from the intended Reynolds number (Equation 3.8). In this case, however, the hydraulic diameter is equal to the inlet diameter ($d_h = d_{inlet}$), since the cross-sectional area of the inlet was considered circular. Table 4 summarises the different Reynolds numbers studied and the corresponding inlet velocities.

Table 4. Different Re studied and corresponding inlet velocities.

Cases	1	2	3	4	5	6
Re_{inlet}	100	200	300	400	500	600
Inlet velocity/m·s^{-1}	0.05	0.10	0.15	0.20	0.25	0.30

It should be mentioned that cases 1 to 3 were simulated in laminar regime and cases 4 to 6 were simulated in turbulent regime. Although there appears to be no information regarding flow regimes in this type of distributor, the Reynolds number intervals for flow regimes around an obstacle were considered to justify the choices mentioned before. For Re higher than 300, the flow in these situations is classified as turbulent [71]. Moreover, a study conducted by Liu et al. reported a turbulent flow behaviour in a flow distributor for Reynolds numbers varying from 300 to 1539 [72].

In addition, water was chosen as the working fluid (ρ = 998.2 kg·m^{-3} and μ = 1.003 mPa·s) and a no-slip condition was defined at the walls of the distributor. Regarding the outlets, different gauge pressures were defined in each one of them so as to study their influence on the flow. Table 5 shows the pressures imposed in each outlet and the pressure difference between them ($\Delta p_{outlet} = p_{out,1} - p_{out,2}$). The pressure value of 3000 Pa was estimated to be the head loss from the outlet of the distributors to the collecting container used in the experimental setup. It should also be noted that only the gauge pressure in outlet 1 was varied and all the cases described in Table 5 were studied for each Reynolds number present in Table 4. Finally, all simulations were done in steady state and a hybrid solution initialisation method was adopted.

Table 5. Cases studied with different Δp_{outlet}.

Cases	a	b	c	d	e	f	g	h	i	j
$p_{out,1}$/Pa	3000	3001	3010	3050	3070	3100	3300	3600	3900	4200
$p_{out,2}$/Pa	3000	3000	3000	3000	3000	3000	3000	3000	3000	3000
Δp_{outlet}/Pa	0	1	10	50	70	100	300	600	900	1200

5.4 Models and solution methods

A pressure-based type solver was chosen for all simulations and the viscous laminar and the standard k-ε models were chosen in accordance to the inlet Reynolds number. Regarding the solution methods, for the pressure-velocity coupling the Coupled method was chosen. The Least Squares Cell Based method was used for gradient discretisation, the Second Order method for pressure discretisation and the Second Order Upwind for momentum discretisation. Also, the chosen Pseudo Time method was the Global Time Step. In the cases simulated in turbulent regime, it was necessary to define the discretisation methods for k and ε. For both the First Order Upwind method was employed. Finally, the converge criteria defined for all simulations were residuals lower than 1×10^{-5}.

5.5 Results and discussion

5.5.1 Mesh independence test

A mesh independence test was done in order to determine the smallest mesh element size that would lead to obtaining results with no significant variation in relation to the previous element size [69]. The variation of two variables with the decrease of the mesh element size was studied, namely the pressure difference in the distributor, computed as $\Delta p_{distributor} = p_{inlet} - p_{outlet}$, and the shear stresses at the walls, τ. Table 6 shows the different element sizes studied and the respective number of element cells. For all cases, the inlet Re was of 100 and a gauge pressure of 3000 Pa was defined in each outlet.

Table 6. Mesh element sizes and respective number of mesh element cells.

Mesh element size (Δx)/m	5.0×10^{-4}	2.0×10^{-4}	1.5×10^{-4}	1.0×10^{-4}	7.0×10^{-5}	5.0×10^{-5}
Number of element cells	106	618	1093	2424	4936	9627

Figures 19a and 19b show the variation of $\Delta p_{distributor}$ and τ with the number of mesh elements, respectively.

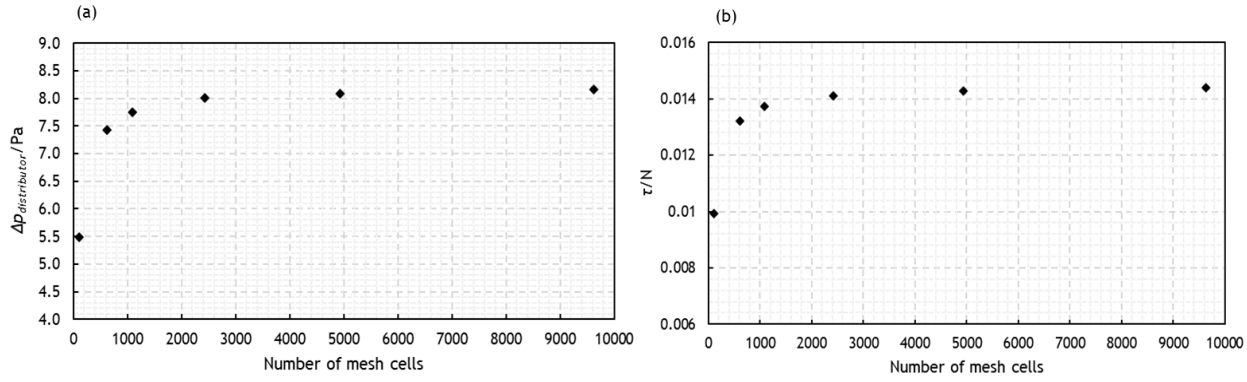

Figure 19. Variation of (a) $\Delta p_{distributor}$ and (b) τ with the number of mesh element cells.

By analysing Figure 19, one can see that both variables increase with the increase of the number of mesh cells (or, in other words, with the decrease of Δx) until they start to stabilise from $\Delta x = 1.0 \times 10^{-4}$ m. Furthermore, relative errors for both variables, $E_{r,\Delta p_{distributor}}$ and $E_{r,\tau}$, were calculated in relation to the

smallest Δx (5.0×10^{-5} m) so as to assess the deviation of the results obtained for denser meshes. Errors lower than 5 % accompanied by a sharp increase of the number of element cells were considered negligible and so meshes with errors smaller than this percentage would be deemed sufficiently refined. Equations 5.9 and 5.10 show how these errors were determined.

$$E_{r,\Delta p_{distributor}}(\%) = \frac{\left|\Delta p_{distributor,\ x\Delta x \neq 5\times10^{-5}} - \Delta p_{distributor,\Delta x=5\times10^{-5}}\right|}{\Delta p_{distributor,\Delta x=5\times10^{-5}}} \times 100 \quad (5.9)$$

$$E_{r,\tau}(\%) = \frac{\left|\tau_{\Delta x \neq 5\times10^{-5}} - \tau_{\Delta x=5\times10^{-5}}\right|}{\tau_{\Delta x=5\times10^{-5}}} \times 100 \quad (5.10)$$

Table 7 summarises the relative errors obtained for each mesh element size and each variable.

Table 7. Mesh element sizes, variation of the number of element cells and respective relative errors.

Mesh element size/m	5.0×10^{-4}	2.0×10^{-4}	1.5×10^{-4}	1.0×10^{-4}	7.0×10^{-5}
Variation of the number of element cells/%	-----	483	77	122	104
$E_{r,\Delta p_{distributor}}$/%	32.88	9.00	5.05	2.00	0.98
$E_{r,\tau}$/%	30.93	8.11	4.63	1.92	0.70

Table 7 shows a decrease of the relative errors as the refinement of the mesh increases, as expected. Analysing the errors obtained for each Δx, it was concluded that a mesh with a Δx of 1×10^{-4} m would be sufficiently refined, since the obtained errors were both inferior to 5 % (2.00 and 1.92 %) and the increase of the number of element cells in relation to the previous mesh was of 122 %. Thus, the simulations were all performed with this mesh.

5.5.2 Pressure influence analysis

In order to study the influence of different pressure outlets on the flow in the Y-distributor, the flowrates in each outlet, $q_{out,1}$ and $q_{out,2}$, were obtained. In addition, the inlet pressure values, p_{inlet}, were also determined. This procedure was repeated for the different Re_{inlet} present in Table 4. Figures 20a and 20b show the variation of $q_{out,1}$ and $q_{out,2}$ with Δp_{outlet} for different inlet Reynolds numbers. The x-axis in both graphs is in logarithmic form. It should be noted that negative flowrate values indicate that the flow is exiting the distributor and positive values mean that the flow is entering this device, i.e., backflow.

By observing Figure 20a, it is noticeable that initially, for all Re_{inlet}, the $q_{out,1}$ values do not vary significantly with the increase of the outlet pressure difference until a Δp_{outlet} of 50 Pa. Then, they start to decrease and eventually become positive. This indicates that, after a certain Δp_{outlet}, the flow direction reverses and water starts to enter the distributor through outlet 1 as a consequence of the higher pressure on its left side. For Re_{inlet} values of 100 and 200, this transition in the flow behaviour occurs at $\Delta p_{outlet} = 70$ Pa, for $\mathrm{Re}_{inlet} = 300$ and 400 occurs at $\Delta p_{outlet} = 300$ Pa and for Re_{inlet} of 500 and 600 it happens when $\Delta p_{outlet} = 600$ Pa.

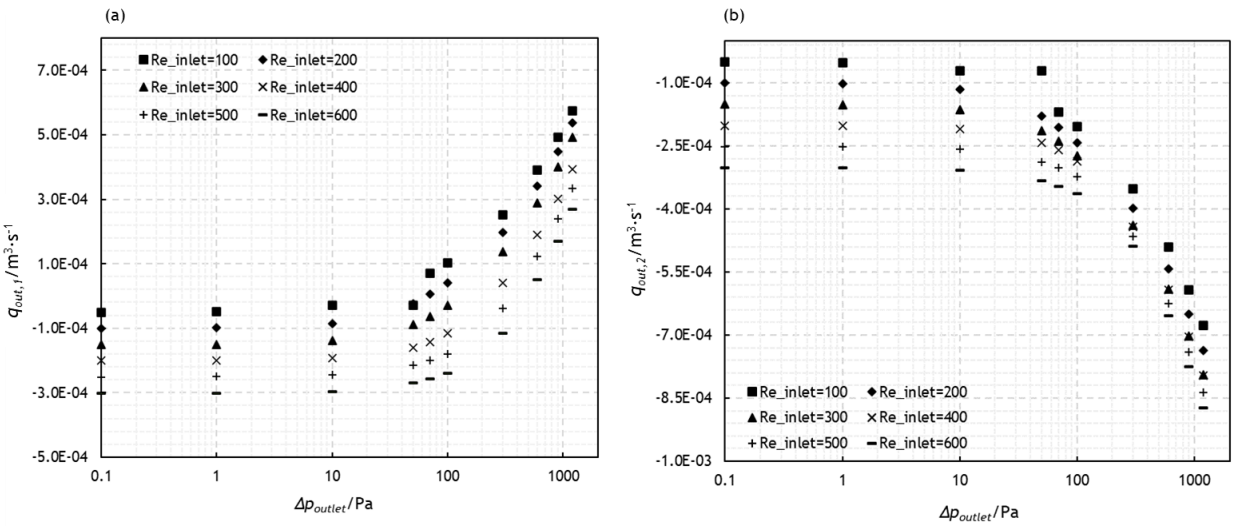

Figure 20. Variation of (a) $q_{out,1}$ and (b) $q_{out,2}$ with Δp_{outlet} for different Re_{inlet}.

This can be justified by the fact that the pressure drop varies proportionally with the velocity, which means that a higher velocity at the inlet of the distributor increases the $\Delta p_{distributor}$. In addition, the pressure felt at the beginning of each outlet channel, that is, where the bifurcation occurs, $p_{bifurcation}$, is the same. The pressure drop felt on the left-hand side outlet channel is $\Delta p_{out,1} = p_{bifurcation} - p_{out,1}$, and the pressure drop in the right-hand side outlet channel is given by $\Delta p_{out,2} = p_{bifurcation} - p_{out,2}$, and so it can be said that $\Delta p_{out,1} + p_{out,1} = \Delta p_{out,2} + p_{out,2}$. In this sense, the increase of Re results in an increment of $p_{bifurcation}$ and, consequently, of $\Delta p_{out,1}$ and $\Delta p_{out,2}$, meaning that as the inlet Reynolds number is increased the Δp_{outlet} at which backflow starts to occur also increases. Note that, for backflow to occur, $p_{out,1}$ must be higher than $p_{bifurcation}$ and, since the increase of the inlet Reynolds results in an increase of $p_{bifurcation}$, $p_{out,1}$ must also increment. Consequently, the pressure difference between both outlets also increases.

Furthermore, Figure 20b shows that the $q_{out,2}$ are always negative, which means that the backflow effect never occurs in this side of the distributor. This is expected since the flow goes preferentially to the side with the lower pressure drop. In addition, as Δp_{outlet} is increased, the absolute values of $q_{out,2}$ also increase, as it can be seen in Figure 20b, due to the principle of mass conservation.

The variation of the inlet pressure with Δp_{outlet} was also represented, as it can be seen in Figure 21. Once again, the x-axis is in logarithmic scale. Firstly, it can be observed that the increase of Re_{inlet} results in an increment of the inlet pressure, for the same Δp_{outlet}. This could be due to the fact that higher kinetic energy results in higher pressure drops and, therefore, a higher pressure is needed at the inlet. Since the pressure outlet conditions are the same, the inlet pressure must increase to compensate the higher pressure drops. Additionally, all plots present the same tendency, which is approximately constant p_{inlet} values until a Δp_{outlet} of 50 Pa and then a gradual increase of the inlet pressure as the outlet pressure difference also increases. This is a direct consequence of the increase of $p_{out,1}$ while maintaining $p_{out,2}$ constant. For the same Re_{inlet}, the increase of $p_{out,1}$ must be compensated by an increase of p_{inlet} so that the pressure drop felt in the distributor remains the same.

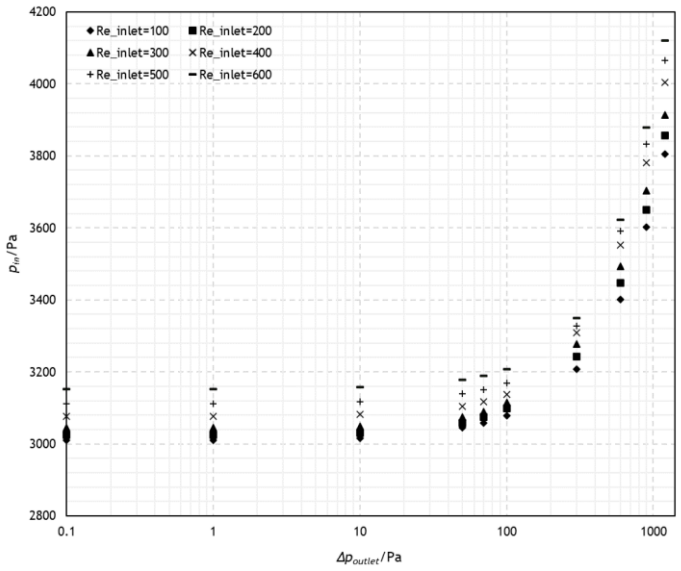

Figure 21. Variation of p_{inlet} with Δp_{outlet} for various Re_{inlet}.

This study made it possible to conclude that a pressure difference of 50 Pa, which represents 5 mm of water column, although considerably small, is sufficient to make the flow distribution between the two outlets of the distributor non-uniform. This is not desirable since it affects the flow distribution at the inlets of the NETmix reactor and consequently its performance. These pressure differences between outlets can be related to manufacture malfunctions during the production of these Y-flow distributors. Other factors that may influence negatively the flow distribution at the inlets of the reactor are very small alignment issues of the reactor, or an inlet pressure profile in the NETmix, which will be assessed in the next section.

6 NETmix Entire Block CFD simulation

In order to deepen the study of the pressure influence on the experimental facility shown in chapter 4, the whole network of the NETmix reactor used in the laboratory was designed.

The objective of this study was to assess the influence of the pressure at the first channels of the NETmix reactor on the flow distribution at the inlets as well as the effect of the smaller side chambers on the pressure and, consequently, on the flow distribution. Once again, simulations were conducted on the commercial package ANSYS/Fluent 2022 R2. The velocity and pressure profiles were taken for these channels and the pressure difference between the channels that are connected to the same radial inlet chamber were determined for different asymmetric inlet flow conditions.

6.1 Geometry and mesh

The geometry domain of the entire network of the NETmix, called the NETmix Entire Block (NEB) model, is depicted in Figure 22. The characteristic dimensions and the identification of surfaces can also be seen in this figure.

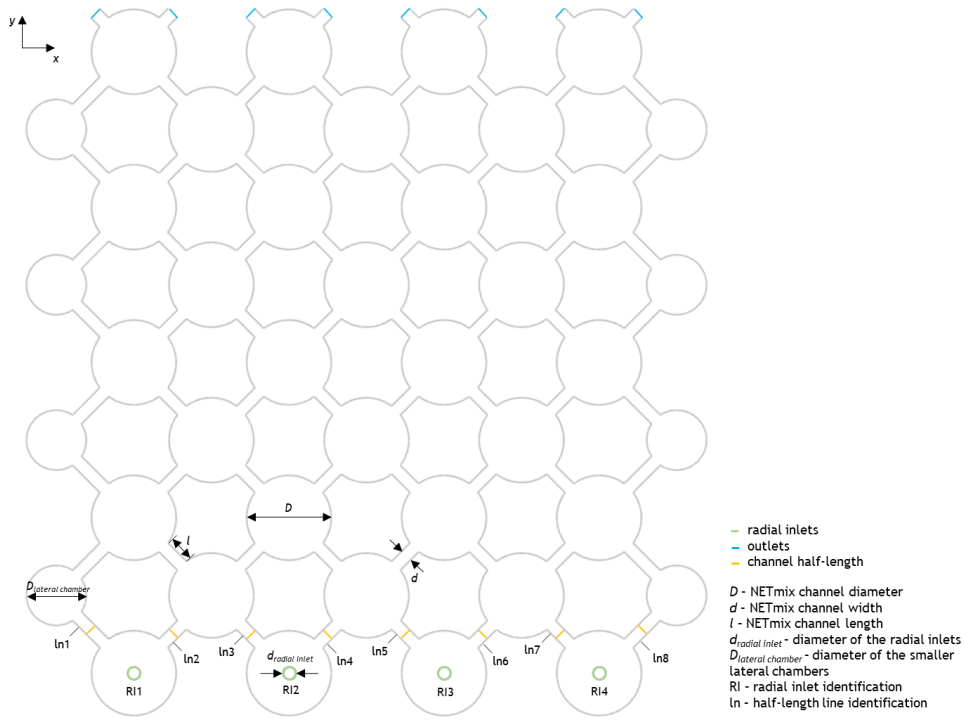

Figure 22. NEB geometry domain and characteristic dimensions and surfaces identification.

The dimensions shown in Figure 22 have the following numerical values: $D = 6.75$ mm, $d = 1.0$ mm, $l = 2$ mm, $d_{radial\ inlet} = 1$ mm and $D_{lateral\ chamber} = 4.77$ mm.

Additionally, the mesh independence test was not performed since it was already validated for other NETmix geometries in previous works. The mesh element size is of 62.5 μm, the number of element cells is of 3.9×10^5 and the mesh has an average surface area of 1.44×10^{-3} mm^2.

6.2 Governing equations, boundary and initial conditions

The simulations performed with the NEB model were conducted in laminar regime, so the Navier-Stokes and continuity equations for momentum and mass conservation discussed in section 3.2 were solved. Moreover, the energy conservation equations were not solved since an incompressible and isothermal flow was assumed.

Concerning boundary conditions, asymmetric velocity magnitudes were imposed in alternated radial inlets. The velocity magnitude set at each radial inlet, $\bar{u}_{in,RI}$, was determined considering that the mass flowrates, $\dot{m}$, in the channels connected to the corresponding inlet chamber would be equal, as it is illustrated in Equation 6.1 (mass conservation principle). The calculation of the velocity magnitude is also deduced in this equation.

$$\dot{m}_{R1} = \dot{m}_{ln1} + \dot{m}_{ln2} \Leftrightarrow \rho \bar{u}_{in,RI1} w \pi d_{radial\ inlet} = \rho \bar{u}_{channel}(d+d)w \Leftrightarrow \bar{u}_{in,RI1} = \frac{2d\bar{u}_{channel}}{\pi d_{radial\ inlet}} \qquad (6.1)$$

Equation 6.1 is a calculation example for the determination of the inlet velocity magnitude in RI1. The same procedure was done for the remaining inlets (RI2 to RI4). Also, $\bar{u}_{channel}$ corresponds to the desired velocity in each pair of channels (in this case, channels ln1 and ln2) and w is the width of the NETmix reactor. The determination of $\bar{u}_{channel}$ was made based on Equation 3.8, used for the calculation of the Reynolds number. As in the ExtendedNUB model, the hydraulic diameter is equal to $2d$. Table 8 summarises the different combinations of asymmetric Reynolds numbers studied and the respective inlet velocities. A reference case study, with all inlet Re equal to 100, was also simulated.

Table 8. Cases studied with asymmetric inlet conditions in the NEB model.

Lines	Case 1		Case 2		Case 3	
	Re	$\bar{u}_{in,RI}$ / m·s^{-1}	Re	$\bar{u}_{in,RI}$ / m·s^{-1}	Re	$\bar{u}_{in,RI}$ / m·s^{-1}
ln1	0.1	3.2×10^{-5}	1	3.2×10^{-4}	10	3.2×10^{-3}
ln2	0.1		1		10	
ln3	100	3.2×10^{-2}	100	3.2×10^{-2}	100	3.2×10^{-2}
ln4	100		100		100	
ln5	0.1	3.2×10^{-5}	1	3.2×10^{-4}	10	3.2×10^{-3}
ln6	0.1		1		10	
ln7	100	3.2×10^{-2}	100	3.2×10^{-2}	100	3.2×10^{-2}
ln8	100		100		100	

Furthermore, water was chosen as the working fluid (ρ = 998.2 kg·m^{-3} and μ = 1.003 mPa·s) and a no-slip condition was defined at the walls of the distributor. Regarding the outlets, gauge pressures of 0 Pa were defined in each one of them.

Finally, the simulations were done in steady state, since the imposed Re values were all below Re_c, so the flow was always in laminar regime, and the same Reynolds number ratios studied in chapter 3 (10, 100 and 1000) were used, as it can be seen in Table 8. A hybrid initialisation was set.

6.3 Models and solution methods

A pressure-based type solver and the viscous laminar model were chosen for all simulations. Regarding the solution methods, for the pressure-velocity coupling the Coupled method was chosen. The Least Squares Cell Based method was used for gradient discretisation, the Second Order method for pressure discretisation and the Second Order Upwind for momentum discretisation. Moreover, the chosen Pseudo Time method was the Global Time Step. Finally, the converge criteria defined for all simulations were residuals lower than 1×10^{-8}.

6.4 Results and discussion

The total pressure profiles in each line as well as the velocity magnitude profiles were computed for each case. Figures 23a and 23b show the variation of the average total pressure, p, with the NEB line number and the variation of the pressure difference between the two channels of each inlet, $\Delta p_{channels}$, with the radial inlet number, respectively. The total pressure is calculated as the sum of the static and dynamic pressures [56].

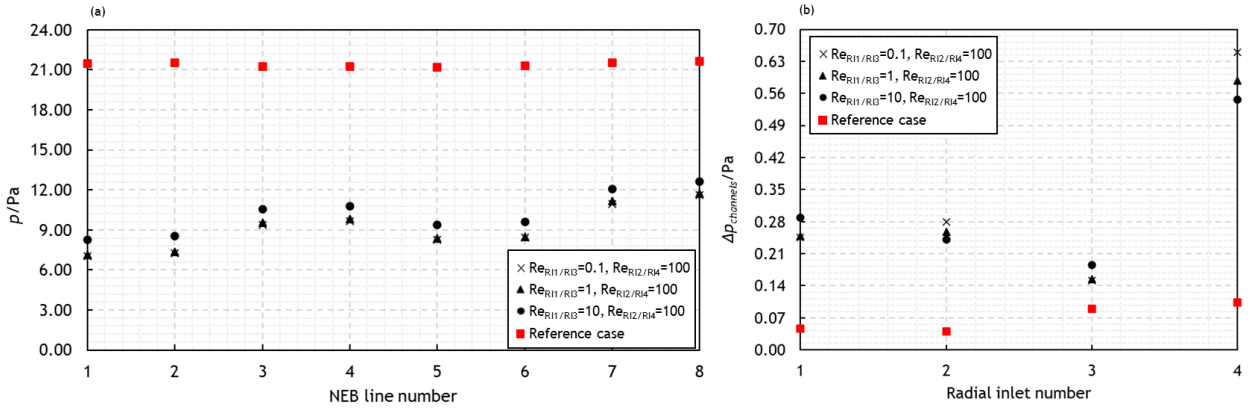

Figure 23. Variation of (a) the average total pressure with the NEB line number and (b) of $\Delta p_{channels}$ with the radial inlet number.

Figure 23a shows that the pressure values of the channels with odd line numbers are always lower than the pressure values of the even-numbered channels for cases 1 to 3, which indicates that the flow distribution in each radial inlet is not entirely uniform. Additionally, the pressure values obtained for the channels with smaller Re are always lower than the pressure values obtained for the channels with higher Re. This can be explained by Newton's viscosity law, in which shear stresses are directly proportional to velocity gradients, i.e., $\tau_{yx} = \mu \frac{du_x}{dy}$ [73]. Higher Re values mean larger velocity gradients, which result in an increase of the shear stresses at the walls and of the pressure at the inlet chambers with higher Re. In order to better comprehend the behaviour of the flow at the inlets, pressure and velocity magnitude contour maps were drawn for each case and are present in Appendix I. Additionally, velocity streamlines were drawn for the first two rows of the NEB geometry and can also be seen in Appendix I.

By analysing Figure 34 of Appendix I, one can clearly see the larger pressure values at the inlet chambers associated with higher inlet velocities. It is also notorious that as $\mathrm{Re}_{\mathrm{RI1/RI3}}$ increases, the pressure within the same inlet chamber also increases. This is evidenced by the intensification of the colour that fills

these chambers. The velocity magnitude contours maps for cases 1 to 3 (Figure 35) show colour gradients in all inlet chambers, which, as expected, are more pronounced in the inlet chambers with higher Re. Also, the colour patterns in these chambers suggest an uneven radial flow distribution from the centre to the chamber walls. The velocity streamlines, present in Figures 37 to 39 of Appendix I, allow to better visualise the flow pattern distribution inside these chambers. For the inlet chambers RI2 and RI4 in cases 1 to 3, two large recirculation zones can be seen in each halve. These recirculation zones are formed due to the change of geometry and direction that the flow entering the chambers suffers and could be responsible for the abovementioned greater pressure values. As in chambers RI2 and RI4 the fluid velocity is larger, the recirculation zones are more intense and so the pressure is greater than in chambers RI1 and RI3.

Figure 23a shows that the pressure values for each channel for the reference case are almost constant, which indicates that the flow distribution in the inlet chambers is more homogenous comparatively to the cases with asymmetric inlet conditions. This can also be seen in Figures 33 and 36 of Appendix I.

Moreover, comparing the $\Delta p_{channels}$ values for inlet chambers RI1 and RI3 and for inlet chambers RI2 and RI4, it is notorious that the values for the chambers connected to the side chambers (RI1 and RI4) are higher than the values for the chambers not connected to them. Table 9 shows these $\Delta p_{channels}$ values.

Table 9. $\Delta p_{channels}$ values for each inlet radial chamber for all cases studied.

	$\Delta p_{channels}$ / Pa			
Cases	Chamber RI1	Chamber RI2	Chamber RI3	Chamber RI4
Reference	0.05	0.04	0.09	0.10
1	0.25	0.28	0.15	0.65
2	0.25	0.26	0.15	0.59
3	0.29	0.24	0.19	0.55

Analysing the values present in Table 9, it is possible to conclude that, in fact, there is a significant difference between the $\Delta p_{channels}$ values for RI1 and RI3 and for RI2 and RI4 as a result of the influence of the side chambers on the flow distribution. Comparing cases 1, 2 and 3, the $\Delta p_{channels}$ for the same inlet chamber are not very dissimilar. Regarding the reference case, the pressure differences are considerably lower than the ones obtained for cases 1 to 3, which is due to the equal flow conditions set at the inlets. Nevertheless, the $\Delta p_{channels}$ for the two right-hand side inlet chambers are higher than the $\Delta p_{channels}$ for the left-hand side inlet chambers.

These studies allowed to conclude that when dissimilar inlet flow conditions are set in the NEB geometry, there is not a uniform pressure distribution along the first row, which leads to an uneven flow distribution. Nevertheless, as it can be seen in the contour maps for cases 1 to 3 in Appendix I, the pressure and velocity magnitude along the rows end up uniformising in downstream chambers, attesting to the well-known mixing abilities of the NETmix reactor. However, this uneven initial flow distribution in the first rows of the NETmix coupled with an asymmetric flow distribution in the Y distributors that divide the tracer and water flows by the inlets could negatively affect the extent of the reaction along the reactor due to a non-uniform phase contact time.

7 Conclusions

The main objective of this dissertation was to propose the use of the NETmix technology to recover phosphorus and nitrogen from the liquid fraction of side-stream digestates in the form of struvite. With this purpose in mind, CFD simulations of tracer experiments were carried out with the 2D ExtendedNUB geometry to assess the mixing capacities of this static mixer when operated with two different inlet flow conditions, specifically one that would onset a fully developed laminar regime in the reactor and another that would lead to a self-sustained fully chaotic and oscillatory flow regime. Analysis of the flow distribution, mass transfer between water and tracer, and flow dynamics were conducted for the following case studies: $\mathrm{Re}_l = 600$ and $\mathrm{Re}_r = 0.6$, $\mathrm{Re}_l = 600$ and $\mathrm{Re}_r = 6$, $\mathrm{Re}_l = 600$ and $\mathrm{Re}_r = 60$, $\mathrm{Re}_l = 1200$ and $\mathrm{Re}_r = 1.2$, $\mathrm{Re}_l = 1200$ and $\mathrm{Re}_r = 12$, and $\mathrm{Re}_l = 1200$ and $\mathrm{Re}_r = 120$.

First of all, the flow distribution analysis showed that, in all cases, flowrate values in opposite channels tend to approximate along the ExtendedNUB and are almost identical in the outlet channels. This proved that the NETmix reactor is able to equally distribute the flow along its network when dissimilar flow conditions are set at the inlets. However, the differences between outlet flowrates obtained for the cases with $\mathrm{Re}_l = 1200$ were smaller comparatively to the differences obtained for the cases with $\mathrm{Re}_l = 600$. This could be explained by the fact that higher Reynolds numbers at the inlets enhance the dynamic behaviour of the flow and promote a higher mixing degree in the ExtendedNUB chambers, resulting in a more homogenous flow distribution. Velocity magnitude contour maps demonstrated that the formation of vortices in downstream chambers was responsible for the flow distribution phenomenon.

Regarding mass transfer, it was observed that increasing Re_l resulted in a decrease of the intensity of segregation values for the same channel number. Moreover, the increment of Re_r had the same effect on the I_s values. Higher Re values mean that the fluid has a higher kinetic energy and so the flow dynamics increases, leading to the formation of more eddies and an enhancement of the mixing degree in the reactor with a consequent decrease of I_s. Mass fraction of tracer contour maps confirmed the previous statement. Uniform tracer concentrations could be observed in downstream chambers of the ExtendedNUB for the cases with $\mathrm{Re}_l = 1200$, while concentration gradients were present in those same chambers for the cases with $\mathrm{Re}_l = 600$, proving that mass transfer between fluids in these last cases was not as efficient.

The power spectra for chamber C8 obtained for the flow dynamics analysis showed that the energy injection scale for the cases with $\mathrm{Re}_l = 1200$ coincided with a wavenumber of d^{-1}, which was in agreement with results obtained for CFD simulations of the NETmix reactor with an equal Re in both inlets varying from 300 to 2000 [66]. This evidenced that a fully developed dynamic flow was achieved in these cases. In contrast, the energy injection scale for the cases with $\mathrm{Re}_l = 600$ coincided with D^{-1} and deviated from the standard NETmix behaviour. This could have been due to the fact that the flowrates in downstream channels in these cases were not as uniform. Additionally, the power spectra for the cases with $\mathrm{Re}_l = 1200$ demonstrated the existence of vortices with characteristic NETmix dimensions in chamber C8 oscillating in the x-direction. Finally, the frequency spectra for the cases with lower Re_l did not have isolated energy peaks as the ones present in the frequency spectra of the cases

with higher Re_l, meaning that the vortices formed in chamber C8 were not as energetic as the ones formed in the cases with $\mathrm{Re}_l = 1200$.

Experimental validation of the simulated tracer experiments was conducted in a NETmix reactor with the same characteristic dimensions as the 2D ExtendedNUB, apart from the depth, for the cases with $\mathrm{Re}_l/\mathrm{Re}_r$ = 10 and 100. It was possible to conclude that mixing between the water and tracer streams occurred in the chambers of the section of the NETmix reactor equivalent to the ExtendedNUB geometry in all cases. Gradual dissipation of the blue colour of the flow along the chambers proved this remark. Nonetheless, outlet streams with different tracer concentrations were obtained, which indicated that the mixing degree along the rows of the reactor was not uniform. In this sense, conducting tracer experiments in a NETmix reactor with more rows operated with asymmetric inlet flow conditions was suggested in order to check whether it is possible to obtain outlet streams with similar compositions.

In addition, the objective of conducting the simulations with the Y-flow distributor geometry was to evaluate the influence of different outlet pressures in the flow inside this device for different Reynolds. It was possible to conclude that Δp_{outlet} values superior to 50 Pa significantly decrease the flowrate in the channel with higher outlet pressure until backflow starts to occur. The Δp_{outlet} value at which this transition occurs depends on the Reynolds number of the flow. Greater Re values result in a redirection of the flow at higher Δp_{outlet} due to a higher kinetic energy of the flow. This study showed that small pressure differences in the outlets of these devices, which were used to divide the water and tracer flows in the tracer experiments carried out to validate the NETmix CFD simulations, can have negative impacts on the performance of this static mixer due to a non-uniform flow distribution at the inlets.

At last, CFD simulations in a new NETmix design, the NETmix Entire Block model, were done to deepen the study of the influence of pressure on the channels of the 1st row of this reactor when operated with dissimilar inlet flow conditions. The same Reynolds number ratios studied in the ExtendedNUB simulations (10, 100 and 1000) were used. It was verified that the pressure along the first NEB channels was not uniform in all cases, and it was lower in the channels with lower Re. This was justified by the fact that this geometry has radial inlets, which means that the flow suffers a change of geometry and direction when entering this mixer. This then leads to the formation of recirculation zones in the inlet chambers. Since these recirculation zones are more intense at the inlet chambers with higher Re, the pressure felt in them becomes higher than the pressure at the inlet chambers with lower inlet Reynolds. Consequently, this uneven flow distribution in the first rows of the NETmix coupled with an asymmetric flow distribution in the Y distributors could negatively affect the performance of the NETmix as a reactor.

The NETmix CFD simulations conducted in this dissertation showed a good potential for the application of the NETmix technology for the production of struvite crystals from the liquid fraction of digestates, attesting to its great mixing capacities, which are essential in any chemical engineering process. Nevertheless, further experimental validation of the CFD results must be performed to determine whether this reactor is actually capable of obtaining a homogenous mixing degree in its network. Furthermore, it was concluded that an uneven pressure distribution could negatively impact the flow distribution at the inlets and further affect the extent of chemical reactions occurring inside this mixer.

8 Assessment of the work done

8.1 Objectives achieved and future work

The main objective of this dissertation was to validate the use of the NETmix technology for the production of struvite crystals from the liquid fraction of side-stream digestates through CFD studies and further validation of the numerical results through tracer experiments. This was accomplished in the sense that a uniform flow distribution along the ExtendedNUB network was verified in all cases studied with dissimilar inlet flow conditions. Nevertheless, it was possible to conclude that the cases with higher inlet Reynolds ($\mathrm{Re}_l = 1200$) showed a higher mixing degree in downstream chambers and a higher dynamic behaviour of the flow promoted by vortex engulfment. The experimental work validated the conclusions drawn from the NETmix CFD studies, albeit showing an uneven tracer concentration along the rows of the reactor.

Further numerical and experimental validation should be done to better support the use of the NETmix technology for the recovery of P and N from the effluents under study and the production of a sustainable fertiliser. Some suggestions of future work are made below:

- Further CFD studies to test other asymmetric inlet flow conditions in the ExtendedNUB model, for example, different Reynolds number ratios or Re_l values between 600 and 1200;
- CFD simulations on a NUB model with a higher number of rows to assess at which point the turbulence of the flow inside the NETmix begins to stabilise and comparison with results obtained for CFD simulations with symmetric inlet flow conditions;
- Simulation of tracer experiments in the NEB model to validate the results obtained with the 2D ExtendedNUB model;
- Conducting tracer experiments in a NETmix reactor with a higher number of rows;
- CFD simulation of the struvite precipitation chemical reaction and study of the influence of the type of reactant as a Mg source and its dosage, temperature, pH and the influence of foreign ions;
- Experimental determination of struvite crystallisation using a NETmix reactor under different operating conditions to optimise the purity level of the formed crystals and their further characterisation regarding purity, size and morphology.

8.2 Other work carried out

The design of the Y-flow distributor and CFD studies to analyse the influence of the outlet pressure on the flow inside this device were not part of the main objectives of this dissertation and were done to better comprehend the reasons behind problems that emerged during the tracer experiments. The design of the NEB model and the respective CFD simulations were also not part of the original objectives and were done to deepen the study of the influence of pressure on the flow distribution at the inlets of the NETmix reactor.

8.3 Final assessment

One of the major limitations of this work were computational resources. Each simulation took a long time, more or less five days, which limited the number of conditions that could be tested.

Concerning the experimental validation, the major limitations were related to the impossibility of reproducing in a precise way the conditions used in the NETmix CFD simulations since the injection schemes were different. Moreover, the formation of air bubbles inside the tubes and their removal was also challenging.

Finally, obtaining a detailed characterisation of the centrate stream provided for this work was also challenging due to the limited amount of time to perform this dissertation.

9 References

1. Prasad, R. and D. Chakraborty, *Understanding Phosphorus Forms and Their Cycling in the Soil*. 2019.
2. Alewell, C., B. Ringeval, C. Ballabio, D.A. Robinson, P. Panagos, and P. Borrelli, *Global phosphorus shortage will be aggravated by soil erosion.* Nature Communications, 2020. **11**(1): p. 4546 DOI: 10.1038/s41467-020-18326-7.
3. Di Capua, F., S. de Sario, A. Ferraro, A. Petrella, M. Race, F. Pirozzi, U. Fratino, and D. Spasiano, *Phosphorous removal and recovery from urban wastewater: Current practices and new directions.* Science of The Total Environment, 2022. **823**: p. 153750 DOI: 10.1016/j.scitotenv.2022.153750.
4. Winkler, M., *Optimal nutrient ratios for wastewater treatment*, Hach, Editor. 2012.
5. Silva, A.J.P.R.d., *A produção de biogás na ETAR de Gaia Litoral: Estudo preliminar por Análise dos Componentes Principais*, in *Departamento de Geociências, Ambiente e Ordenamento do Território*. 2015, FCUP.
6. Shaddel, S., T. Grini, J.-P. Andreassen, S.W. Østerhus, and S. Ucar, *Crystallization kinetics and growth of struvite crystals by seawater versus magnesium chloride as magnesium source: towards enhancing sustainability and economics of struvite crystallization.* Chemosphere, 2020. **256**: p. 126968 DOI: 10.1016/j.chemosphere.2020.126968.
7. Lu, H., J. Wang, T. Wang, N. Wang, Y. Bao, and H. Hao, *Crystallization techniques in wastewater treatment: An overview of applications.* Chemosphere, 2017. **173**: p. 474-484 DOI: 10.1016/j.chemosphere.2017.01.070.
8. Achilleos, P., K.R. Roberts, and I.D. Williams, *Struvite precipitation within wastewater treatment: A problem or a circular economy opportunity?* Heliyon, 2022. **8**(7): p. e09862 DOI: 10.1016/j.heliyon.2022.e09862.
9. Costa, M.F.d.S., *The NETmix® Technology, Applied to Gas Hydrates Production: A Potential Solution to CCS*, in *Chemical Engineering Department*. 2017, FEUP.
10. Fernandes, I.S., M.S.e.C.A. de Brito, Y.A. Manrique, M.M. Dias, J.C.B. Lopes, and R.J. Santos, *Computational Fluid Dynamics Model of Two-Phase Flow in NETmix Reactors.* Chemical Engineering & Technology, 2021. **44**(11): p. 2002-2010 DOI: 10.1002/ceat.202100245.
11. Qasim, S.R. and G. Zhu, *Wastewater Treatment and Reuse Theory and Design Examples - Volume 1: Principles and Basic Treatment*. Vol. 1. 2018: CRC Press Taylor & Francis Group. 1161.
12. Comission, E. *COUNCIL DIRECTIVE of 21 May 1991 concerning urban waste water treatment*. [cited 2023 03/03/2023]; Available from: https://eur-lex.europa.eu/legal-content/EN/TXT/PDF/?uri=CELEX:01991L0271-20140101&qid=1485957216288&from=EN#page=3.
13. Victoria, E.P.A. *About wastewater*. 2022 [cited 2023 03/03/2023]; Available from: https://www.epa.vic.gov.au/for-community/environmental-information/water/about-wastewater.
14. Robertson, M. *A Guide to Measurement in Wastewater Treatment*. 2018 [cited 2023 06/03/2023]; Available from: https://www.pumpsandsystems.com/guide-measurement-wastewater-treatment.
15. Drosg, B., W. Fuchs, T.A. Seadi, M. Madsen, and B. Linke, *Nutrient Recovery by Biogas Digestate Processing*. 2015, IEA Bioenergy.
16. Maurer, C., J. Seiler-Petzold, R. Schulz, and J. Müller, *Short-Term Nitrogen Uptake of Barley from Differently Processed Biogas Digestate in Pot Experiments.* Energies, 2019. **12**: p. 696 DOI: 10.3390/en12040696.
17. Zuliani, L., N. Frison, A. Jelic, F. Fatone, D. Bolzonella, and M. Ballottari, *Microalgae Cultivation on Anaerobic Digestate of Municipal Wastewater, Sewage Sludge and Agro-Waste.* Int J Mol Sci, 2016. **17**(10) DOI: 10.3390/ijms17101692.
18. SYSTEMIC, *Liquid fraction digestate*. 2020, SYSTEMIC.
19. UNEP. *Four reasons why the world needs to limit nitrogen pollution*. 2023 [cited 2023 24/03/2023]; Available from: https://www.unep.org/news-and-stories/story/four-reasons-why-world-needs-limit-nitrogen-pollution.
20. dos Reis, G.S., P.S. Thue, B.G. Cazacliu, E.C. Lima, C.H. Sampaio, M. Quattrone, E. Ovsyannikova, A. Kruse, and G.L. Dotto, *Effect of concrete carbonation on phosphate removal through adsorption process and its potential application as fertilizer.* Journal of Cleaner Production, 2020. **256**: p. 120416 DOI: 10.1016/j.jclepro.2020.120416.

21. Siciliano, A., C. Limonti, G.M. Curcio, and R. Molinari, *Advances in Struvite Precipitation Technologies for Nutrients Removal and Recovery from Aqueous Waste and Wastewater*. Sustainability, 2020. **12**(18): p. 7538 DOI: 10.3390/su12187538.

22. Wu, I., J.D. Hostert, G. Verma, M.-C. Kuo, J.N. Renner, and A.M. Herring, *Electrochemical Struvite Precipitation Enhanced by an Amelogenin Peptide for Nutrient Recovery*. ACS Sustainable Chemistry & Engineering, 2022. **10**(43): p. 14322-14329 DOI: 10.1021/acssuschemeng.2c04691.

23. Tao, Z., J. Rongfeng, and D. Yaxin, *Phosphorus Recovery by Struvite Crystallization from Livestock Wastewater and Reuse as Fertilizer: A Review*, in *Physico-Chemical Wastewater Treatment and Resource Recovery*, F. Robina and A. Zaki, Editors. 2017, IntechOpen: Rijeka. p. Ch. 7.

24. Syrris. *Crystallization*. 2023 [cited 2023 10/06/2023]; Available from: https://www.syrris.com/applications/what-is-crystallization-and-what-are-the-methods-of-crystallization/.

25. Ma, H., Y. Zhang, Y. Xue, K. Kubota, and Y.-Y. Li, *Efficient phosphorus recovery by enhanced hydroxyapatite formation in a high loading anammox expanded bed reactor at 15 °C*. Chemical Engineering Journal, 2021. **425**: p. 130636 DOI: 10.1016/j.cej.2021.130636.

26. Chen, T. and X. Song, *Analysis of phosphorus recovery based on vivianite formation for practical applications*. Sanitary Engineering Journal, 2022. **27**(5) DOI: 10.1590/S1413-415220210164.

27. Legeros, R.Z. and J.P. Legeros, *16 - Hydroxyapatite*, in *Bioceramics and their Clinical Applications*, T. Kokubo, Editor. 2008, Woodhead Publishing. p. 367-394.

28. Water4All. *Wastewater: recover vivianite mineral, from lab to pilot scale - with Wetsus partner*. 2023 [cited 2023 10/06/2023]; Available from: https://www.water4all-partnership.eu/news/wastewater-recover-vivianite-mineral-lab-pilot-scale-wetsus-partner.

29. Chrispim, M.C., M. Scholz, and M.A. Nolasco, *Phosphorus recovery from municipal wastewater treatment: Critical review of challenges and opportunities for developing countries*. Journal of Environmental Management, 2019. **248**: p. 109268 DOI: 10.1016/j.jenvman.2019.109268.

30. Song, Y., P. Yuan, B. Zheng, J. Peng, F. Yuan, and Y. Gao, *Nutrients removal and recovery by crystallization of magnesium ammonium phosphate from synthetic swine wastewater*. Chemosphere, 2007. **69**(2): p. 319-324 DOI: 10.1016/j.chemosphere.2007.06.001.

31. Tünay, O., I. Kabdasli, D. Orhon, and S. Kolçak, *Ammonia removal by magnesium ammonium phosphate precipitation in industrial wastewaters*. Water Science and Technology, 1997. **36**(2-3): p. 225-228 DOI: 10.2166/wst.1997.0524.

32. Hao, X., C. Wang, M.C.M. van Loosdrecht, and Y. Hu, *Looking Beyond Struvite for P-Recovery*. Environmental Science & Technology, 2013. **47**(10): p. 4965-4966 DOI: 10.1021/es401140s.

33. Bayuseno, A.P., D.S. Perwitasari, S. Muryanto, M. Tauviqirrahman, and J. Jamari, *Kinetics and morphological characteristics of struvite (MgNH4PO4.6H2O) under the influence of maleic acid*. Heliyon, 2020. **6**(3): p. e03533 DOI: 10.1016/j.heliyon.2020.e03533.

34. Quintana, M., E. Sánchez, M.F. Colmenarejo, J. Barrera, G. García, and R. Borja, *Kinetics of phosphorus removal and struvite formation by the utilization of by-product of magnesium oxide production*. Chemical Engineering Journal, 2005. **111**(1): p. 45-52 DOI: 10.1016/j.cej.2005.05.005.

35. Nelson, N.O., R.L. Mikkelsen, and D.L. Hesterberg, *Struvite precipitation in anaerobic swine lagoon liquid: effect of pH and Mg:P ratio and determination of rate constant*. Bioresource Technology, 2003. **89**(3): p. 229-236 DOI: 10.1016/S0960-8524(03)00076-2.

36. Jaffer, Y., T.A. Clark, P. Pearce, and S.A. Parsons, *Potential phosphorus recovery by struvite formation*. Water Research, 2002. **36**(7): p. 1834-1842 DOI: 10.1016/S0043-1354(01)00391-8.

37. Tao, W., K.P. Fattah, and M.P. Huchzermeier, *Struvite recovery from anaerobically digested dairy manure: A review of application potential and hindrances*. Journal of Environmental Management, 2016. **169**: p. 46-57 DOI: 10.1016/j.jenvman.2015.12.006.

38. Ryu, H.-D., Y.-D. Choo, M.-K. Kang, and S.-I. Lee, *Integrated Application of Struvite Precipitation and Biological Treatment in Treating Autothermal Thermophilic Aerobic Digestion Supernatant Liquid*. Environmental Engineering Science, 2014. **31**(4): p. 167-175 DOI: 10.1089/ees.2013.0313.

39. Ghosh, S., S. Lobanov, and V.K. Lo, *An overview of technologies to recover phosphorus as struvite from wastewater: advantages and shortcomings*. Environmental Science and Pollution Research, 2019. **26**(19): p. 19063-19077 DOI: 10.1007/s11356-019-05378-6.

40. Desmidt, E., K. Ghyselbrecht, Y. Zhang, L. Pinoy, B. Van der Bruggen, W. Verstraete, K. Rabaey, and B. Meesschaert, *Global Phosphorus Scarcity and Full-Scale P-Recovery Techniques: A Review*. Critical Reviews in Environmental Science and Technology, 2015. **45**(4): p. 336-384 DOI: 10.1080/10643389.2013.866531.

41. Lopes, J.C.B., P.E. Laranjeira, M.M. Dias, and A.A. Martins, *Network Mixer and Related Mixing Process*. 2005.

42. Laranjeira, P.E.M.S.C., *NETMIX® Static Mixer Modelling, CFD Simulation and Experimental Characterisation*, in *Chemical Engineering Department*. 2005, FEUP.

43. Silva, V.M.T.M., P.A. Quadros, P.E.M.S.C. Laranjeira, M.M. Dias, and J.C.B. Lopes, *A Novel Continuous Industrial Process for Producing Hydroxyapatite Nanoparticles*. Journal of Dispersion Science and Technology, 2008. **29**(4): p. 542-547 DOI: 10.1080/01932690701728924.

44. Fonte, C.M., M.E. Leblebici, M.M. Dias, and J.C.B. Lopes, *The NETmix reactor: Pressure drop measurements and 3D CFD modeling*. Chemical Engineering Research and Design, 2013. **91**(11): p. 2250-2258 DOI: 10.1016/j.cherd.2013.07.014.

45. Lima, M.J., A.M.T. Silva, C.G. Silva, J.L. Faria, J.C.B. Lopes, and M.M. Dias, *An innovative static mixer photoreactor: Proof of concept*. Chemical Engineering Journal, 2016. **287**: p. 419-424 DOI: 10.1016/j.cej.2015.09.092.

46. da Costa Filho, B.M., G.V. Silva, R.A.R. Boaventura, M.M. Dias, J.C.B. Lopes, and V.J.P. Vilar, *Ozonation and ozone-enhanced photocatalysis for VOC removal from air streams: Process optimization, synergy and mechanism assessment*. Science of The Total Environment, 2019. **687**: p. 1357-1368 DOI: 10.1016/j.scitotenv.2019.05.365.

47. Santos, S.G.S., L.O. Paulista, T.F.C.V. Silva, M.M. Dias, J.C.B. Lopes, R.A.R. Boaventura, and V.J.P. Vilar, *Intensifying heterogeneous TiO2 photocatalysis for bromate reduction using the NETmix photoreactor*. Science of The Total Environment, 2019. **664**: p. 805-816 DOI: 10.1016/j.scitotenv.2019.02.045.

48. Espíndola, J.C., R.O. Cristóvão, S.G.S. Santos, R.A.R. Boaventura, M.M. Dias, J.C.B. Lopes, and V.J.P. Vilar, *Intensification of heterogeneous TiO2 photocatalysis using the NETmix mili-photoreactor under microscale illumination for oxytetracycline oxidation*. Science of The Total Environment, 2019. **681**: p. 467-474 DOI: 10.1016/j.scitotenv.2019.05.066.

49. Santos, S.G.S., L.O. Paulista, B.A. Marinho, C. Passalía, M. Flores, M.D. Labas, R.J. Brandi, and V.J.P. Vilar, *A step forward on NETmix reactor for heterogeneous photocatalysis: Kinetic modeling of As(III) oxidation*. Chemical Engineering Journal, 2021. **405**: p. 126612 DOI: 10.1016/j.cej.2020.126612.

50. Ribeiro, A., J.C.B. Lopes, M.M. Dias, and M.F. Barreiro, *Pickering Emulsions Based in Inorganic Solid Particles: From Product Development to Food Applications*. Molecules, 2023. **28**(6): p. 2504 DOI: 10.3390/molecules28062504.

51. Moreira, A.C.G., Y.A. Manrique, I.M. Martins, I.P. Fernandes, A.E. Rodrigues, J.C.B. Lopes, and M.M. Dias, *Continuous Production of Melamine-Formaldehyde Microcapsules Using a Mesostructured Reactor*. Industrial & Engineering Chemistry Research, 2020. **59**(41): p. 18510-18519 DOI: 10.1021/acs.iecr.0c02656.

52. FLUIDINOVA. *nanoXIM*. 2021 [cited 2023 12/06/2023]; Available from: https://www.fluidinova.com/.

53. Hu, H.H., *Chapter 10 - Computational Fluid Dynamics*, in *Fluid Mechanics (Fifth Edition)*, P.K. Kundu, I.M. Cohen, and D.R. Dowling, Editors. 2012, Academic Press: Boston. p. 421-472.

54. Matos, J., R.J. Santos, M.M. Dias, and J.C.B. Lopes, *Mixing in the NETmix Reactor*. Frontiers in Chemical Engineering, 2021. **3** DOI: 10.3389/fceng.2021.771476.

55. Brandão, S., *Fundamental studies on oscillatory NETmix Reactor*, in *Chemical Engineering Department*. 2022, FEUP.

56. ANSYS, *Ansys Fluent Theory Guide*. 2022, ANSYS, Inc.: U.S.A.

57. SIMSCALE. *What Are Boundary Conditions?* 2023 [cited 2023 17/04/2023]; Available from: https://www.simscale.com/docs/simwiki/numerics-background/what-are-boundary-conditions/.

58. Rapp, B.E., *Chapter 9 - Fluids*, in *Microfluidics: Modelling, Mechanics and Mathematics*, B.E. Rapp, Editor. 2017, Elsevier: Oxford. p. 243-263.

59. Çengel, Y.A. and J.M. Cimbala, *FLUID MECHANICS: FUNDAMENTALS AND APPLICATIONS*. 3rd ed. 2014, New York: McGraw-Hill.

60. Courant, R., K. Friedrichs, and H. Lewy, *On the Partial Difference Equations of Mathematical Physics*. IBM Journal of Research and Development, 1967. **11**(2): p. 215-234 DOI: 10.1147/rd.112.0215.

61. Danckwerts, P.V., *The definition and measurement of some characteristics of mixtures*. Applied Scientific Research, Section A, 1952. **3**(4): p. 279-296 DOI: 10.1007/BF03184936.

62. Kukukova, A., J. Aubin, and S.M. Kresta, *A new definition of mixing and segregation: Three dimensions of a key process variable*. Chemical Engineering Research and Design, 2009. **87**(4): p. 633-647 DOI: 10.1016/j.cherd.2009.01.001.

63. Brito, M.S.C.A., S.P. Brandão, N.D. Gonçalves, C.P. Fonte, M.M. Dias, J.C.B. Lopes, and R.J. Santos, *On the control of 2D turbulence by active mixing in opposed jets mixers*. Chemical Engineering Research and Design, 2023. **195**: p. 272-285 DOI: 10.1016/j.cherd.2023.05.045.

64. Kundu, P.K., I.M. Cohen, and D.R. Dowling, *FLUID MECHANICS*. 6th ed. 2016: Academic Press.

65. Cheever, E. *Introduction to the Fourier Transform*. 2022 [cited 2023 30/05/2023]; Available from: https://lpsa.swarthmore.edu/Fourier/Xforms/FXformIntro.html.

66. Torres, J.P.N.d.S., *Proper Orthogonal Decomposition of Turbulent Flows*, in *Chemical Engineering Department*. 2017, University of Porto: Porto.

67. Santos, R.J.N.d., *Mixing Mechanisms in Reaction Injection Moulding - RIM An LDA/PIV Experimental Study and CFD Simulation*, in *Chemical Engineering Department*. 2003, FEUP.

68. McDavid, R.M., *Macroscopic Modeling*, in *Encyclopedia of Materials: Science and Technology*, K.H.J. Buschow, et al., Editors. 2001, Elsevier: Oxford. p. 4720-4732.

69. australia, l. *TIPS & TRICKS: INFLATION LAYER MESHING IN ANSYS*. 2021 [cited 2023 21/05/2023]; Available from: https://www.computationalfluiddynamics.com.au/tips-tricks-inflation-layer-meshing-in-ansys/.

70. Versteeg, H.K. and W. Malalasekera, *An Introduction to Computational Fluid Dynamics THE FINITE VOLUME METHOD*. 2nd ed. 2007, England: Pearson Education Limited. 517.

71. Alziadeh, M., *Flow-sound Interaction Mechanism of a Single Spirally Finned Cylinder in Cross-Flow*. 2017.

72. Liu, H., P. Li, J.V. Lew, and D. Juarez-Robles, *Experimental study of the flow distribution uniformity in flow distributors having novel flow channel bifurcation structures*. Experimental Thermal and Fluid Science, 2012. **37**: p. 142-153 DOI: 10.1016/j.expthermflusci.2011.10.015.

73. George, H.F. and F. Qureshi, *Newton's Law of Viscosity, Newtonian and Non-Newtonian Fluids*, in *Encyclopedia of Tribology*, Q.J. Wang and Y.-W. Chung, Editors. 2013, Springer US: Boston, MA. p. 2416-2420.

74. EPA. *How Does Anaerobic Digestion Work?* 2023 [cited 2023 16/03/2023]; Available from: https://www.epa.gov/agstar/how-does-anaerobic-digestion-work.

75. Tuser, C. *What is Total Phosphorus?* 2022 [cited 2023 22/03/2023]; Available from: https://www.wwdmag.com/editorial-topical/what-is-articles/article/10940686/kruger-veolia-water-technologies-what-is-total-phosphorus.

76. Gerber, M. and N. Schneider, *Density of biogas digestate depending on temperature and composition*. Bioresource Technology, 2015. **192**: p. 172-176 DOI: 10.1016/j.biortech.2015.05.061.

77. DANETV, *Verification Report for GEA Westfalia Decanter Centrifuge*. 2010, DANETV.

78. Ge, S. and P. Champagne, *Nutrient removal, microalgal biomass growth, harvesting and lipid yield in response to centrate wastewater loadings*. Water Research, 2016. **88**: p. 604-612 DOI: 10.1016/j.watres.2015.10.054.

79. HaskoningDHV, R. *Proven crystallisation technology for purifying water and harvesting valuable resources*. 2023 [cited 2023 12/06/2023]; Available from: https://www.royalhaskoningdhv.com/en/services/crystalactor.

80. Technologies, E.W. *Ostara's Pearl® System by Evoqua*. 2023 [cited 2023 13/06/2023]; Available from: https://www.evoqua.com/en/evoqua/products--services/anaerobic-wastewater-treatment/digestor-components/pearl-system/.

Appendix A – WWTP process description

As it is shown in Figure 1 in section 2.1, there are two primary phase treatments in WWTPs, namely a liquid phase treatment and a solid phase treatment.

Regarding the liquid phase treatment, its main objective is to guarantee that the effluent is safe to be discharged into the ecosystem. It is composed of the following stages: firstly, the preliminary treatment, in which fine screens and grits remove objects of larger dimensions; then, the primary treatment aims to remove larger and denser suspended organic matter with the aid of sedimentation tanks; after, comes the activated sludge process, also known as secondary treatment, in which suspended biodegradable organic matter is removed with the aid of microorganisms; finally, there is the tertiary treatment comprising filtration stages and also disinfection processes [11].

The primary and secondary liquid treatments, more precisely the primary decantation and biological treatment, originate solid residues known as sludge that also need to be subject to several treatment processes before they leave the WWTP. These are divided into three main steps, namely sludge thickening, stabilisation or anaerobic digestion, and sludge dewatering. The first step is done to reduce sludge volume and to concentrate their solid content. Primary sludge is normally thickened in gravity thickeners. Activated sludge, for instance, is thickened in a process called air floatation, in which an ascendant air flow drags solid particles towards the surface [11].

The sludge obtained in these thickening processes is then sent to anaerobic digesters, where the production of biogas occurs. Firstly, hydrolytic bacteria convert larger biopolymers into their respective monomers. Then, fermentation reactions occur inside bacterial cells, in which alcohols, hydrogen (H_2), carbon dioxide (CO_2) and other products are formed. These products are subsequently converted into acetic acid, CO_2 and H_2 by acetogenic bacteria. Finally, there is the formation of methane (CH_4) and CO_2 (the main components of biogas) from acetic acid, CO_2 and H_2 [5]. The obtained biogas has several applications as a biofuel, such as electricity generation, heat production, vehicle fuel, among others [74].

In the last step of the solid phase treatment, the sludge resulting from the anaerobic digestion, called digestate, undergoes a dewatering process so that it can be transported by trucks and used as a fertiliser in landfills. This process may be performed in several types of equipment, such as centrifuges, rotary drums or filter presses. The water removed from the sludge, called centrate, normally returns to the primary sedimentation tank, as shown in Figure 1 [11].

Appendix B – Composition of several digestates

Tables 10 and 11 summarise the NH_4-N, TN, TP and K contents of digestates originated from anaerobic digestion with different origins. NH_4-N results from the degradation of organic nitrogen during the anaerobic digestion step and is a source of N for plants [15]. The TP content includes all phosphorus present in a solution, whether it being in the form of phosphate ions, ortho or polyphosphates (inorganic P) or organic-linked phosphates [75]. TN comprises organic N, ammonium, nitrate-nitrogen and nitrite-nitrogen [12]. It is also important to mention that the values presented for the Italian municipal wastewater digestate were calculated assuming that the density of untreated digestate is similar to the density of water (998 kg·m^{-3} at 20 °C) [76].

Table 10. Composition of digestates with different origins.

Wastewater origin	Fraction	Parameter	Concentration value/g·kg effluent^{-1}	Reference
Feedstock energy crops	Untreated digestate	NH_4-N	30.4	[16]
		TN	80.1	
		TP	7.9	
		K	59.2	
	Solid fraction	NH_4-N	6.5	
		TN	70.3	
		TP	10.1	
		K	67.8	
	Liquid fraction	NH_4-N	33.1	
		TN	25.6	
		TP	8.7	
		K	20.4	
Manure	Untreated digestate	NH_4-N	2.9	[15, 77]
		TN	4.1	
		TP	0.9	
		K	2.2	
	Solid fraction	NH_4-N	4.5	
		TN	8.2	
		TP	6.5	
		K	2.3	
	Liquid fraction	NH_4-N	2.6	
		TN	3.5	
		TP	0.3	
		K	2.3	
Municipal wastewater from an Italian WWTP	Untreated digestate	NH_4-N	1.5	[17]
		TP	0.5	

Table 11. Composition of a centrate stream.

Wastewater origin	Fraction	Parameter	Concentration value/g·kg effluent^{-1}	Reference
Municipal wastewater from a Canadian WWTP	Digestate liquid fraction	NH_4-N	0.5	[78]
		TN	0.5	
		TP	8.6×10^{-2}	

Appendix C – Struvite crystallisation technologies

Hereafter, some full-scale struvite crystallisation technologies will be presented and briefly described.

C.1 Crystalactor®

The Crystalactor technology arose from the relationship of the Aquatec Maxcon and the engineering consultancy firm Royal HaskoningDHV BV of the Netherlands. It consists of a fluisided bed reactor partially filled with a high-surface seed material, for example sand or a target mineral. Wastewater is pumped into the reactor in an ascendent direction until the bed material is completely fluisided. The crystallisation process is promoted by the addition of specific reagents, which adjust the pH value inside the reactor and supersaturate the reaction medium. The selection of the most suitable process conditions allows for the formation of crystals with high levels of purity, called pellets, and the inhibition of undesirable side reactions. When the pellets are fully grown, they sediment at the bottom of the reactor due to gravity. They are subsequently discharged from the reactor and air-dried for posterior commercialisation [79]. Figure 24 shows a schematic representation of the Crystalactor® technology.

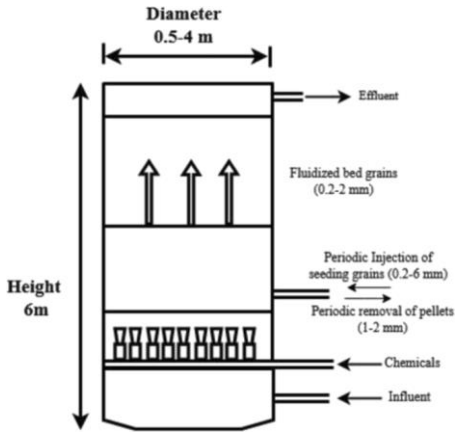

Figure 24. Crystalactor® technology schematic representation. Reprinted with permission from Gosh et al. [39]. Copyright 2019. Springer Nature.

For struvite recovery, the reagents used in the process are lime, $Mg(OH)_2$, or a combination of caustic soda and $MgCl_2$ [79].

C.2 Ostara Pearl®

The Ostara Pearl® technology was developed at Evoqua Water Technologies. It is composed of a fluidised bed reactor, inside which occurs the controlled precipitation of struvite crystals. A nutrient-rich effluent is pumped into the reactor in an upstream direction. Moreover, a magnesium source is added to the effluent stream so as to facilitate the growth of the struvite crystals and an alkaline chemical can be used to adjust the pH of the reaction medium. The formed crystals deposit at the bottom of the reactor and are subject to a dewatering and a drying process after being harvested. Finally, they are commercialised under the name of Crystal Green® Fertiliser. The treated effluent leaves the reactor at the top and is returned to a WWTP [80].

Figure 25 shows a schematic representation of the Ostara Pearl®0 technology.

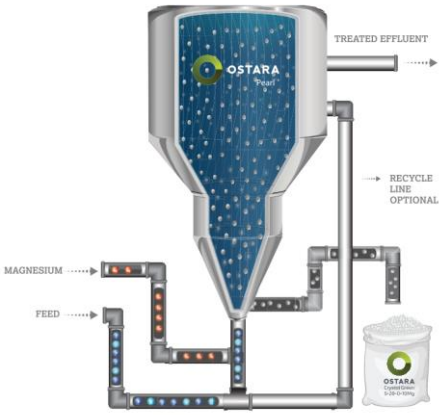

Figure 25. Ostara Pearl® process diagram [80].

C.3 NuReSys®

The NuReSys® technology was created at the Belgian company Akwadok. It should be said that this process operates in a continuous mode. Figure 26 depicts a process diagram of this technology.

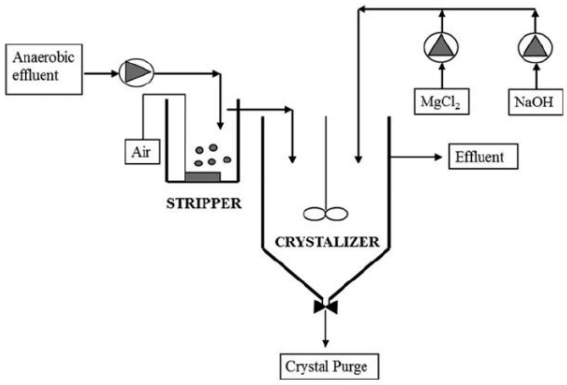

Figure 26. NuReSys® technology process diagram [40].

Firstly, the anaerobic effluent is pumped into a stripper. Air is supplied into this processing unit and CO_2 is stripped from the effluent, which results in a desirable pH increase. Then, the centrate stream is sent to a crystallisation tank equipped with a simple blade impeller and a control system that regulates reagent dosage and mixing intensity. $MgCl_2$ is added to the tank as a magnesium source and sodium hydroxide (NaOH) is added for pH adjustment. The pH of the reaction medium is kept between 8 and 8.5 to ensure that newly formed crystalline matter grows upon already existing crystals, preventing the formation of fouling on the impeller or reactor. The formed struvite pellets are discharged at the bottom of the tank intermittently and are subsequently sold under the commercial name BIOSTRU [40].

C.4 Phosnix

The Phosnix technology was developed by the Japanese company Unitika Ltd Environmental and Engineering Division. Figure 27 shows a process diagram for this technology. The centrate stream is fed into a fluisided bed reactor that uses granulated struvite as the seed material to promote the formation

of crystals. $Mg(OH)_2$ is used as the magnesium source and is added in a Mg:P molar ratio of 1:1. The pH of the reaction medium is kept between 8.2 and 8.8 through the addition of NaOH. The struvite pellets are kept inside the reactor for a period of 10 days to ensure proper crystal growth. After that time, they are discharged at the bottom of the reactor. The struvite stream then enters a separator to remove the struvite crystals with the finest dimensions. These are subsequently returned to the reactor to be used as seeding material. The struvite crystals with largest dimensions are sent to a hopper to considerably reduce their water content and then are sold as fertiliser [40].

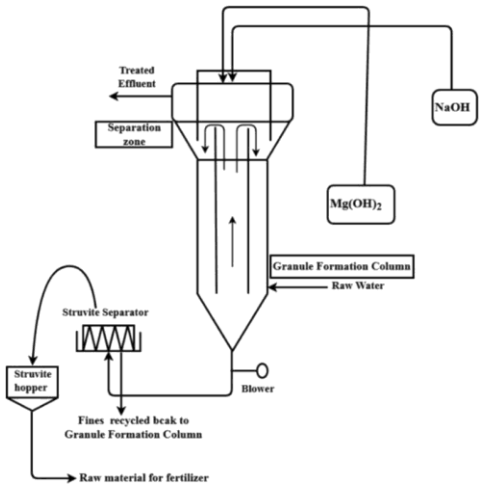

Figure 27. Process diagram for the Phosnix technology. Reprinted with permission from Gosh et al. [39]. Copyright 2019. Springer Nature.

C.5 PHOSPAQ™

The PHOSPAQ™ technology was developed by Paques. The struvite crystallisation occurs as follows: a P-rich stream is fed into an aerated continuous stirred tank reactor. Magnesium oxide (MgO) is added to the reactor as a Mg source. The pH medium is kept between 8.2 and 8.3 by the occurrence of CO_2 stripping due to aeration. After the struvite crystals are formed, they are kept inside the reactor by means of a patented separator. Then, they are collected at the bottom of the tank and redirected to a container with the aid of a screw press [40]. A process diagram for this technology is present in Figure 28.

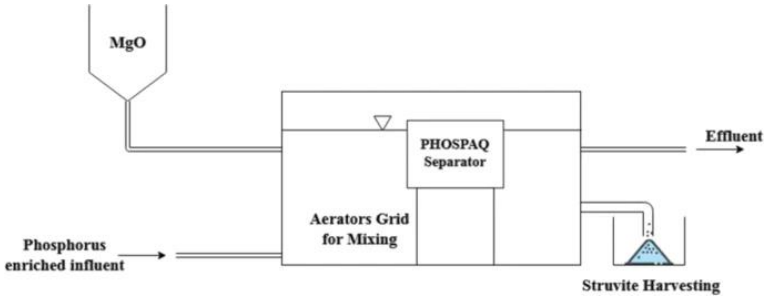

Figure 28. PHOSPAQ™ process diagram. Reprinted with permission from Gosh et al. [39]. Copyright 2019. Springer Nature.

Appendix D – Normalised I_s values for all cases

Table 12 summarises the I_s^* values obtained for channels 2 and 9 (outlets) in all cases studied (1 to 6).

Table 12. I_s^* values for channels 2 and 9 of the ExtendedNUB model.

	Channel 2		Channel 9	
Cases	$I_s^{*l,2}$	$I_s^{*r,2}$	$I_s^{*l,9}$	$I_s^{*r,9}$
1 ($\mathrm{Re}_l = 600$ and $\mathrm{Re}_r = 0.6$)	0.73	1.10	0.63	0.82
2 ($\mathrm{Re}_l = 600$ and $\mathrm{Re}_r = 6$)	1.26	0.74	0.05	0.10
3 ($\mathrm{Re}_l = 600$ and $\mathrm{Re}_r = 60$)	1.62	0.38	0.02	4.13×10^{-3}
4 ($\mathrm{Re}_l = 1200$ and $\mathrm{Re}_r = 1.2$)	0.92	1.08	0.98	0.89
5 ($\mathrm{Re}_l = 1200$ and $\mathrm{Re}_r = 12$)	0.79	1.21	0.38	0.39
6 ($\mathrm{Re}_l = 1200$ and $\mathrm{Re}_r = 120$)	1.38	0.62	6.41×10^{-6}	8.91×10^{-6}

Appendix E - Frequency spectra for the *y*-velocity component

Figure 29 shows the frequency spectra for the y-direction obtained for a midpoint in chamber C8 of the ExtendedNUB geometry for all cases studied.

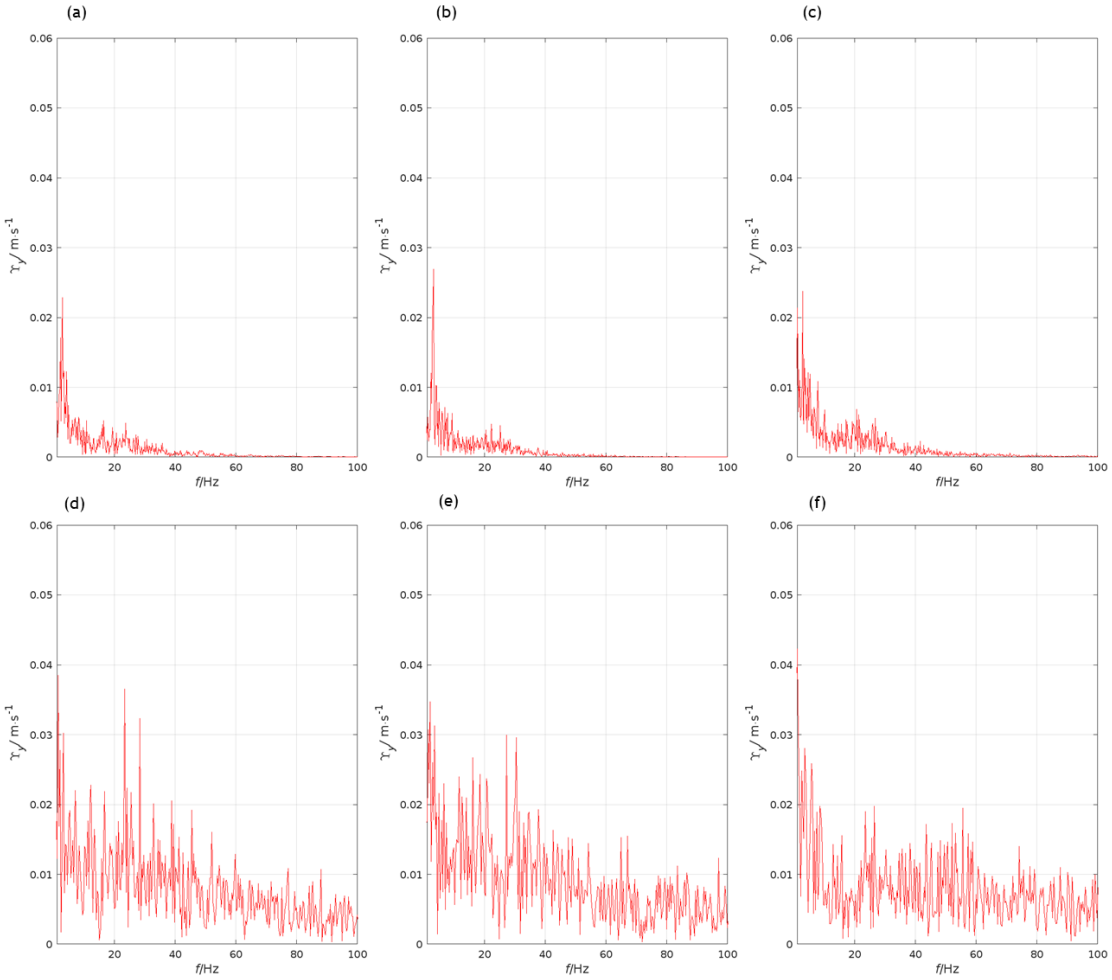

Figure 29. Frequency spectra for the y-velocity component for cases (a) 1 ($Re_l = 600$ and $Re_r = 0.6$), (b) 2 ($Re_l = 600$ and $Re_r = 6$), (c) 3 ($Re_l = 600$ and $Re_r = 60$), (d) 4 ($Re_l = 1200$ and $Re_r = 1.2$), (e) 5 ($Re_l = 1200$ and $Re_r = 12$) and (f) 6 ($Re_l = 1200$ and $Re_r = 120$).

Appendix F – Vorticity contour maps

Figures 30 and 31 show the vorticity contour maps for cases 1 to 3 and for cases 4 to 6, respectively.

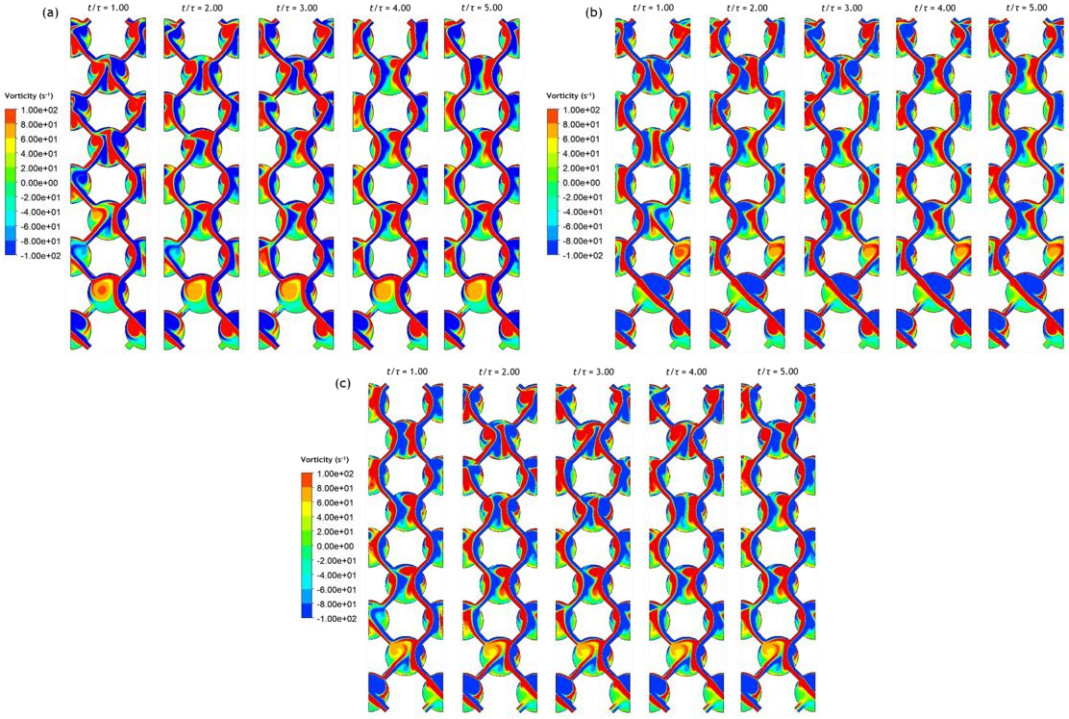

Figure 30. Vorticity contour maps for cases (a) 1 ($Re_l = 600$ and $Re_r = 0.6$), (b) 2 ($Re_l = 600$ and $Re_r = 6$) and (c) 3 ($Re_l = 600$ and $Re_r = 60$).

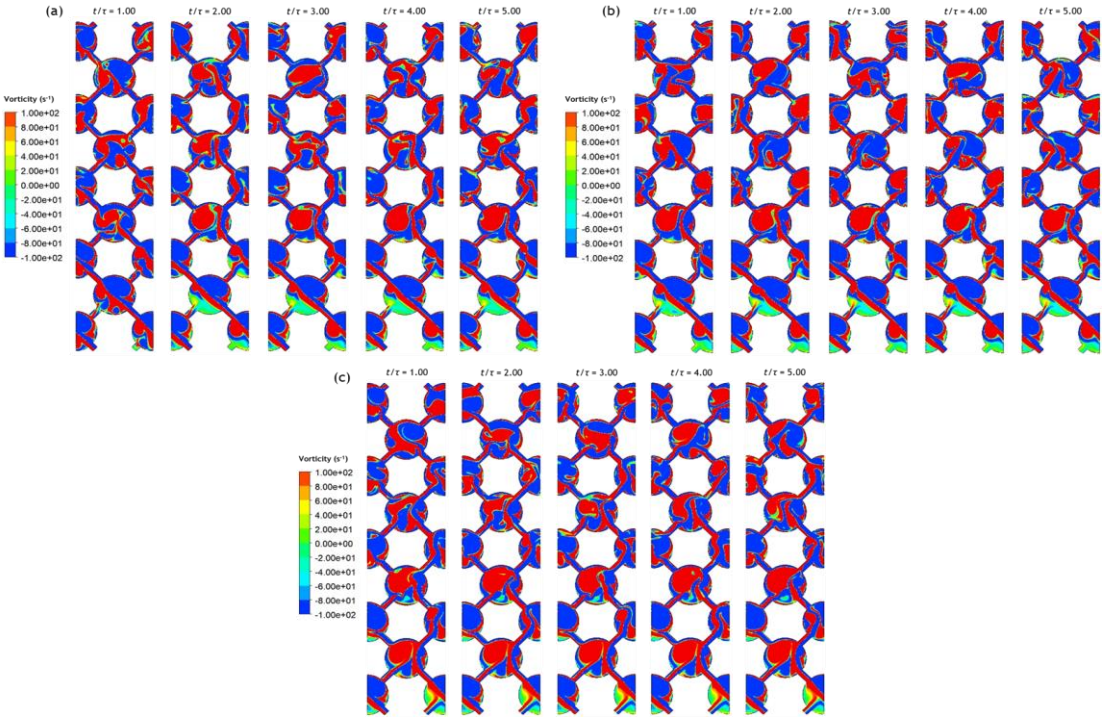

Figure 31. Tracer mass fraction contour maps for cases (a) 4 ($Re_l = 1200$ and $Re_r = 1.2$), (b) 5 ($Re_l = 1200$ and $Re_r = 12$) and (c) 6 ($Re_l = 1200$ and $Re_r = 120$).

Firstly, by analysing both figures, it is notorious the existence of the vortices in chamber C2 of all cases mentioned in section 3.5.1 of this work.

The analysis of Figures 30a to 30c shows the existence of an interface in chambers C4 to C8 (green colour) that separates vortices that oscillate in opposite directions. These vortices, however, are not symmetric since the abovementioned interfaces do not entirely coincide with the symmetry axis of each chamber. Although this shows that the mixing dynamics in these cases is not very efficient (as it was concluded in sections 3.5.2 and 3.5.3) since there is almost no vortex engulfment, the effect of Re_l being greater than Re_c is noticeable in the oscillatory behaviour of the said interfaces. Furthermore, the effect of increasing Re_r is not perceptible from Figure 30a to 30b, but in Figure 30c a more intense oscillation of the vortex interface can be seen in chamber C8 comparatively to cases 1 and 2. This shows that increasing Re_r from 12 to 120 enhances slightly the dynamic behaviour of the flow, promoting a higher mixing degree of both fluids (water and tracer).

Concerning Figures 31a to 31c, the formation of an eddy with considerable dimensions occurs in chamber C4 in all cases (4 to 6). Moreover, in chambers C6 and C8 there is no symmetric interface between vortices with opposing directions of oscillation due to the intense engulfment of vortices formed on opposite sides. This is a result of the high dynamic behaviour of the flow promoted by Re_l being equal to 1200, which significantly enhances the mass transfer between the water and tracer fluids and allows a perfectly mixed state to the achieved in the downstream chambers of the ExtendedNUB geometry.

Appendix G – Experimental setup

Next, it is shown a photograph of the experimental setup used for the tracer experiments.

Figure 32. Photograph of the experimental setup.

Appendix H - Characterisation of a digestate liquid fraction

Table 13 summarises the several physico-chemical parameters analysed and the analytical methods employed to determine them.

Table 13. Physico-chemical parameters and respective analytical methods.

Parameter	Analytical method
pH	pH was measured by a Hanna multiparameter meter, edge® model, with a HI12300 pH sensor.
TSS	Total suspended solids content was determined in accordance with the standard method 2540-D. The sample was dried at 105 °C in a Binder drying chamber.
VSS	Volatile suspended solids content was determined in accordance with the standard method 2540-E. The sample was ignited at 550 °C in a Nabertherm GmbH furnace.
TS	Total solids content was determined in accordance with the standard method 2540-B. The sample was dried at 105 °C in a Binder drying chamber.
COD[a]	Chemical oxygen demand was quantified by the following Merck Spectroquant® test kit: COD Cell Test Method: photometric 25 - 1500mg/l Spectroquant®. The samples were digested in a Spectroquant® Thermoreactor TR 420, and the absorbance reading was done in a Spectroquant® Prove 300 UV/VIS Spectrophotometer.
DOC[a]	Dissolved organic carbon (DOC) was determined by NDIR (non-dispersive infrared) spectrometry in a Shimadzu TOC-V_{CSN} analyser, equipped with an ASI-V autosampler. The equipment was calibrated with standard solutions of potassium hydrogen phthalate for total dissolved carbon (TDC) and a mixture of sodium carbonate/sodium hydrogen carbonate for dissolved inorganic carbon (DIC). DOC was calculated as follows: DOC = TDC – DIC.
Inorganic anions[a]	The presence of the following anions was studied: fluoride (F^-), chloride (Cl^-), nitrite (NO_2^-), sulphate (SO_4^{3-}), nitrate (NO_3^-) and phosphate (PO_4^{2-}). They were quantified by ion chromatography in a Dionex ICS-2100 apparatus, with an incorporated IonPac® AS11-HC column (4 × 250 mm) at 30 °C and the anion self-regenerating suppressor ASRS® 300, 4 mm. The test was conducted under isocratic elution of 30 mM NaOH at a flowrate of 1.5 mL/min for 12 min.
NH_4-N	Ammoniacal nitrogen was quantified by the following Merck Spectroquant® test kit: Ammonium Test Method: photometric 2.0 - 150 mg/l NH_4-N 2.6 - 193 mg/l NH_4^+ Spectroquant®. The samples were digested in a Spectroquant® Thermoreactor TR 420, and the absorbance reading was done in a Spectroquant® Prove 300 UV/VIS Spectrophotometer.
TN	Total nitrogen was quantified by the following method: samples pre-treatment with a Crack Set 20 for the digestion of nitrogen (total) 90 digestions Spectroquant®, and quantification with a Nitrate Test Method: photometric, DMP 0.10 - 25.0 mg/l NO_3-N 0.4 - 110.7 mg/l NO_3^- Spectroquant®. The samples were digested in a Spectroquant® Thermoreactor TR 420, and the absorbance reading was done in a Spectroquant® Prove 300 UV/VIS Spectrophotometer.

[a]Before analysis, the samples were filtrated through 0.45 µm Nylon membrane filters.

Table 13. Physico-chemical parameters and respective analytical methods (continuation).

Parameter	Analytical method
TP	Total Phosphorus was quantified by the following method: samples pre-treatment with a Crack Set 10 for the digestion of lead, cadmium, iron, copper, nickel, phosphorus (total) and zinc 100 digestions Spectroquant®, and quantification with a Phosphate Test (o-phosphate) Method: photometric, PMB 0.0025 - 5.00 mg/l PO_4-P 0.0077 - 15.3 mg/l PO_4 0.0057 - 11.46 mg/l P_2O_5 Spectroquant®. The samples were digested in a Spectroquant® Thermoreactor TR 420, and the absorbance reading was done in a Spectroquant® Prove 300 UV/VIS Spectrophotometer.
Metals[a]	The presence of the following metals was assessed: silver (Ag), aluminum (Al), boron (B), barium (Ba), bismuth (Bi), calcium (Ca), cadmium (Cd), cobalt (Co), chromium (Cr), copper (Cu), iron (Fe), gallium (Ga), indium (In), potassium (K), lithium (Li), magnesium (Mg), manganese (Mn), sodium (Na), nickel (Ni), lead (Pb), strontium (Sr), thallium (Tl), and zinc (Zn). The ICP analysis was conducted in a Thermo Scientific spectrophotometer, model iCAP 7000 Series ICP-OES.

[a]Before analysis, the samples were filtrated through 0.45 µm Nylon membrane filters.

The results obtained for pH, TSS, VSS, TS, COD, TDC, DIC, DOC, anions, NH4-N, TN and TP are present in Table 14.

Table 14. Results obtained for the digestate liquid fraction characterisation.

Parameter		Experimental values
pH at 20.9 °C		7.7
TSS/mg·L^{-1}		226
VSS/mg·L^{-1}		141
TS/mg·L^{-1}		382
COD/mg·L^{-1}		394
TDC/mg·L^{-1}		719
DIC/mg·L^{-1}		632
DOC/mg·L^{-1}		88
NH_4-N/mg·L^{-1}		3110
TN/mg·L^{-1}		1158
TP/mg·L^{-1}		62
Inorganic anions	F^-/mg·L^{-1}	0.3
	Cl^-/mg·L^{-1}	229
	NO_2^-/mg·L^{-1}	24
	SO_4^{2-}/mg·L^{-1}	44
	NO_3^-/mg·L^{-1}	6.4
	PO_4^{3-}/mg·L^{-1}	177

Tables 15 and 16 show the results obtained for the ICP analysis.

Table 15. ICP analysis results (part 1).

Metal	Ag	Al	B	Ba	Bi	Ca	Cd	Co	Cr	Cu	Fe
Concentration/ $\mu g \cdot L^{-1}$	<50	32.5	97.3	6.6	30.3	1.1×10^5	1.6	2.4	6.4	15.7	21.1

Table 16. ICP analysis results (part 2).

Metal	Ga	In	K	Li	Mg	Mn	Na	Ni	Pb	Sr	Tl	Zn
Concentration/ $\mu g \cdot L^{-1}$	<5	8.0	2.3×10^5	5.6	7.7×10^3	2.4	5.0×10^5	<5	4.9	120	<20	30.9

Appendix I – Pressure and velocity contour maps for the NEB geometry

The pressure contour maps obtained in the CFD simulations performed with the NEB geometry for the reference case and cases 1 to 3 are present in Figures 33a and 34, respectively. The velocity contour maps for the reference case and cases 1 to 3 are depicted in Figures 33b and 35, respectively. Finally, the velocity streamlines obtained for the reference case and cases 1, 2 and 3 can be seen in Figures 36, 37, 38 and 39, respectively.

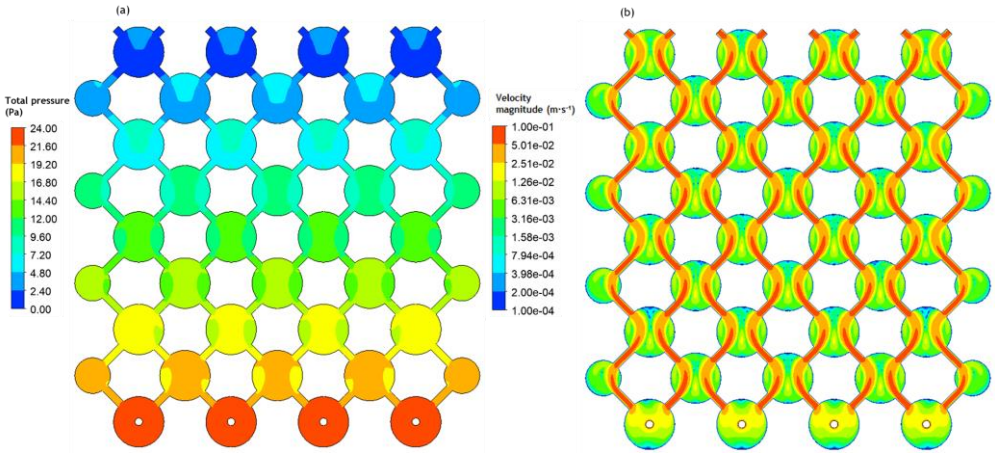

Figure 33. (a) Total pressure contour map and (b) velocity magnitude contour map (scale in logarithmic form) for the reference case.

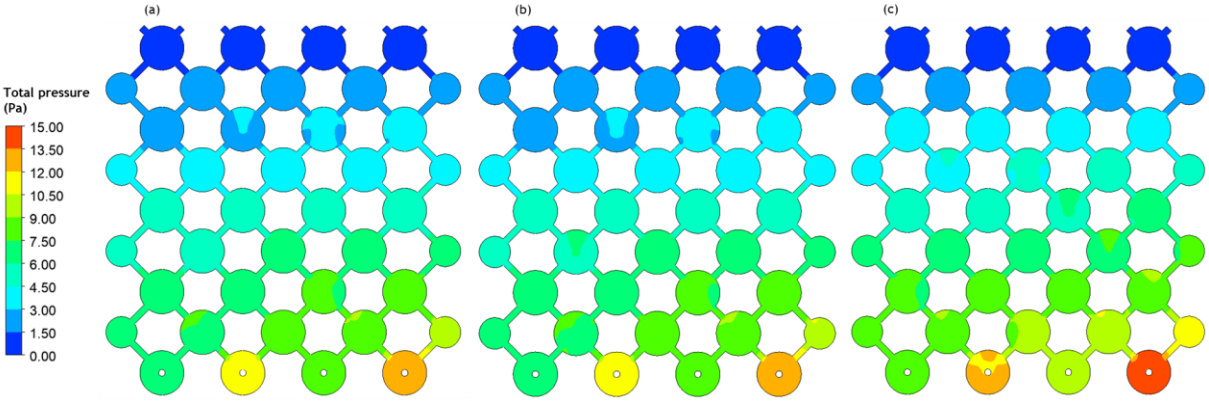

Figure 34. Total pressure contour maps for (a) case 1 ($Re_{RI1/RI3} = 0.1$ and $Re_{RI2/RI4} = 100$) (b) case 2 ($Re_{RI1/RI3} = 1$ and $Re_{RI2/RI4} = 100$), and case 3 ($Re_{RI1/RI3} = 10$ and $Re_{RI2/RI4} = 100$).

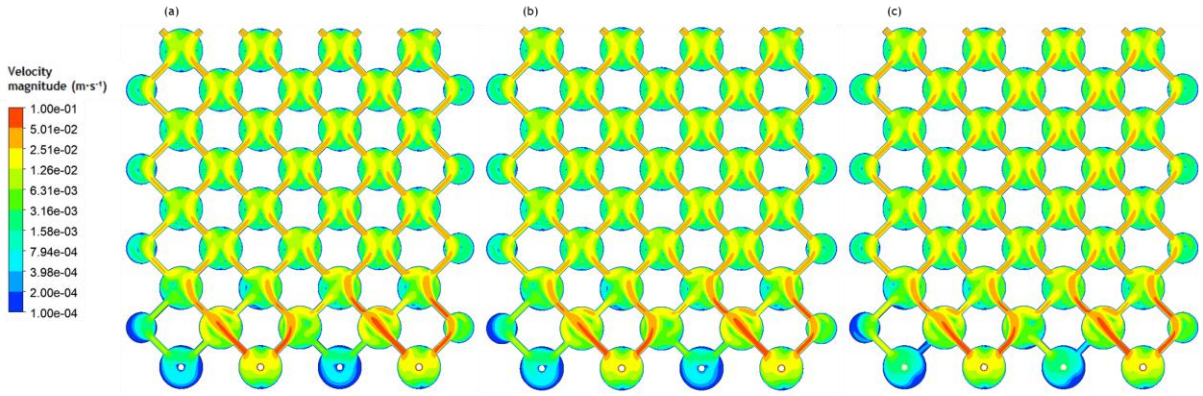

Figure 35. Velocity magnitude contour maps for (a) case 1 ($Re_{RI1/RI3} = 0.1$ and $Re_{RI2/RI4} = 100$) (b) case 2 ($Re_{RI1/RI3} = 1$ and $Re_{RI2/RI4} = 100$), and case 3 ($Re_{RI1/RI3} = 10$ and $Re_{RI2/RI4} = 100$) (scale in logarithmic form).

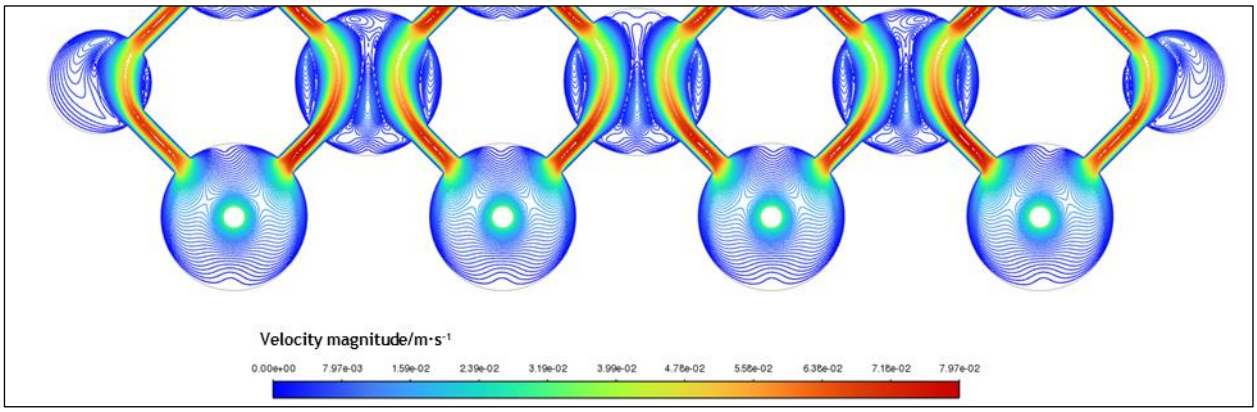

Figure 36. Velocity streamlines for the reference case.

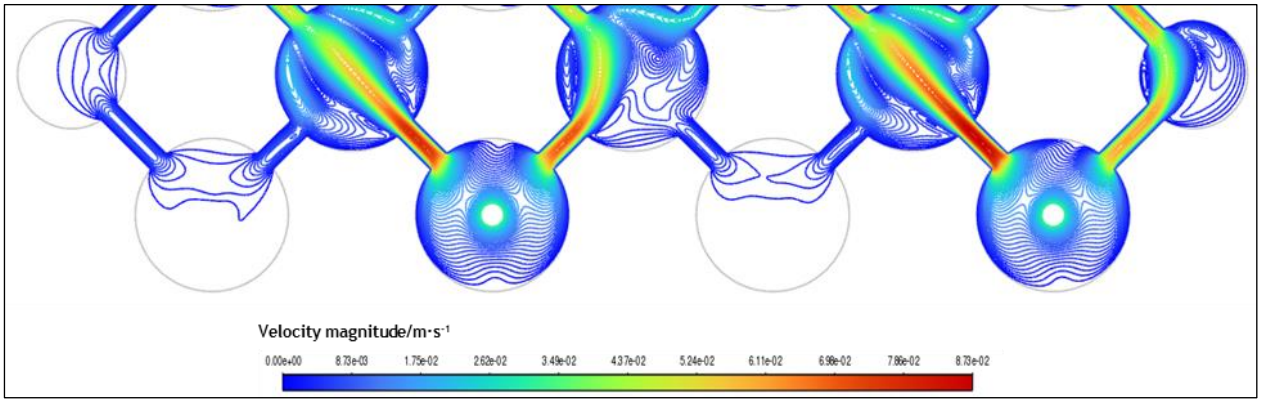

Figure 37. Velocity streamlines for case 1 ($Re_{RI1/RI3} = 0.1$ and $Re_{RI2/RI4} = 100$).

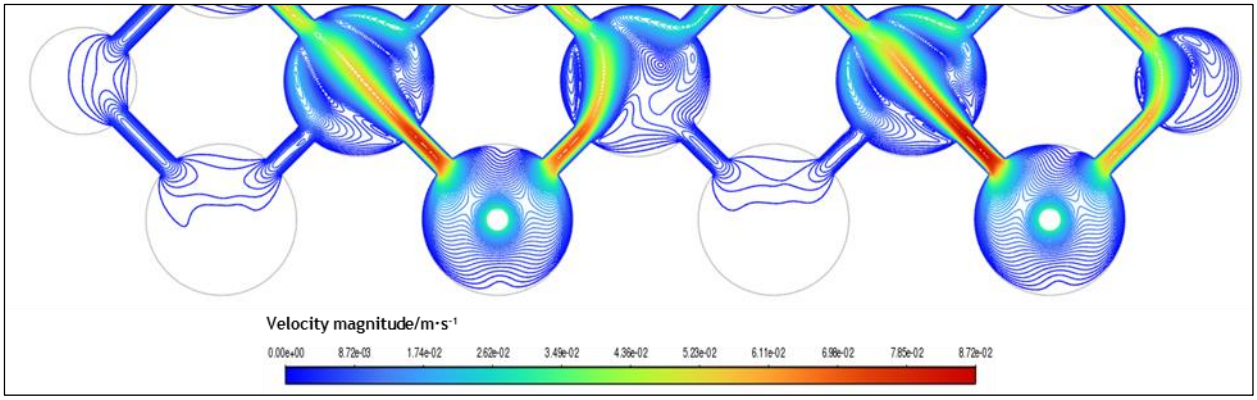

Figure 38. Velocity streamlines for case 2 ($Re_{RI1/RI3} = 1$ and $Re_{RI2/RI4} = 100$).

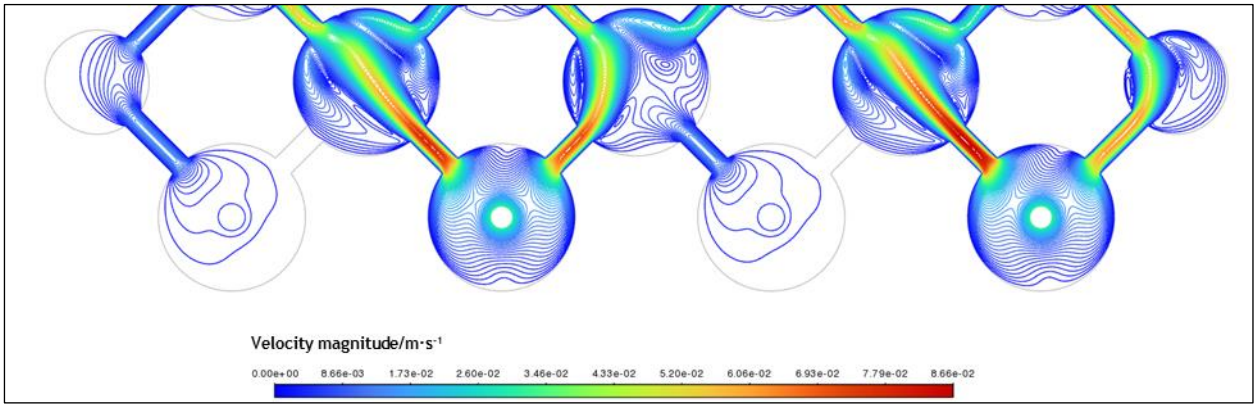

Figure 39. Velocity streamlines for case 3 ($Re_{RI1/RI3} = 10$ and $Re_{RI2/RI4} = 100$).